

FACILITY FORM 602

N 66-16 205	
(ACCESSION NUMBER)	(THRU)
231	1
(PAGES)	(CODE)
CR 6989K	30
(NASA CR OR TMX OR AD NUMBER)	(CATEGORY)

4158-6015-SU-000

INVESTIGATION OF HIGH-SPEED PHENOMENA (III)

by
J. F. Friichtenicht

GPO PRICE \$ _____

CFSTI PRICE(S) \$ _____

VOLUME II

Hard copy (HC) 6.00

Microfiche (MF) 1.25

ff 653 July 65

Prepared for
NATIONAL AERONAUTICS AND SPACE ADMINISTRATION
Contract No. NASw-936

DECEMBER 1965

TRW SYSTEMS

ONE SPACE PARK • REDONDO BEACH, CALIFORNIA

"INVESTIGATION OF HIGH-SPEED IMPACT PHENOMENA"

By J. F. Friichtenicht

VOLUME II

December 1965

Prepared Under Contract No. NASw-936 by
TRW Systems, Redondo Beach, California

for

National Aeronautics and Space Administration
Washington, D. C.

CONTENTS

FOREWORD	iii
APPENDIX A - A Solid-State Low-Noise Preamplifier (4158-6011-TU-000)	
APPENDIX B - High-Repetition-Rate Particle Injector for Electro- static Accelerator (4158-6014-TU-000)	
APPENDIX C - Velocity Selector for an Electrostatic Hypervelocity Accelerator (4158-6008-TU-000)	
APPENDIX D - Particle Parameter Selection System for an Electro- static Particle Accelerator (4158-6007-TU-000)	
APPENDIX E - Solid State High Voltage Pulser (4158-6005-TU-000)	
APPENDIX F - A Novel High Voltage Pulse Generator (4158-6006-TU-000)	
APPENDIX G - Electronic Particle-Parameter Analyzing System for an Electrostatic Hypervelocity Projector (4158-6016-TU-000)	
APPENDIX H - Micrometeoroid Simulation Using Nuclear Accelerator Techniques (9804-6008-RU-000)	
APPENDIX I - Ionization Associated with Hypervelocity Impact (8699-6002-RU-000)	
APPENDIX J - Impact Ionization from Fragile Targets (4158-6012-TU-000)	
APPENDIX K - Experiments on the Impact-Light-Flash at High Velocities (4158-6017-TU-000)	
APPENDIX L - Response of Microphone Meteorite Detectors to the Impact of High Velocity Particles (4158-6010-TU-000)	
APPENDIX M - The Interaction of Micrometeorites with Gaseous Targets (8699-6004-RU-000)	
APPENDIX N - Penetration of Thin Films by Hypervelocity Micro- particles (4158-6013-TU-000)	
APPENDIX O - Solid-State Detector (4158-6018-TU-000)	
APPENDIX P - High Voltage Breakdown Initiated by Particle Impact (4158-6009-TU-000)	

INVESTIGATION OF HIGH-SPEED IMPACT PHENOMENA (III)

By J. F. Friichtenicht
TRW Systems

FOREWORD

This document is Volume II of a two volume final report on an investigation of high-speed impact phenomena which has been conducted at TRW Systems for the past five years. The report is submitted in compliance with conditions of work done under Contracts NAS5-763, NASw-269, and NASw-561. This volume contains copies of Technical Reports and papers generated under the series of contracts. In the text of Volume I these reports and papers are referred to as Appendices. In general, the material is discussed in much greater detail than in Volume I.

A SOLID-STATE LOW-NOISE PREAMPLIFIER

APPENDIX A

A SOLID-STATE LOW-NOISE PREAMPLIFIER

by D. O. Hansen and N. L. Roy
TRW Systems, Redondo Beach, California

ABSTRACT

16205

A completely solid-state voltage sensitive preamplifier is described. A field effect transistor is used as the input stage. The equivalent noise charge referred to the input is 250 electrons. The input capacitance is 1 pf and is obtained by a bootstrapping technique. The input resistance is 10^{10} ohms, and the frequency response is from 10 kc to 7 mc. The preamplifier has a voltage gain of 15, and is linear to $\pm 2\%$ to an output voltage of 10 volts.

Author

A SOLID-STATE LOW-NOISE PREAMPLIFIER

An all-solid-state, voltage-sensitive preamplifier with low noise and broadband response has been developed for use with an electrostatic hypervelocity accelerator employed in research on hypervelocity impact phenomena.^{1,2,3} A large effective resistance and small effective capacitance have been achieved at the input stage by use of a bootstrap loop incorporating a field effect transistor as the input stage. In the hypervelocity test system the preamplifier is used in conjunction with a detector^{2,4} to measure particle velocity and charge, but its characteristics make it suitable for other applications as well. The equivalent input resistance of the preamplifier is 10^{10} ohms, and the bootstrapping reduces the effective input capacitance to about 1 pf. For a pass band of 10 kc to 7 Mc the equivalent rms input noise charge is about 250 electrons.

In the hypervelocity test system³ the detector is a cylindrical tube which is traversed axially by a charged dust particle in a time Δt that is inversely proportional to particle velocity. Electrically, the detector may be considered a capacitance to ground upon which at some instant of time a charge q (the charge of the dust particle) is placed, and from which after a time Δt is removed. The resulting voltage signal is a rectangular pulse of length Δt and of amplitude.

$$V_{in} = \frac{q}{C_{eff}}, \quad (1)$$

where C_{eff} is the effective input capacitance. The pulse has a droop of time constant τ , where τ is given by

$$\tau = R_{eff}C_{eff}, \quad (2)$$

R_{eff} being the effective input resistance. In actuality, a finite amount of time is required to deposit and to remove the charge q , hence the rise and fall times of the pulse are also finite. The values of these times necessitate a high-frequency response > 5 Mc. The transit times of the particles through the detector require that the low frequency response be extended to 10 kc.

From Eq. (1) it is clear that the effective input capacitance should be as low as possible, providing, of course, that any technique used to lower the capacitance also improves the signal-to-noise ratio. The desired decrease can be achieved by bootstrapping the input capacitance. It is shown in the appendix that the effective input capacitance with bootstrapping is given by

$$C_{eff} = C_d (1-A), \quad (3)$$

where A is the open-loop gain of the bootstrap loop and C_d is the input capacitance.

However, an undesirable effect accompanies this reduction of input capacitance. The rise time at the output of the bootstrap loop is given by

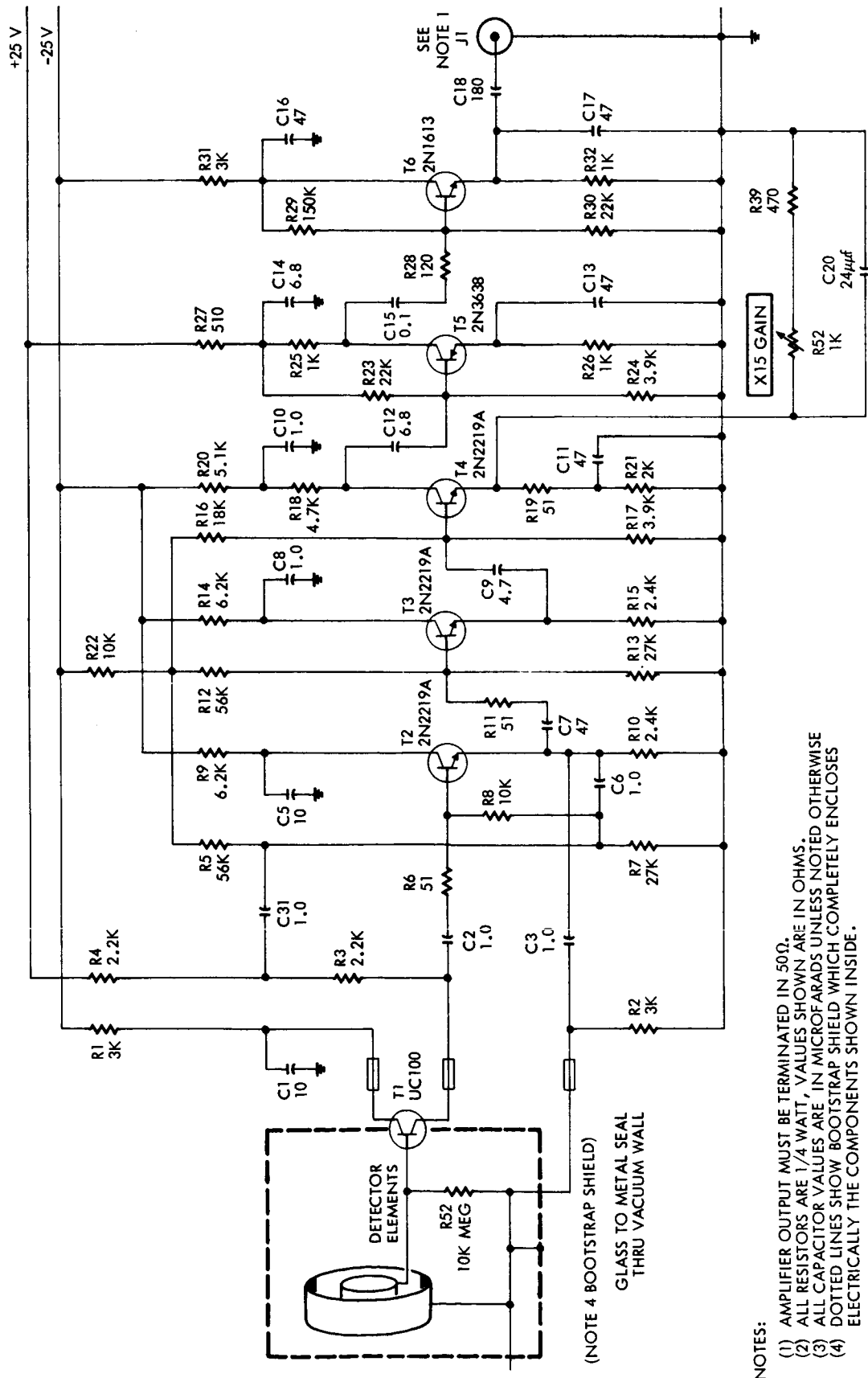
$$t_r = \frac{2.2 R_o C_b}{(1 - A)}, \quad (4)$$

where R_o is the output impedance of the bootstrap and C_b is the load capacitance that must be driven by the bootstrap loop. This equation points out that the effective load capacitance driven by the bootstrap loop is increased by the same amount that the effective input capacitance is reduced. C_b has a value of 20 pf, and a value in excess of 0.95 was obtained for A ; therefore, for a high-frequency cutoff of 10 mc, R_o must be no greater than 50 ohms. An output impedance R_o of approximately 20 ohms is easily obtained with an emitter follower, resulting in the desired high-frequency cutoff.

Vacuum tubes were originally used in the input stage of the preamplifier because tubes are quite superior to conventional bipolar transistors when high input resistance, low input capacitance, and low noise are required. However, with the development of the field effect transistor (FET) the semiconductor family became very competitive in this area, and in some instances, superior to vacuum tubes for such applications. In the source-follower configuration the FET has an equivalent input resistance of 10^{11} ohms or greater, allowing the use of a gate resistance of 10^{10} ohms, whereas the maximum value of grid resistance for tubes is much lower. It will be shown that a high value for this characteristic is very important with respect to the noise properties of the preamplifier. The interelectrode capacitances of FET's are lower, and the noise properties of this type of transistor are better than those of tubes. In addition, when vacuum tubes are used precautions must be taken to avoid the introduction of noise into the preamplifier through the filament supply; with FET's, of course, no filament supply is needed.

Although the transconductance of FET's with the above characteristics is considerably lower than that of tubes, in many cases this is not a serious disadvantage, since a conventional transistor may be used to effectively increase the g_m of the FET. (This technique is used in the preamplifier under discussion.) In using FET's care must be taken, as with all semiconductors, to insure that voltage and current ratings are never exceeded.

Figure 1 is a complete circuit diagram of the preamplifier. The bootstrap shield, which is a cylindrical tube, completely surrounds the detector and T1, the FET. The bootstrap loop is taken from the emitter of T2 back to the detector. This arrangement provides a low bootstrap-loop output impedance R_o allowing the desired high-frequency response. T3 provides a high load impedance for T2, so that the bootstrap loop gain A may be kept as close to unity as possible. (A value slightly in excess of



NOTES:

- (1) AMPLIFIER OUTPUT MUST BE TERMINATED IN 50Ω.
- (2) ALL RESISTORS ARE 1/4 WATT, VALUES SHOWN ARE IN OHMS.
- (3) ALL CAPACITOR VALUES ARE IN MICROFARADS UNLESS NOTED OTHERWISE
- (4) DOTTED LINES SHOW BOOTSTRAP SHIELD WHICH COMPLETELY ENCLOSES ELECTRICALLY THE COMPONENTS SHOWN INSIDE.

Figure 1. Complete Circuit Diagram of Preamplifier

0.95 has been obtained for A.) The detector capacitance, nominally 10 pf, is reduced to less than 0.5 pf by bootstrapping, and since the gate-to-drain capacitance of the FET averages about 0.5 pf, the total effective input capacitance is approximately 1 pf.

The two emitter-followers T2 and T3 contribute only a small amount of noise because their source resistances are quite low (500 and 20 ohms, respectively). T4 through T6 comprise a feedback amplifier with an open-loop gain of 300, which has been cut back to 15 with a resulting linearity in gain of ± 2 percent for output pulse heights to 10 volts. The emitter-follower output stage T6 allows a terminated 50 ohms transmission line to be used as the output load.

With C_{eff} equal to 1 pf, the FET input resistance of at least 10^{11} ohms allows the low-frequency cutoff to be extended to 10 kc as desired. However, this large input resistance is even more important in its effect on the noise properties of the preamplifier. The FET, the detector, and the bias network are the major sources of noise in the preamplifier. The noise equivalent of the input circuit is shown in Fig. 2, where R is the FET bias resistor, E_{tn} is the equivalent rms noise generator of the resistor, C_{eff} is the equivalent input capacitance, and V_{in} is the equivalent rms noise voltage appearing at the input of the preamplifier. The rms noise voltage amplitude of the generator is determined by

$$E_{tn}^2 = 4kTR\Delta f \quad (5)$$

It can be shown⁵ that

$$\Delta f = 1.57 f_{-3db} \quad (6)$$

where f_{-3db} is the upper half-power frequency. By use of this relationship a value for E_{tn} that is independent of R is obtained:

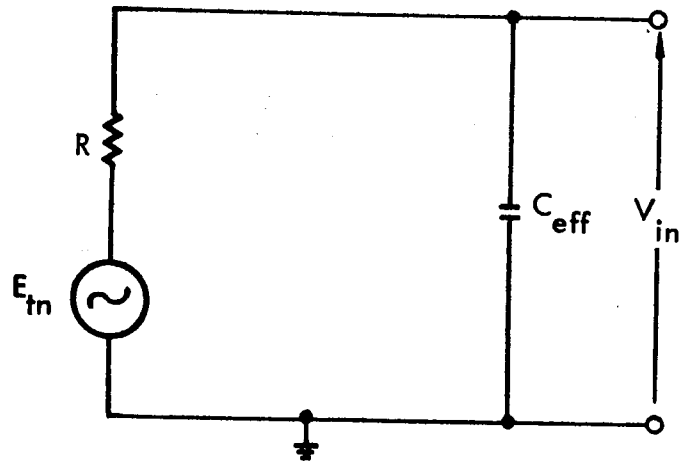


Figure 2. Noise Equivalent Input Circuit.

$$E_{tn}^2 = \frac{kT}{C_{eff}}, \text{ or}$$

$$E_{tn} = \sqrt{\frac{kT}{C_{eff}}}.$$
(7)

The voltage transfer function for Fig. 2 is

$$\frac{V_{in}}{E_{tn}} = \frac{1}{1 + i\omega RC_{eff}}$$
(8)

and the power transfer function $G(\omega)$ is the square of the voltage transfer function. For purposes of calculation it will be assumed that the preamplifier has a sharp lower cutoff at 10 kc. (If such an approximation introduces appreciable error another transfer function may be introduced to describe the details of the low-frequency cutoff.) E_n , which represents the total rms noise voltage appearing across V_{in} , the preamplifier input, can be obtained from

$$E_n^2 = 4kTR \int_{2\pi \times 10^4}^{2\pi \times 10^7} |G(\omega)| d\omega.$$
(1)

When this integral is evaluated the value of E_n is found to be 5 μ v, which is a factor of 25 less than the noise from E_{tn} . Since the maximum value of R that can be obtained with vacuum tubes is much lower (well below 10^{10} ohms), using vacuum tubes in this circuit would result in a considerably larger value of E_n .

Equivalent noise circuits have been derived for FET's;⁶ however, as a first-order approximation an FET may be regarded as a noisy resistor of value $1/g_m$. The g_m of the FET used in the preamplifier is 2000 μ mhos, resulting in an equivalent rms noise voltage at the input of 10 μ v. The measured noise voltage referred to the input was 40 μ v.

In summary, on the basis of the design considerations discussed in this paper, a preamplifier with the following

characteristics has been constructed:

1. An equivalent input resistance of 10^{10} ohms
2. An equivalent input capacitance of 1 pf
3. An equivalent rms input noise charge of 250 electrons
4. Broadband response, from 10 kc to 7 mc
5. Use of all solid-state components.

APPENDIX

The expression for the effective input capacitance with bootstrapping may be found with the aid of Fig. A-1. In this analysis the input impedance is assumed to be infinite and the reactance of C is ignored. If it assumed that at some instant a charge q is placed at the input, the following equations may be written:

$$V_i = V_{C_d} + V_o = \frac{q}{C_d} + V_o \quad (A-1)$$

$$V_o = A V_i = A \frac{q}{C_{eff}} \quad (A-2)$$

From these, it is found that

$$C_{eff} = C_d (1 - A) \quad (A-3)$$

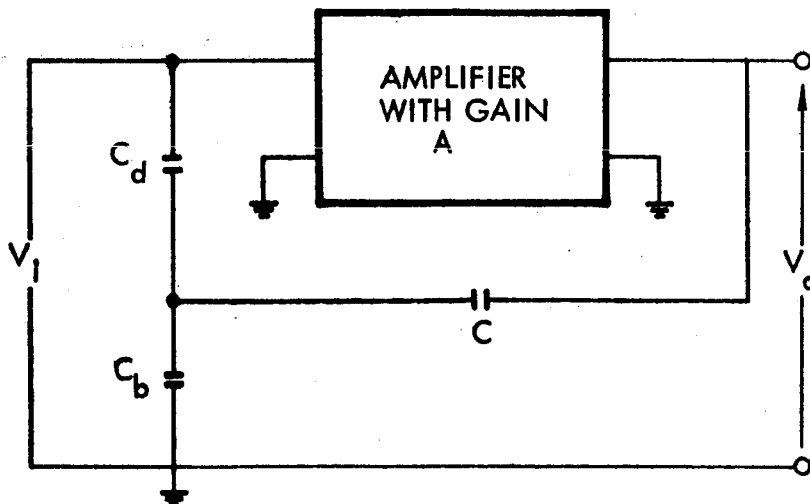


Figure A-1. Equivalent Circuit for Determination of Effective Input Capacitance with Bootstrapping.

In the preceding derivation it was assumed that the output impedance of the preamplifier was zero. The circuit in Fig. A-2 may be used to find the rise time. Again, it is assumed that at some instant a charge q is placed at the input. Then,

$$V_o = AV_i - iR_o \quad , \quad (A-4)$$

$$V_i = \frac{q}{C_d} + V_o \quad , \text{ and} \quad (A-5)$$

$$V_o = \frac{1}{C_b} \int i \, dt \quad . \quad (A-6)$$

Differentiating Eq. (A-6) and eliminating i gives

$$\frac{dV_o}{dt} + \frac{V_o(1-A)}{C_b R_o} = \frac{Aq}{C_d C_b R_o}$$

which upon solution yields

$$V_o = \frac{Aq}{(1-A)C_d} \left[1 - e^{-\frac{(1-A)t}{R_o C_b}} \right]$$

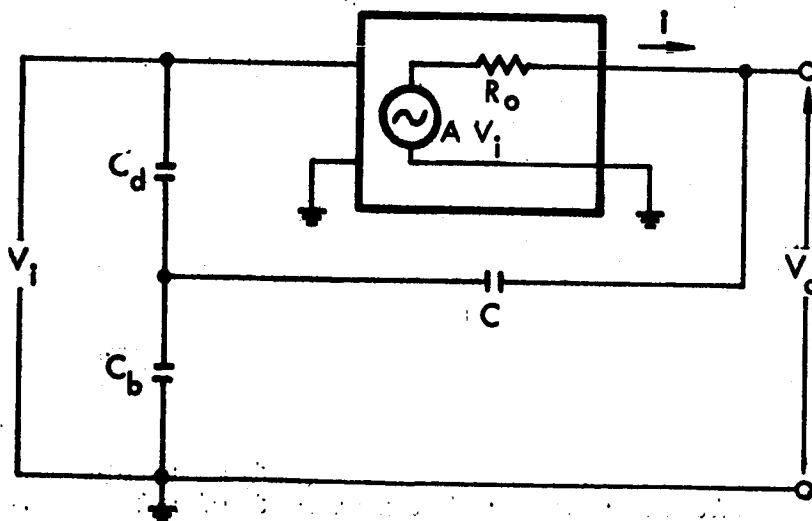


Figure A-2. Equivalent Circuit for Determination of Effective Output RC Time Constant.

The effective RC time constant is

$$RC_{\text{eff}} = \frac{R_o C_b}{(1 - A)} \quad (A-7)$$

It should be noted that if the input capacitance of the next stage is appreciable, its value should be added to C_b .

REFERENCES

1. J. F. Friichtenicht, "Two-Million-Volt Electrostatic Accelerator for Hypervelocity Research," Rev. of Sci. Inst., Vol. 33, p. 209 (February 1962).
2. J. F. Friichtenicht, "Micrometeoroid Simulation Using Nuclear Accelerator Techniques," Nuclear Inst. and Methods, Vol. 28, p. 70 (June 1964).
3. J. F. Friichtenicht, J. C. Slattery and D. O. Hansen, "Electrostatic Accelerators-Experimental Techniques," Proc. of the Seventh Hypervelocity Impact Symposium, Tampa, Florida, (November 17, 18, and 19, 1964).
4. H. Shelton, C. D. Hendricks, Jr., and R. F. Wuerker, "Electrostatic Acceleration of Microparticles to Hypervelocity," J. of Appl. Phys., Vol. 31, p. 1243 (July 1960).
5. J. F. Pierce, Transistor Circuit Theory and Design, p. 316, Charles E. Merrill Books, Inc., Columbus, Ohio (1963).
6. A. Van der Ziel, "Thermal Noise in Field-Effect Transistors," Proc. IRE, Vol. 50, p. 1808 (August 1962).

**HIGH-REPETITION-RATE PARTICLE INJECTOR
FOR ELECTROSTATIC ACCELERATOR**

APPENDIX B

TECHNICAL REPORT

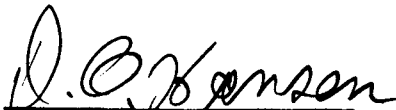
**"HIGH-REPETITION-RATE PARTICLE INJECTOR
FOR ELECTROSTATIC ACCELERATOR"**

July 1965

Prepared for

National Aeronautics and Space Administration
Washington, D. C. 20546

Contract No. NASw-936


Prepared by
D. O. Hansen


Approved by
J. F. Friichtenicht
Manager, Meteoritics Dept.

PHYSICAL ELECTRONICS LABORATORY
Physical Research Division
TRW Systems
One Space Park, Redondo Beach, California

HIGH-REPETITION-RATE PARTICLE INJECTOR FOR ELECTROSTATIC ACCELERATOR

Certain classes of experiments conducted on the TRW two-million-volt accelerator, particularly those intended to simulate long-term micrometeoroid bombardment, require a large number of particle impacts. An automatic particle-injection system capable of satisfying this requirement has been developed and is currently in use on the accelerator.

The charged-particle injector requires the application of a large negative voltage pulse in order to inject particles into the accelerator. In the original system the pulse was initiated by the manual closure of a switch, which discharged a capacitor through a pulse-forming network. The pulse from the network was fed to the grid of the high-voltage pulse tube. The operation of the switch and voltage adjustments were accomplished from the operator's console by means of solenoid-driven control rods that are an integral part of the Van de Graaff accelerator. This manual mode has been incorporated into the new system.

In the automatic system an electronic subassembly generates triggering pulses at a predetermined rate. The automatic pulsing system contains two major units, one located within the Van de Graaff console and the other in the high-voltage terminal. The pulse rate control and indicating unit shown in Fig. 1 is located within the Van de Graaff console. Indicator lamps on the control panel show the position of the console stepping switch, which corresponds to the position of a stepping switch within the terminal. The time delay insures that the solenoid is actuated long enough to allow the terminal stepping switch to step and to prevent the stepping motor from being on more than 2 seconds to prevent overheating.

Pushing the pulse-control button advances the pulse-rate

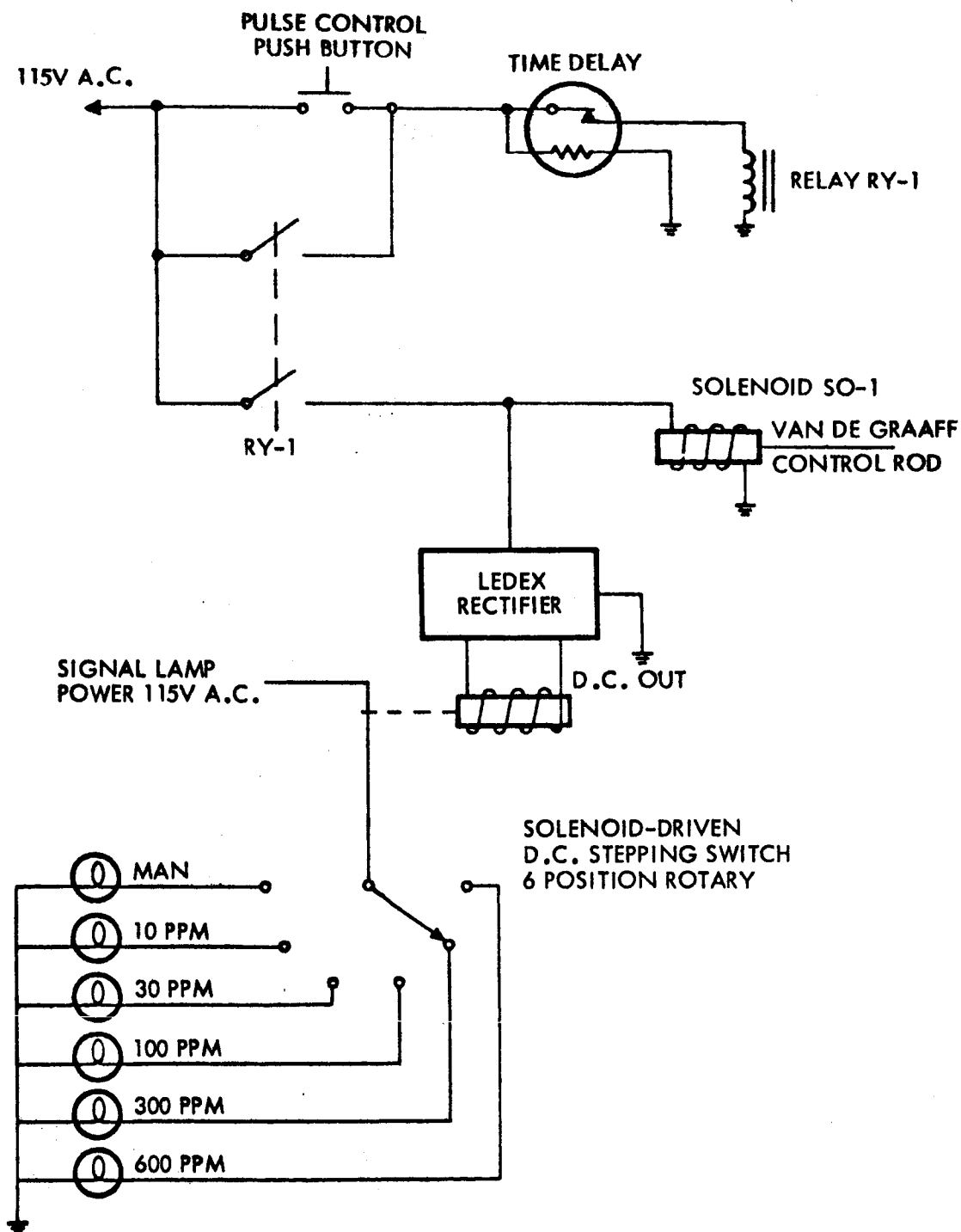


Fig. 1 Schematic of Automatic Pulse Control and Indicating Unit

switch to the next step. The sequence operates in one direction only, from manual to the slowest automatic pulse rate (10 pulses/min) and on through progressively faster rates, returning to manual one step after the fastest pulse rate (600 pulses/min).

The function of the unit located within the Van de Graaff high voltage terminal (Fig. 2) is to provide the proper pulsed and d-c voltages to the particle injector for both manual and automatic operation. A multivibrator (labeled V-1 in Fig. 2) generates the pulses employed in the automatic mode. Pulse rates are selected by changing the multivibrator coupling capacitors. Switching of the capacitors is accomplished by S-1, a solenoid-driven stepping switch. The switch is stepped by closing micro-switch S-501 by operation of a Van de Graaff control rod (as indicated in Fig. 1).

Trigger pulses for manual operation are produced by a pulse-forming network consisting of R-6, C-11, and R-8. With the manual injection switch S-503 open, C-11 charges through R-6 to 300 volts. Closing the switch discharges C-11 through R-8, producing a trigger pulse. C-12 and R-7 suppress arcing at the switch.

The trigger pulses produced by either V-1 or by the pulse-forming network are coupled to a univibrator V-2. The output pulse from this tube is 75 volts in amplitude and about 10 msec in duration, the length of the pulse being adjustable over a limited range by R-14. The pulse from V-2 is fed to the grid of V-3, which is normally cut off but conducts for the duration of the pulse, producing a voltage drop across R-20. The magnitude of the voltage pulse is determined by the voltage divider consisting of R-16 and R-17. R-16 is a potentiometer that is adjusted by a selsyn-driven control rod from the operator's console. The high-voltage pulse obtained at the plate of V-3 is applied to the particle injector.

The number of particles injected per pulse is a function of pulse amplitude and duration, which are normally adjusted so that

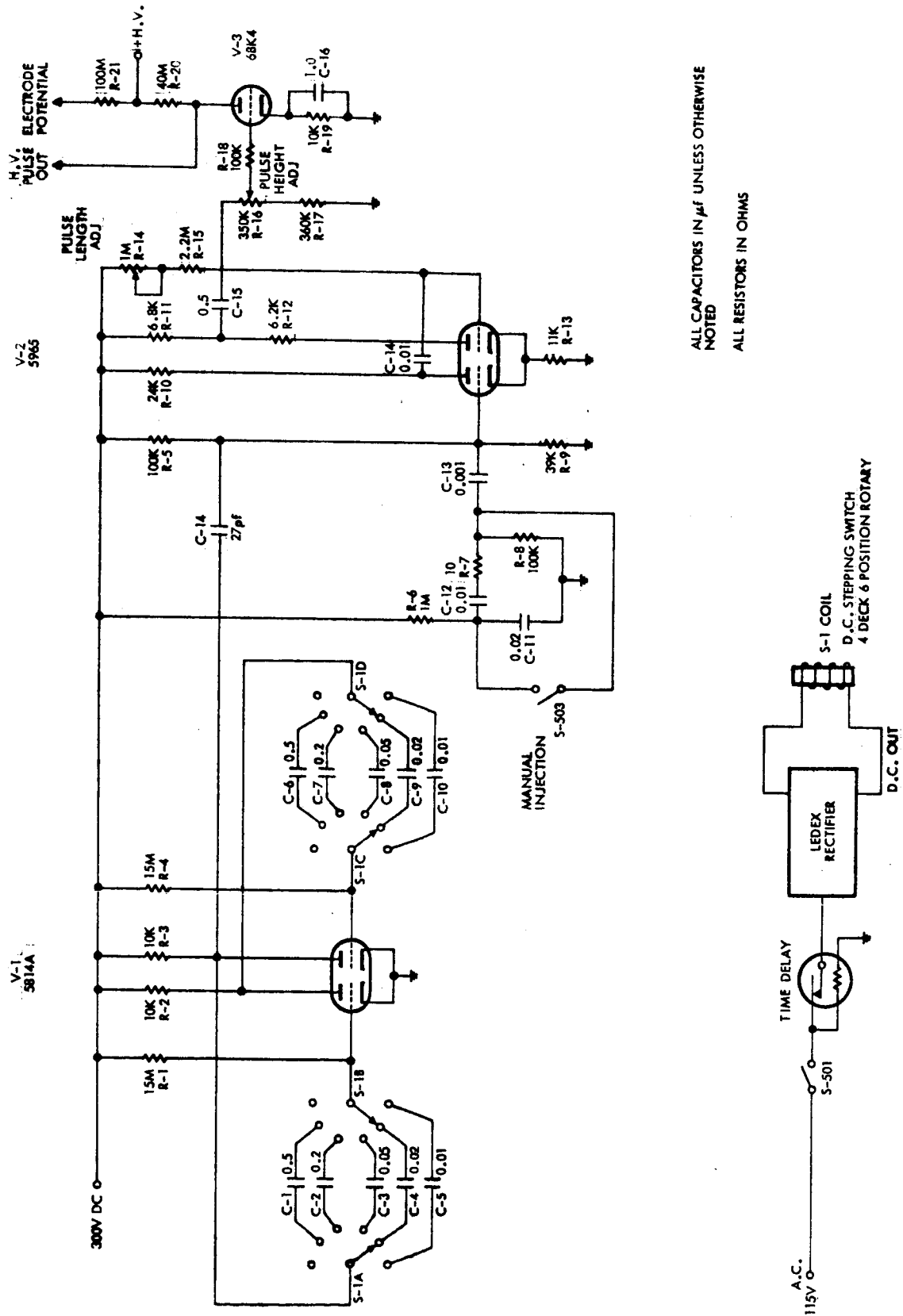


Fig. 2 Schematic of Automatic Pulser Unit within Van de Graaff Terminal

the average rate is about one particle per pulse. The injector has been operated under these conditions at the rate of 10 particles per second for periods of over 100 hours with no noticeable deterioration in performance.

VW

**VELOCITY SELECTOR FOR AN ELECTROSTATIC
HYPERVELOCITY ACCELERATOR**

APPENDIX C

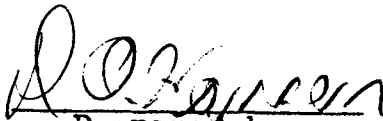
TECHNICAL REPORT

"VELOCITY SELECTOR FOR AN ELECTROSTATIC
HYPERVELOCITY ACCELERATOR"

July 1965

Prepared for

National Aeronautics and Space Administration
Washington, D. C. 20546
Contract No. NASw-936


Prepared by
D. O. Hansen


Approved by
J. F. Friichtenicht
Manager, Meteoritics Dept.

PHYSICAL ELECTRONICS LABORATORY
Physical Research Division
TRW Systems
One Space Park, Redondo Beach, California

VELOCITY SELECTOR FOR AN ELECTROSTATIC
HYPERVELOCITY ACCELERATOR

The TRW electrostatic hypervelocity accelerator¹ is capable of accelerating micron-size electrically charged dust particles to velocities in excess of 30 km/sec. Because obtaining high velocity data with the basic system alone is difficult and time consuming, the practical upper limit on particle velocity prior to development of a velocity selection system was about 15 km/sec. The velocity selector has raised this upper limit to that of the accelerator itself, or above 35 km/sec.

The detectors used with the electrostatic accelerator are described elsewhere.² The output of the detectors consists of a rectangular wave with a height proportional to the charge of the particle and a length inversely proportional to its velocity. This signal is amplified by a low-noise preamplifier³ and then displayed on an oscilloscope. The trace is usually photographed so that the parameters of the particle may be precisely measured.

The faster particles generally carry a smaller charge and therefore generate smaller signals than those produced by the slower particles. The oscilloscope sweep is usually triggered internally so that all particles with less than a specified velocity v_0 sweep the oscilloscope. Thus, in order to obtain data on high-speed particles, all particles with less than the desired velocity must also be recorded and the resulting traces sorted to isolate the high-velocity-particle pictures, which constitute a small fraction of the total number of traces recorded.

These difficulties are compounded because the dust powder available for acceleration does not have a uniform size distribution. The distribution curve peaks for particles of about 1 to 2 microns radius, and particle velocities correspondingly peak at around 5 to 7 km/sec. This peak is quite sharp and

falls off particularly fast in the direction of decreasing radius and higher speed.

A further serious hindrance to obtaining high-velocity data is low-frequency noise. For accurate measurement of particle parameters, the frequency response of the preamplifier must be extended to low frequencies (10 kc or less). A great deal of low-frequency noise reaches the oscilloscope input despite the many precautions that are taken. This noise is not troublesome on an oscilloscope trace because its frequency is low compared to the sweep rate, but it can trigger the oscilloscope, causing it to sweep continuously. The trigger level must therefore be set well above this low-frequency noise level to avoid spurious triggering, with the result that very-low-charge particles do not sweep the oscilloscope. Since these low-charge particles are also the ones with high velocity, the effect of low-frequency noise is to place an upper limit on velocities that can be measured.

To alleviate the above problem a velocity selector system was designed and constructed. As can be seen in the logic diagram presented as Fig. 1, three particle detectors are used with the velocity selector; the first two are velocity detectors, while the third is a charge detector. For some applications only the velocity detectors are used, whereas in other experiments the entire system is required.

The velocity detectors have a relatively narrowband frequency response of 1 to 10 mc. The outputs of preamplifiers No. 1 and 2 are fed to pulse height discriminators, which are set so that they are triggered by noise at a rate of 20 to 50 pps. Discriminator No. 1 triggers a one-shot multivibrator that has an adjustable period. At the end of the period selected, a second one-shot multivibrator of variable period is triggered. A gate is opened for the period of this second one-shot, and pulses from discriminator No. 2 will pass through the gate if they appear

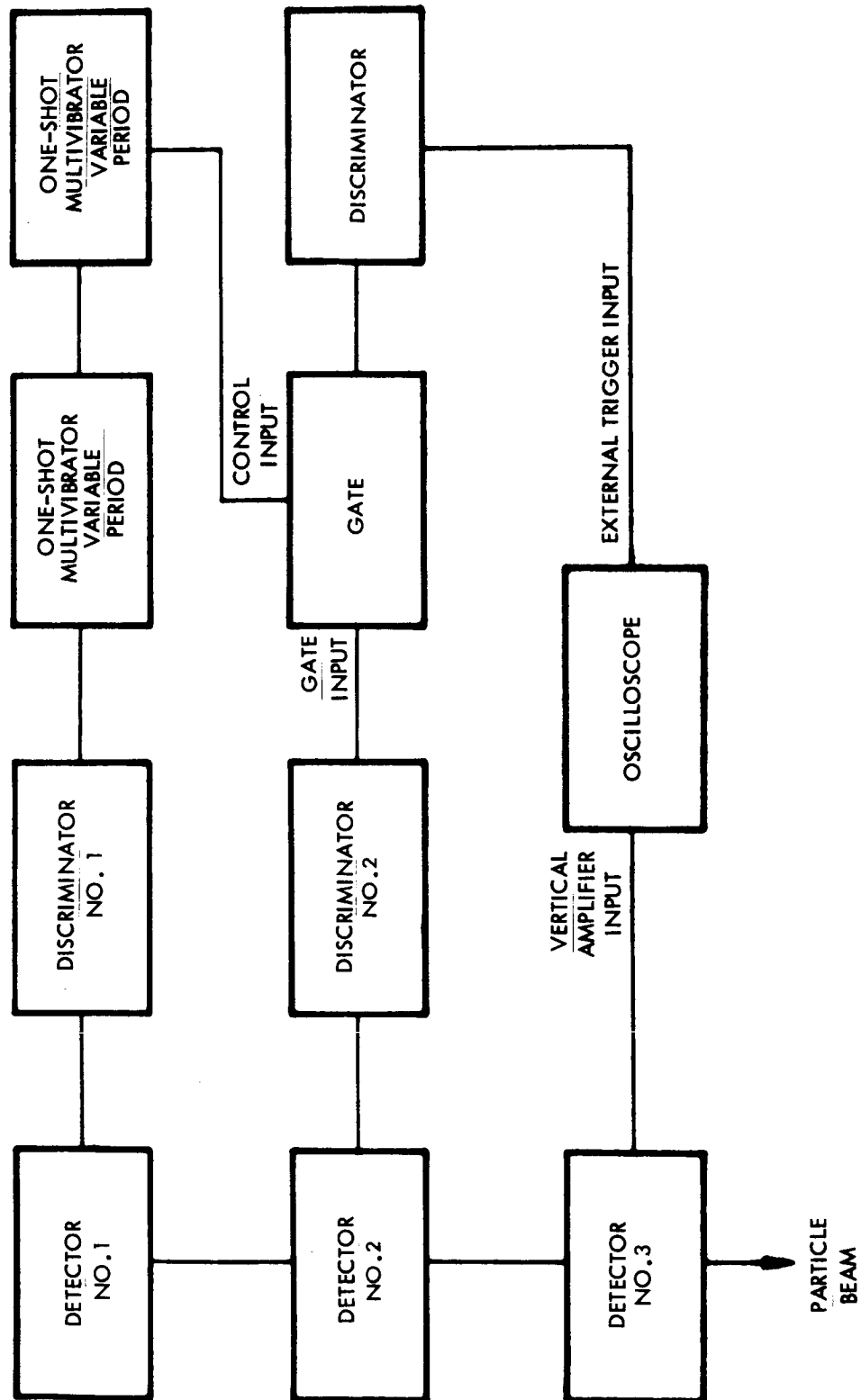


Figure 1. Logic Diagram of Velocity Selector

during this time. Pulses that come through the gate are detected by a discriminator whose output ordinarily sweeps the oscilloscope but may also be used for other purposes, such as activation of a particle-deflection system that is described in some detail elsewhere.⁴

The accidental rate of the velocity selector is calculated from the standard coincidence accidental formula

$$R_{acc} = R_1 R_2 \Delta t ,$$

where R_1 and R_2 are the rates of discriminators Nos. 1 and 2. For R_1 and R_2 equal to 50 pps and Δt equal to 10^{-5} sec, $R_{acc} = 2.5 \times 10^{-2}$, which is a very acceptable rate for most conditions. The value of Δt chosen for this example is larger than required for all but the widest velocity windows (1 to 40 km/sec.)

If a precise determination of particle mass is necessary for an experiment, a pulse height window discriminator may be placed on the output of detector No. 3 to specify a particle charge interval, just as the velocity selector is used to specify a particle velocity interval. The simultaneous specification of charge and velocity is equivalent to specifying a mass interval, since the specification of charge and velocity together with the accelerator voltage allows the mass of the particle to be calculated.

The velocity selection system is used for experiments requiring data over a small particle-velocity interval. For tests of transient phenomena, such as impact ionization, behavior of particles under free-molecular-flow conditions, etc., the velocity-selecting section of the system is all that is needed. However, for experiments on phenomena such as cratering the particle-deflection system is used. When this system is used with the velocity selector, the crater structure can be related accurately to the impacting particle parameters.

REFERENCES

1. J. F. Friichtenicht, "Two-Million-Volt Electrostatic Accelerator for Hypervelocity Research," Rev. of Sci. Instr., Vol. 33, 209 (1962).
2. H. Shelton, C. D. Hendricks, Jr., and R. F. Wuerker, "Electrostatic Acceleration of Microparticles to Hyper-velocities," J. Appl. Phys., Vol. 31, 1243 (1960).
3. D. O. Hansen and N. L. Roy, "A Solid-State Low-Noise Preamplifier," Submitted for publication in Nuclear Instruments and Methods, also, TRW Systems Technical Report 4158-6011-TU-000, June 1965.
4. J. F. Friichtenicht, "Particle Parameter Selection System for an Electrostatic Particle Accelerator," Submitted for publication as a NASA Technical Note, also, TRW Systems Technical Report 4158-6007-TU-000, April 1965.

**PARTICLE PARAMETER SELECTION SYSTEM
FOR AN ELECTROSTATIC PARTICLE ACCELERATOR**

APPENDIX D

TECHNICAL REPORT

PARTICLE PARAMETER SELECTION SYSTEM
FOR AN ELECTROSTATIC PARTICLE ACCELERATOR

8 April 1965

Prepared for
National Aeronautics and Space Administration
Washington, D. C. 20546

J. F. Friichtenicht

Prepared by
J. F. Friichtenicht
Manager
Meteoritics Department

D. B. Langmuir

Approved by
D. B. Langmuir
Director

PHYSICAL ELECTRONICS LABORATORY
Physical Research Division
TRW Space Technology Laboratories
Thompson Ramo Wooldridge Inc
One Space Park
Redondo Beach, California

PARTICLE PARAMETER SELECTION SYSTEM
FOR AN ELECTROSTATIC PARTICLE ACCELERATOR*

J. F. Friichtenicht
TRW Space Technology Laboratories, Redondo Beach, California

INTRODUCTION

The electrostatic hypervelocity particle accelerator¹ has been used in a variety of experiments concerned with micrometeoroid simulation and hypervelocity impact.² One of the major problems associated with the use of the accelerator is the inability to specify in advance the parameters of a particle prior to impact upon an experimental complex. This occurs because of the size distribution of particles comprising the particle supply. As has been shown,³ the charge-to-mass ratio (and therefore, the final velocity) is an inverse function of particle size. The iron powder which has been used extensively contains particles ranging from a few tenths to several microns in diameter. Thus, wide variations in particle velocity and mass are observed.

The use of finely graded powders in several size ranges would partially alleviate the problem. Unfortunately, the state of fine particle technology has not advanced to the point of providing suitable particles. An alternative method is to make the particle selection following acceleration and prior to impact.

Since the particle charge-to-mass ratio is a function of particle size, specification of particle velocity also specifies particle size to an accuracy determined by variations in the charging process. A system which permits particles with velocities within a small interval to reach the target while rejecting all others is a satisfactory solution to the data collection problem. A system embodying this concept has been constructed and tested.

*This work supported under NASA Contract NASw-936, "Investigation of Hypervelocity Impact Phenomena".

The main elements of this system are an electrostatic deflector, a velocity sensing and gating circuit, and a high voltage pulse circuit. Each of these elements are discussed below.

The Electrostatic Deflector

The function of the electrostatic deflector is to deflect unwanted particles from the beam while permitting selected particles to pass through unperturbed. The deflector, consisting of a pair of parallel plates with a potential difference V_d between them, is shown schematically in Fig. 1. Upon entering the region between the plates, particles from the accelerator experience a force perpendicular to the original direction of motion given by

$$F_p = qE \quad , \quad (1)$$

where q is the particle charge and E is the electric field between the plates. Integrating, we get

$$v_p = \frac{q}{m}Et \quad , \quad (2)$$

where v_p is the velocity component perpendicular to the original trajectory, m is the particle mass, and t is the time spent in the deflection region. The time required to traverse the length of the plates L is determined by the initial velocity v and is given by

$$t = \frac{L}{v} = L \left(\frac{m}{2qV} \right)^{1/2} \quad , \quad (3)$$

where V is the accelerating voltage. The perpendicular velocity component at the exit plane of the plates is

$$v_p = E \left(\frac{m}{2qV} \right)^{1/2} L \quad . \quad (4)$$

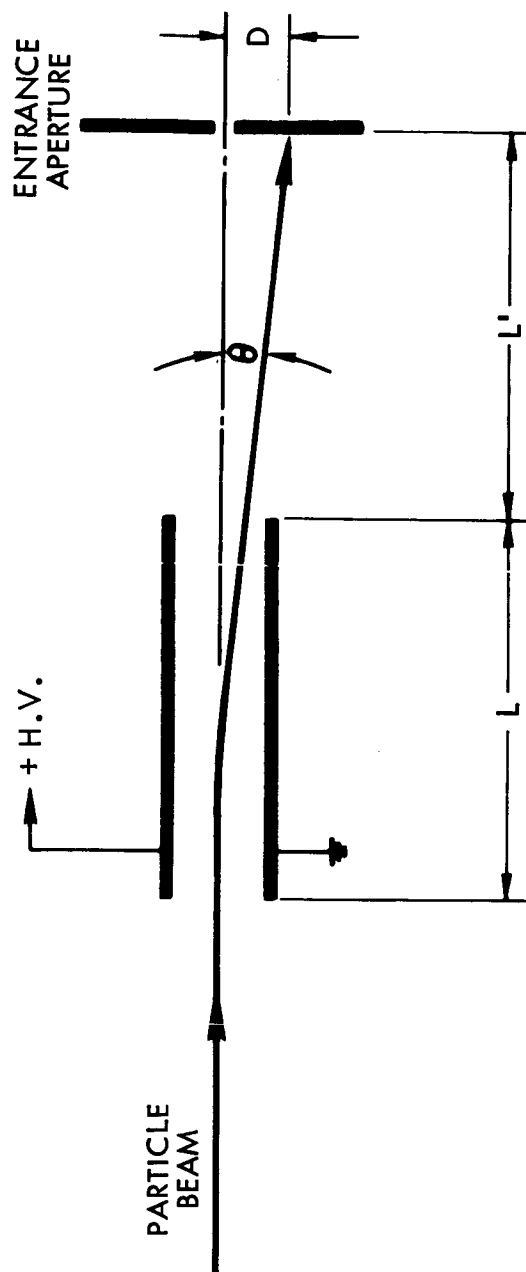


Figure 1. Sketch depicting the operation of the electrostatic deflector.

Furthermore,

$$\frac{v_p}{v} = \frac{EL}{2V} \tan \theta \quad , \quad (5)$$

where θ is the angle between the initial and final trajectories. It should be noted that this expression is independent of particle parameters and all particles traversing the deflection region describe identical trajectories regardless of their charge-to-mass ratio.

By integrating Eq. (2) and combining the result with Eq. (5), it is a simple matter to determine the total displacement D imparted to the particle at any distance L' downstream from the particle deflector. For values of $E = 2 \times 10^6$ volts/meter, $V = 2 \times 10^6$ volts, $L = 0.15$ meter, and $L' = 0.15$ meter, the displacement is 1.25 cm. Since particles from the accelerator are focused into a much smaller spot than this, the magnitude of the deflection is more than adequate to deflect particles from the entrance aperture of an experimental chamber.

The Velocity Sensing and Gate Circuit

As was mentioned above, specifying particle velocity determines particle mass for a given set of conditions. Accordingly, particle parameter selection is made on the basis of a velocity measurement. The velocity selection system is illustrated schematically in Fig. 2. The velocity sensor consists of a pair of short, capacitive-type detectors (see Ref. 3) separated by a fixed distance. The signals from each of the detectors are amplified and presented to voltage discriminators where uniform pulses are generated for each signal exceeding the discrimination level. The output pulse from the first discriminator triggers a "one-shot" multivibrator which produces a pulse of adjustable length. The trailing edge of this pulse triggers another one-shot multivibrator of variable, but preset length. This pulse opens the

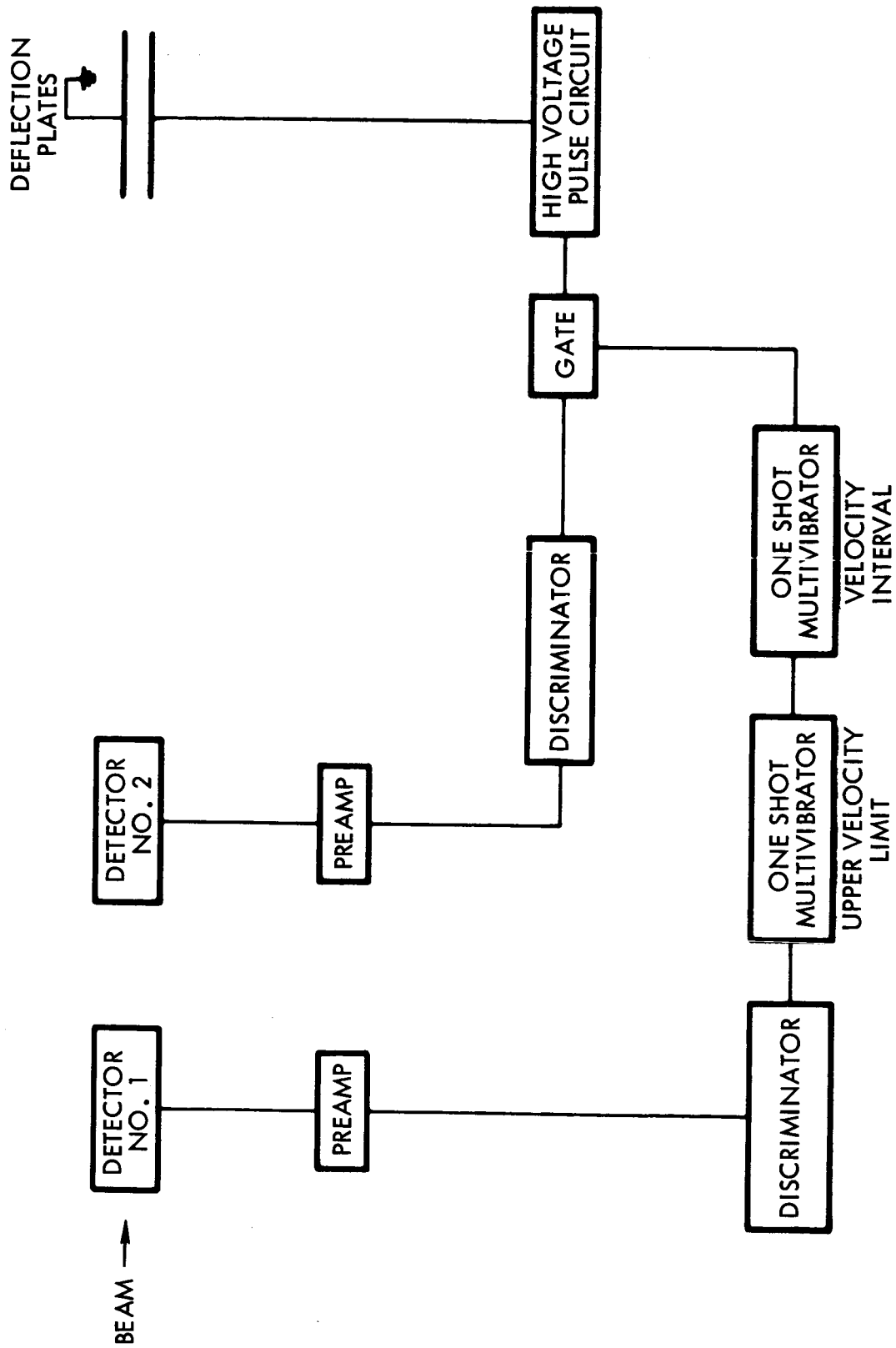


Figure 2. Block diagram of the particle parameter selection system.

gate of an electronic gating circuit for the duration of the pulse. The output pulse from the second discriminator is fed to the gate and if it appears while the gate is open, an output trigger pulse is generated. The trigger pulse is delivered to the high voltage section of the system.

It can be seen that the duration of the first multivibrator pulse determines the upper velocity limit of the system while the duration of the second multivibrator pulse determines the velocity interval over which trigger pulses are generated. The durations of both of these pulses are adjusted by switching the multivibrator coupling capacitors. The switching is accomplished by multi-position wafer switches and a wide variety of velocity intervals may be selected.

It should be pointed out that the velocity sensing system can be used to advantage in other ways, as well. For example, the trigger pulse can be used to gate an oscilloscope in order to display only desired signals, while ignoring all others. The use of the system also increases the apparent signal-to-noise ratio of the detectors. The latter manifestation is discussed more thoroughly in another report⁴ which also includes a detailed description of the electronic circuitry.

The High Voltage Pulse Section

When a trigger pulse is received, the high voltage pulse circuit discharges the voltage across the deflection plates, thereby allowing the particle to proceed on to the target. With the exception of the method by which the grid drive pulse is generated,⁵ the operation of the high voltage pulse circuit is conventional in all respects.

The trigger pulse from the velocity sensing and gate circuit is first fed to a one-shot multivibrator whose period is adjustable to several values roughly corresponding to the time required for the selected particle to traverse the deflection region. The

output pulse from the multivibrator is applied to the grid drive pulse generator. This circuit produces a moderately fast rising high voltage pulse (about 1,000 volts negative) of a duration equal to the length of the input pulse. For a detailed description of the grid drive pulse generator which employs all solid-state electronics, see Ref. 5.

One plate of the deflection system is grounded while the other is connected to the plate of a high voltage pulse modulator tube. Normally the tube is cut off and the deflection plate is at the power supply voltage. Application of the driver pulse to the grid via an inverting 1:1 pulse transformer drives the tube into saturation thereby dropping the voltage between the deflection plates.

For proper operation of the deflector, the voltage between the plates must be completely discharged before the particle arrives and must remain discharged until the particle has traversed the plates. These requirements impose limits upon the rise time and duration of the high voltage pulse. The deflection plates constitute a capacitive load for the tube of the order of 100 picofarads which must be discharged in about a microsecond. A high voltage pulse modulator tube (English Electric Valve Co., C1150/1, equivalent to an Eimac 4PR60B) was used in this case because of availability, although somewhat lower power tubes would be equally satisfactory.

SUMMARY

The particle parameter selection system described above is a valuable addition to the techniques and methods which have been developed in connection with the electrostatic particle accelerator. Even when used alone, the velocity sensing and gate circuit is very useful in the detection and measurement of very small high speed particles because of the noise reduction inherent in the system. The deflection system is most useful in cases where

it is desirable to protect the target from bombardment by particles possessing characteristics other than those within a given range. Also, certain types of experiments require extensive post-bombardment analysis, and the ability to preferentially select certain parameters in advance would reduce the time spent in the analysis of redundant or unnecessary data.

In the present system, the selection mechanism is based strictly on a velocity measurement. This determines particle mass to an accuracy determined by variations in the charging mechanism. If such variations are excessive, the system can be modified to eliminate them. This can be accomplished by adding the requirement that the signal amplitude lie within some small interval. This is equivalent to specifying a charge interval. The simultaneous specification of particle charge and velocity is sufficient to specify particle mass for a given accelerating voltage. Although this refinement has not been included in the present system, it is clear that addition of this feature is a straightforward process.

REFERENCES

1. J. F. Friichtenicht, Rev. of Sci. Instr., Vol. 33, 1962, 209-212.
2. J. F. Friichtenicht, Nuclear Instruments and Methods, Vol. 28, 1964, 70-78.
3. Shelton, Hendricks and Wuerker, Journ. of Appl. Phys., Vol. 31, 1960, 1243-1246.
4. D. O. Hansen, STL Report 4158-6008-TU-000, Velocity Selector for an Electrostatic Hypervelocity Accelerator, April 1965.
5. D. O. Hansen, STL Report 4158-6005-TU-000, Solid State High Voltage, March 12, 1965, to be published in Electronics.

SOLID STATE HIGH VOLTAGE PULSER

APPENDIX E

TECHNICAL REPORT

SOLID STATE HIGH VOLTAGE PULSER

12 March 1965

Prepared for
National Aeronautics and Space Administration
Washington, D. C. 20546

Contract No. NASw-936



Prepared by
D. O. Hansen



Approved by
J. F. Friichtenicht
Manager
Meteoritics Department

PHYSICAL ELECTRONICS LABORATORY
Physical Research Division
TRW Space Technology Laboratories
Thompson Ramo Wooldridge Inc
One Space Park, Redondo Beach, California

SOLID STATE HIGH VOLTAGE PULSER

David O. Hansen

TRW Space Technology Laboratories, Redondo Beach, California

The diagram of a circuit which will produce a moderately fast rising high voltage pulse is shown in the accompanying figure. Some of the advantages of this circuit are: all solid state components, and therefore no filament supplies, etc.; low voltage requirements at the input for turn-on; with the rapidly increasing BV_{CEO} of PNP transistors, the availability of either polarity pulse without transformer coupling; the inherent protection against high voltage breakdown provided by the biasing arrangement.

The biasing arrangement, which is very simple, guarantees that the voltage across each transistor will always be less than some fraction of the supply voltage set by resistive dividers, R_3 , R_4 , and R_5 . If very long pulses are required, then the backup capacitors, C_1 , C_2 , and C_3 should be increased.

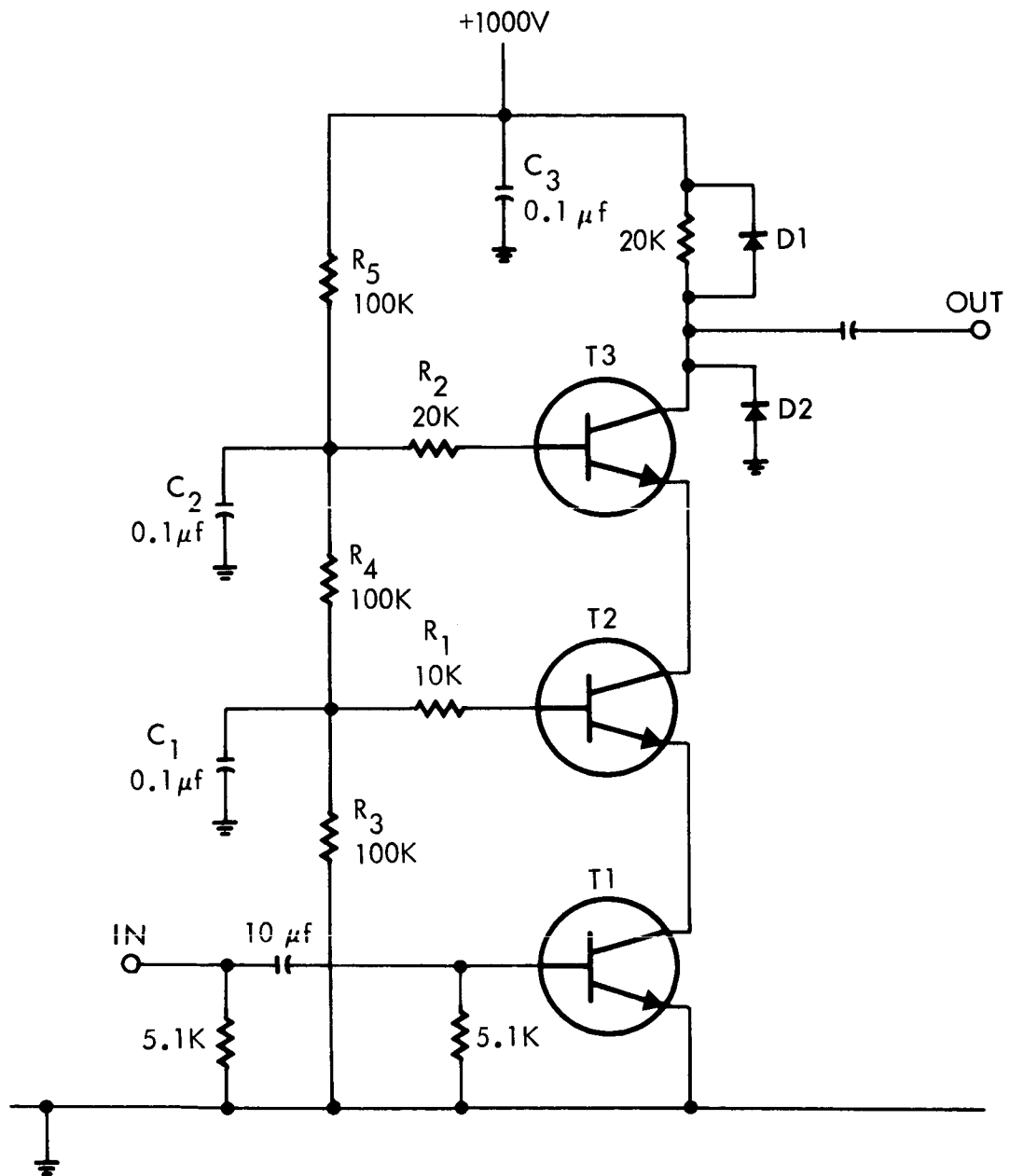
The operation of the circuit is as follows. A positive pulse of approximately 2 or 3 volts at the input switches T_1 on. A simple emitter follower is very adequate for driving T_1 . When T_1 starts to conduct, its collector voltage falls. This turns on T_2 because of the base current now flowing to T_2 through R_1 . The same thing happens when the collector of T_2 falls, switching on T_3 with base current through R_2 . The switching times of T_2 and T_3 are limited only by the f_a of the transistors, since they are switched with emitter drive. Therefore, the switching speed of the complete circuit is limited almost entirely by the switching of T_1 .

*This circuit developed in connection with work being conducted on hypervelocity impact phenomena under NASA Contract NASw-936.

Diodes D_1 and D_2 are high voltage rectifier diodes with breakdown voltages greater than the supply voltage. They protect the transistor string from spurious high voltage spikes that may be fed back from the circuit being driven with the output pulse. The protection afforded by the diodes depends upon their switching time from off to on. Since this is quite fast even for slow rectifier diodes, they may be used.

This circuit was constructed and used as a driving source for a 20-kv pulse tube. 2N3439 transistors were used. The rise and fall times of the pulse were approximately 800 nsec. These times could be decreased by using higher frequency transistors, and in particular, a faster switching transistor for T_1 .

ro



T₁ TO T₃ 2N3439

A NOVEL HIGH VOLTAGE PULSE GENERATOR

APPENDIX F

TECHNICAL REPORT

"A NOVEL HIGH VOLTAGE PULSE GENERATOR"

15 April 1965

Prepared for
National Aeronautics and Space Administration
Washington, D. C. 20546

Contract No. NASw-936

J. F. Friichtenicht

Prepared by
J. F. Friichtenicht

and

D. O. Hansen

D. O. Hansen

D. B. Langmuir

Approved by
D. B. Langmuir
Director

PHYSICAL ELECTRONICS LABORATORY
Physical Research Division
TRW Space Technology Laboratories
Thompson Ramo Wooldridge Inc.
One Space Park, Redondo Beach, California

A NOVEL HIGH VOLTAGE PULSE GENERATOR*

J. F. Friichtenicht and D. O. Hansen
TRW Space Technology Laboratories, Redondo Beach, California

This note describes a high voltage pulse generator that was developed in connection with research being carried out on hypervelocity impact phenomena.¹ Our requirements were a 20-kilovolt pulse delivered to a capacitive load of 100 pf, with rise and fall times of one μ sec or less, and a pulse width range of 10-100 μ sec. The pulse generator contains all solid-state components, except for the output pulse tube, and is simple in design and construction. A 3-volt pulse is sufficient to drive the generator and consequently it can be driven directly from low-level solid-state circuits.

Figure 1 is a circuit diagram of the generator which consists of 2 basic stages. The first is the transistor string composed of Q_{1-3} and its associated circuitry.² The second is the high voltage pulse tube. The biasing arrangement composed of R_{1-5} , while quite simple, achieves two very important results. It allows the switching action of the transistors to occur as described below, and at the same time prevents the voltage across any transistor Q_{α} from exceeding that across its bias resistor R_{α} . This prohibits transistor breakdown due to excessive collector-emitter voltage. Diodes D_{1-2} protect the string from spurious pulses fed back from the pulse tube grid, etc., which might destroy the string by exceeding the maximum BV_{CEO} of the transistors. The protection afforded by D_{1-2} depends only upon their turn-on time, and since this is quite rapid for any diode, ordinary rectifier diodes may be used.

* This circuit developed in connection with work being conducted on hypervelocity impact phenomena under NASA Contract NASw-936.

¹ J. F. Friichtenicht, "Micrometeoroid Simulation Using Nuclear Accelerator Techniques", Nuclear Inst. and Methods (1964) Vol. 28 pp 70-78.

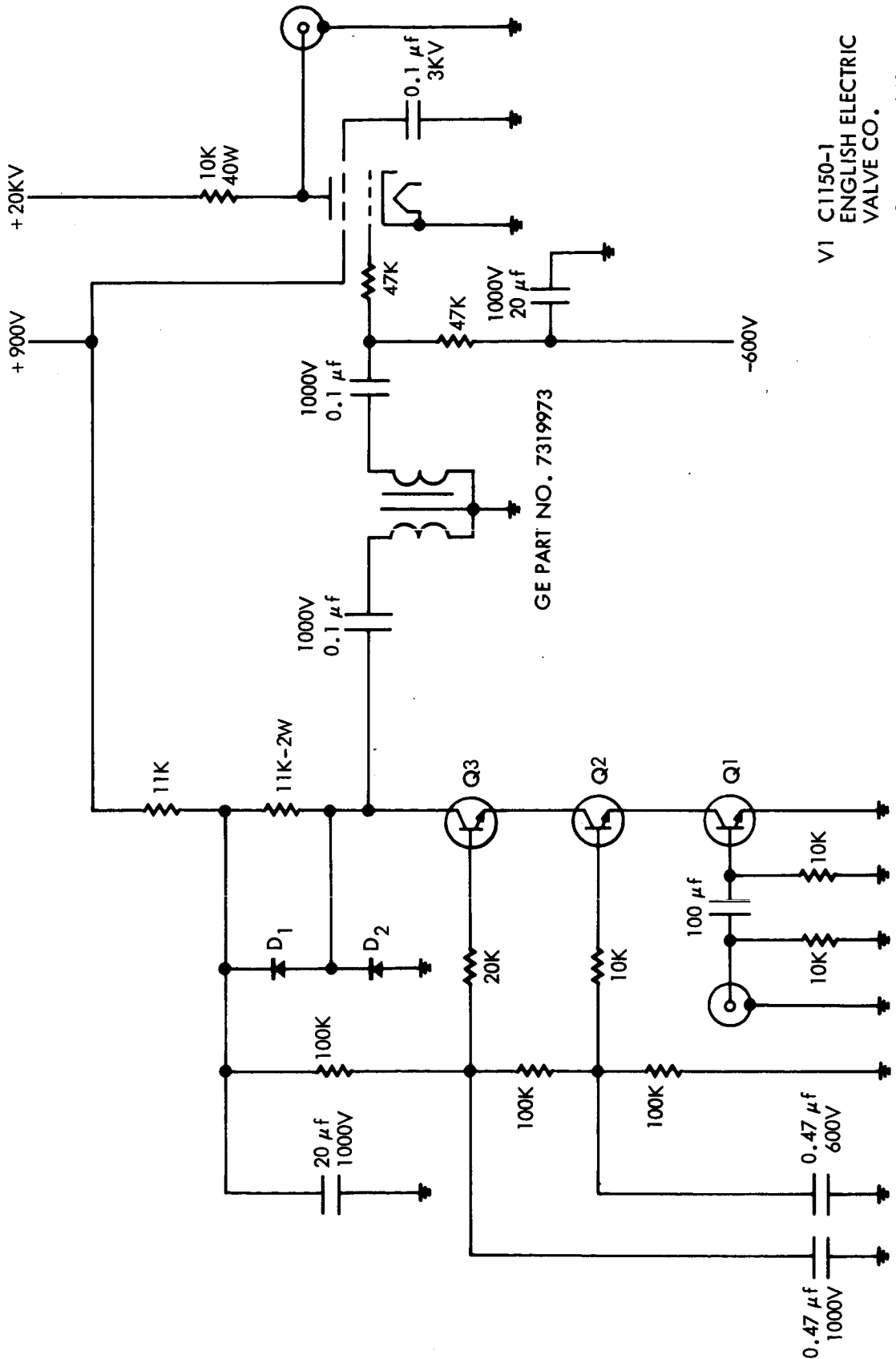
² D. O. Hansen, "Solid State High Voltage Pulser", 4158-6005-TU-000, Contract No. NASw-936, TRW Space Technology Laboratories, Redondo Beach.

A positive rectangular pulse is applied to the base of Q_1 which turns it on. As Q_1 comes on its collector voltage falls, carrying the emitter of Q_2 down also. This turns on Q_2 because of the base current drawn through R_3 . Q_3 is turned on in a similar fashion. When this switching action is complete, all of the transistors are in saturation. Upon termination of the pulse at the base of Q_1 , the reverse procedure takes place. Therefore, the signal at the collector of Q_3 is a negative rectangular voltage pulse with an amplitude nearly equal to the supply voltage. This pulse is delivered to the grid of the high voltage pulse tube by an inverting 1:1 pulse transformer.

The high voltage pulse tube is conventional in all respects. The pulse from the transistor string is delivered to the grid, driving it positive and saturating the tube. The plate falls essentially to ground with a rise time determined by the time required to charge the load capacitance with the plate current. When the pulse is removed from the grid, the plate returns to the supply voltage with a fall time determined by the RC time constant of the effective load resistance and the load capacitance.

The rise and fall times of the output pulse were about 900 nsec which was adequate for our purposes. If shorter rise and fall times are required, both stages of the pulse generator can be improved. Pulse tubes rated at 75 amperes or more are readily available and these are capable of providing rise times of 50 nsec or less into a 100 pf load. The switching time of the transistor string can be improved also. It will be noted that Q_2 and Q_3 are turned on with emitter drive, and therefore their switching times are limited only by their f_α . Q_1 is switched with base drive and almost entirely limits the rise and fall times of the string. If transistors with high f_α are chosen for Q_2 and Q_3 and a fast switching transistor is chosen for Q_1 , short rise and fall times may be obtained from the transistor string. Fast switching high voltage transistors are rare, but it is not

necessary that the voltage division across the transistors be equal. Q_1 may be given a small collector-emitter voltage of perhaps 20 volts. Transistors are available with very fast switching speeds at these voltage ratings. The pulse transformer which also limits the output rise times, may be completely eliminated as shown in Fig. 2 by the use of PNP transistors in the string. Their output is then a positive pulse which may be capacitively coupled to the grid. This also removes the limitation on maximum pulse length which the transformer imposes.



V1 C1150-1
ENGLISH ELECTRIC
VALVE CO.
Q1 TO Q3 2N3439

Figure 1.

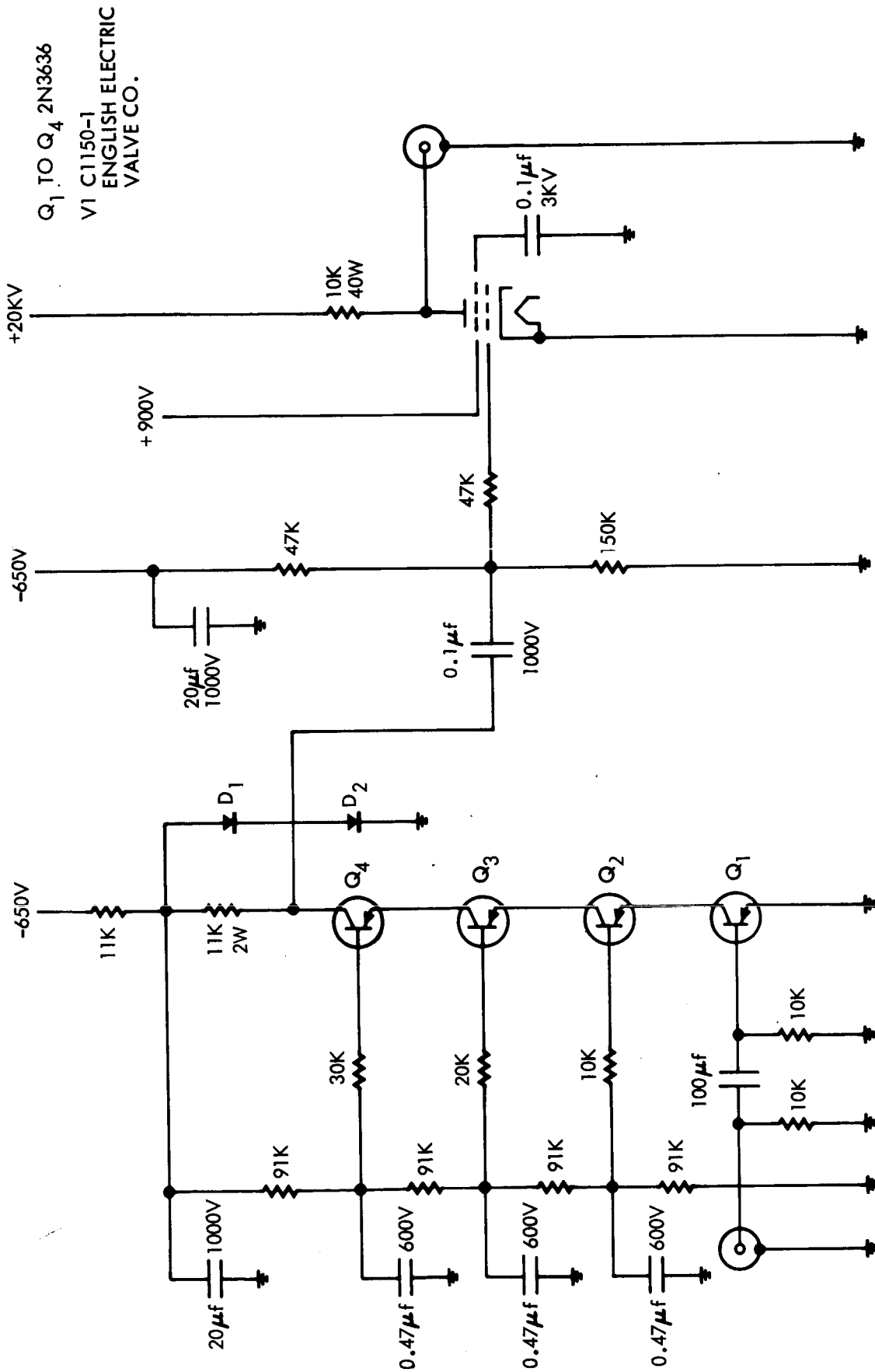


Figure 2.

**ELECTRONIC PARTICLE-PARAMETER ANALYZING SYSTEM
FOR AN ELECTROSTATIC HYPERVELOCITY PROJECTOR**

APPENDIX G

TECHNICAL REPORT

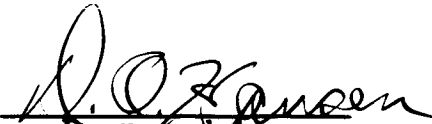
"ELECTRONIC PARTICLE-PARAMETER ANALYZING SYSTEM
FOR AN ELECTROSTATIC HYPERVELOCITY PROJECTOR"

July 1965

Prepared for

National Aeronautics and Space Administration
Washington, D. C. 20546

Contract No. NASw-936


Prepared by
D. O. Hansen


Approved by
J. F. Friichtenicht
Manager, Meteoritics Dept.

PHYSICAL ELECTRONICS LABORATORY
Physical Research Division

TRW Systems
One Space Park, Redondo Beach, California

ELECTRONIC PARTICLE-PARAMETER ANALYZING SYSTEM FOR AN ELECTROSTATIC HYPERVELOCITY PROJECTOR

I. INTRODUCTION

Refinements of equipment and techniques used with the TRW electrostatic hypervelocity accelerator¹ have enhanced its performance and increased its versatility. Detector preamplifiers have been improved to the point that much higher-velocity particles may be detected. In addition, a high-repetition-rate particle injection system has been developed for use in experiments requiring a large particle flux.

One complication that has arisen from improved accelerator performance is that the increasing rate of data acquisition has necessitated more complex computational procedures than those originally used. In general, particle parameters are determined from arithmetical computations involving the amplitude and duration of the detector signal and other system variables. Although the calculations are straightforward, they are time consuming, and this method is not practical for large volumes of data. This problem has led to the development of an automatic particle parameter analyzing system described below.

II. ELECTRONIC X-Y PLOTTER

The main component of the system that has been developed for automatic particle-parameter analysis is an electronic X-Y plotter. In this system each particle is represented by a point on a two-dimensional display. The displacement of the point along the Y axis is proportional to the charge on the particle, and the displacement in the X direction is proportional to its transit time through the detector. Since each particle is represented by a single point, rather than by a rectangular pulse as in the

former method, a large number of data points can be placed on a single display before confusion arises. As will be shown later, lines of equal radius and velocity can be drawn on the plot and will form a number of irregularly shaped areas, each of which correspond to a specific velocity and radius range. The radius and velocity of each particle can be determined fairly accurately by simply observing into which area the point falls.

A simplified block diagram of the X-Y plotter circuit is shown in Fig. 1. The pulse from the particle detector is fed to three separate circuits - a pulse stretcher, discriminator, and differentiating circuit. The pulse stretcher produces a pulse that has the same amplitude but is much longer than the input pulse. The stretched pulse is applied to the vertical amplifier of an oscilloscope and deflects the beam vertically by an amount equal to the original pulse height. The oscilloscope sweep is triggered when the detector pulse exceeds the threshold imposed by the discriminator. The negative pulse from the differentiating network, which occurs at the trailing edge of the detector pulse, is fed to the oscilloscope brightener-pulse generator. The brightener-pulse generator delivers a short-duration, rectangular voltage pulse to the cathode of the oscilloscope. In operation, the beam intensity control of the oscilloscope is adjusted so that the trace is visible only when the brightening pulse is applied to the cathode. Since brightening occurs at the trailing edge of the pulse, and at the same time the vertical displacement is proportional to detector pulse height, the position of the brightened spot gives the desired information.

A further refinement makes provision for the display of information regarding the effect of particle impact after the particle has passed through the detector. Generally this feature is restricted to a simple "yes-no" type of response. The mechanism for implementing this response is shown in Fig. 2. The stretched pulse is applied to the vertical input of the oscilloscope as before, but the output pulses from the differentiating network

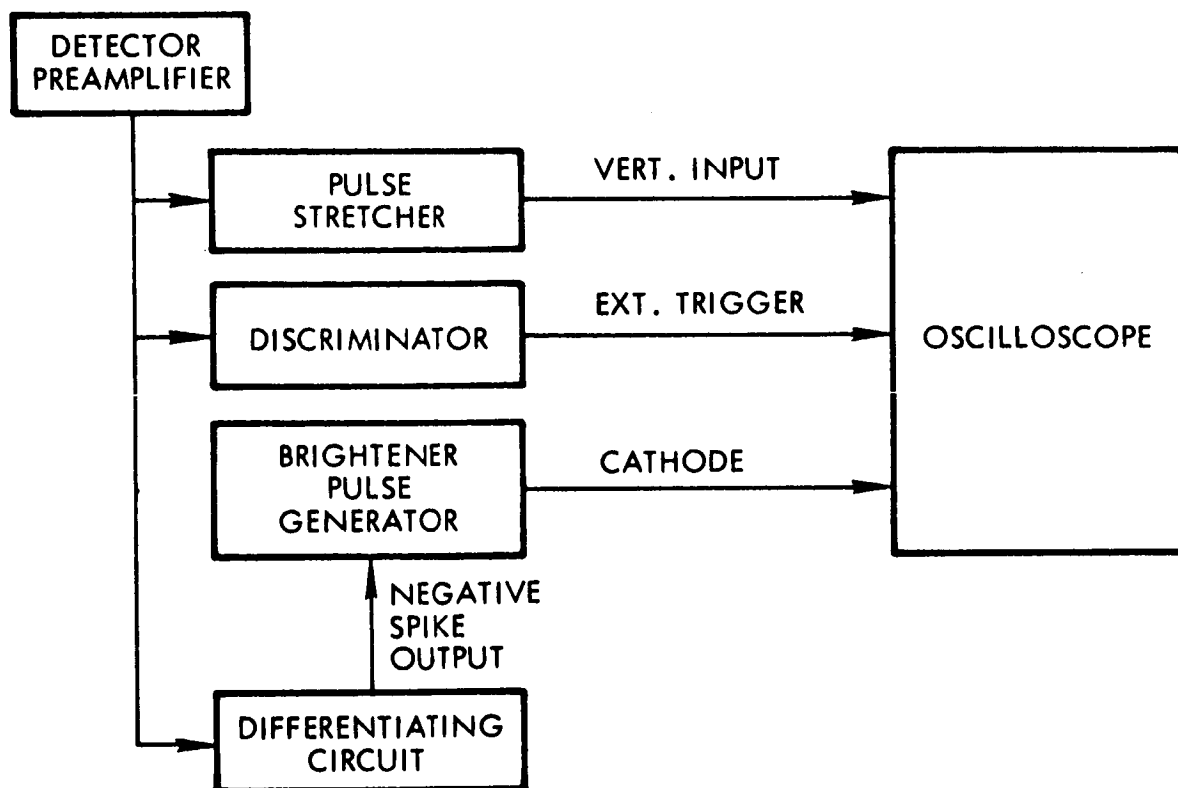


Figure 1. Simplified Block Diagram of the Basic X-Y Plotter

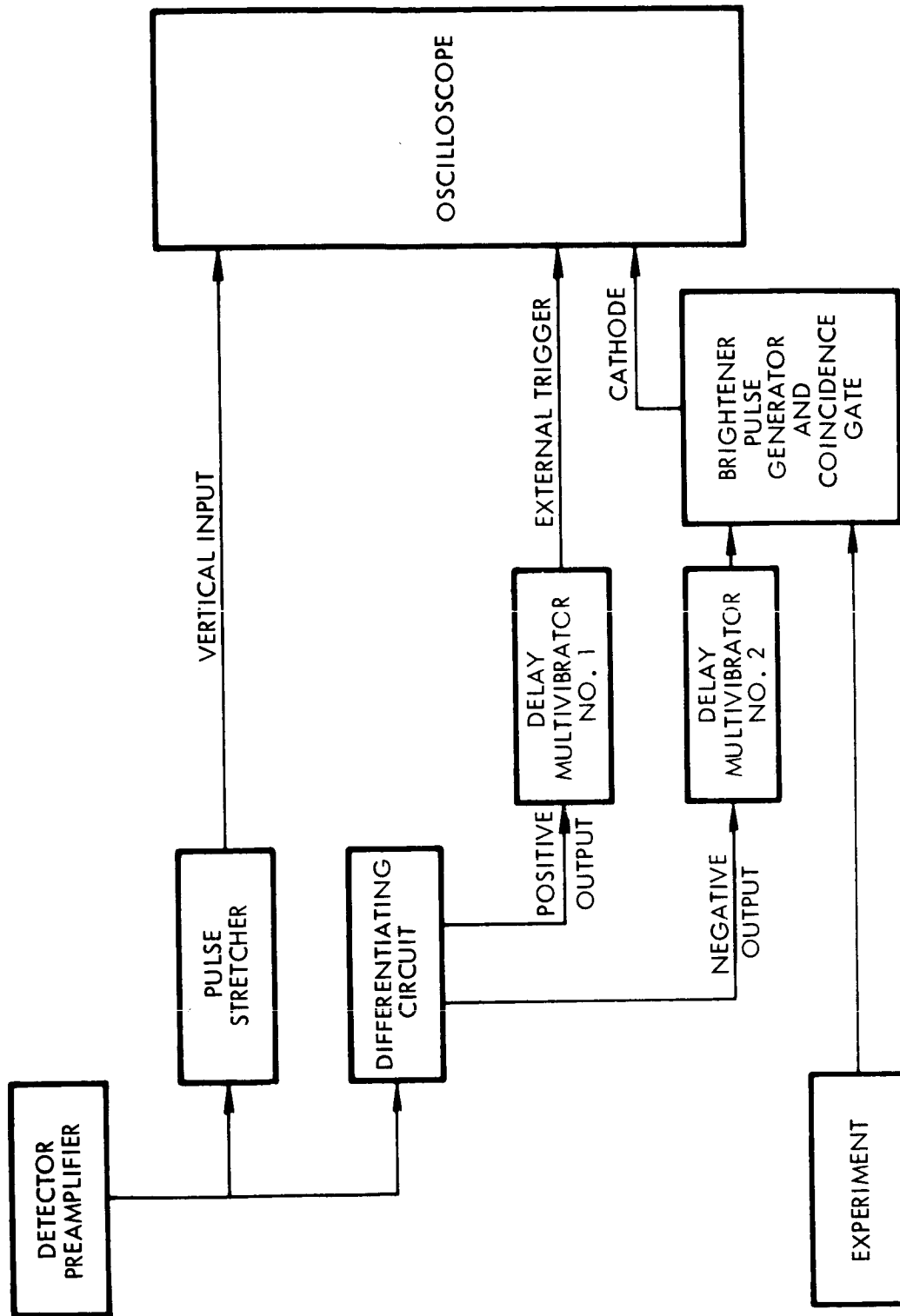


Figure 2. Block Diagram of the X-Y Plotter including the "yes-no" feature. In this application the output signal from the experiment must be characterized by a two-state response.

are applied to two 100- μ sec duration delay multivibrators. The first of these is triggered by the positive spike corresponding to the leading edge of the detector pulse while the second is triggered by the negative spike which occurs at the trailing edge of the detector signal. The trailing edge of the output pulse from the first multivibrator is used to trigger the horizontal sweep of the oscilloscope. The differentiated pulse from the second multivibrator is fed to the oscilloscope trace brightener unit. If no further input is provided to the trace-brightener, the trace is brightened in exactly the same manner as described above except that it is delayed by 100 μ sec.

The "yes-no" feature is characterized by changing the duration of the trace-brightener pulse. The electrical signal from the experiment in question is applied to an electronic gate and, if it appears in the time interval specified by the duration of the delay multivibrators, the output pulse from the trace-brightener is several times longer. This results in points being plotted for "no" events and short lines being recorded for "yes" events. The analysis of particle parameters is the same in either case. This feature has been particularly useful in experiments which have been conducted on the initiation of voltage breakdown by particle impacts.²

III. PARTICLE-PARAMETER ANALYSIS WITH THE X-Y PLOTTER

The amplitude of a detector signal (or the displacement of a point along the Y axis when using the X-Y plotter) is given by

$$V_o = \frac{qG}{C_d} \quad , \quad (1)$$

where V_o is the signal amplitude in volts, q is the particle charge, C_d is the capacitance of the detector, and G is the voltage gain of the preamplifier. Defining $V_o = yS_v$, where y is the amplitude in scale divisions and S_v is the sensitivity of the oscilloscope in volts/scale division, we get

$$q = y \left[\frac{S_v C_d}{G} \right] \quad (2)$$

Similarly, the duration of the signal (or X displacement is the transit time τ through a detector of known length L. From this we get

$$v = \frac{L}{\tau} = \frac{L}{x S_s} \quad (3)$$

where x is the signal length in scale divisions and S_s is the sweep sensitivity in seconds/scale division. Substituting into the conservation of energy equation,

$$1/2 mv^2 = qV_a \quad (4)$$

where m is the particle mass and V_a the accelerating voltage, and rearranging, we get

$$m = \left[\frac{2 S_v S_s^2 C_d V_a}{G L^2} \right] y x^2 \quad (5)$$

For spherical particles of density ρ , the radius r is obtained from

$$r^3 = \left[\frac{3 S_v S_s^2 C_d V_a}{2 \pi \rho G L^2} \right] y x^2 \quad (6)$$

For any given experiment the quantities in brackets are constant and are known. Thus we can write

$$\frac{r^3}{K} = y x^2 \quad (7)$$

Given the X and Y displacements of a given point, the radius of

the particle represented by the point is determined uniquely for a specified value of K . Furthermore, lines of equal radius can be specified by plotting curves of $yx^2 = \text{a constant}$.

To avoid the problem of generating and plotting new sets of curves each time K is changed, we introduce two new quantities - namely, a parametric radius R and an arbitrary constant K_1 such that

$$\frac{R^3}{K_1} = yx^2 \quad (8)$$

By choosing an arbitrary value of K_1 and letting R take on different values, we can plot a family of equal- R curves. From Eqs. (7) and (8) we see that

$$\frac{R^3}{K_1} = \frac{r^3}{K}, \text{ or } r = \left[\frac{K}{K_1} \right]^{1/3} R \quad (9)$$

The curves generated for R are universal. Once a specified value for K is determined, the equal- R curves may be relabeled by use of Eq. (9).

This procedure is illustrated in Fig. 3. First a set of equal- R curves, with R taking values from 1 through 8 and $K_1 = 5$, were plotted. Then the data points recorded from a typical oscilloscope photograph were plotted on the same graph. For this run $K = 2.84 \times 10^{-20}$. From Eq. (9), r was determined to be $0.178R$ microns. The appropriate labels are shown in the figure.

It should be recognized, also, that the displacement of a point in the X direction is proportional to reciprocal velocity. Hence the velocity and radius of a particular particle can be determined to some degree of accuracy by inspection. The radius of a particle can be determined more accurately by interpolation along a line from the origin to the point. Substituting the

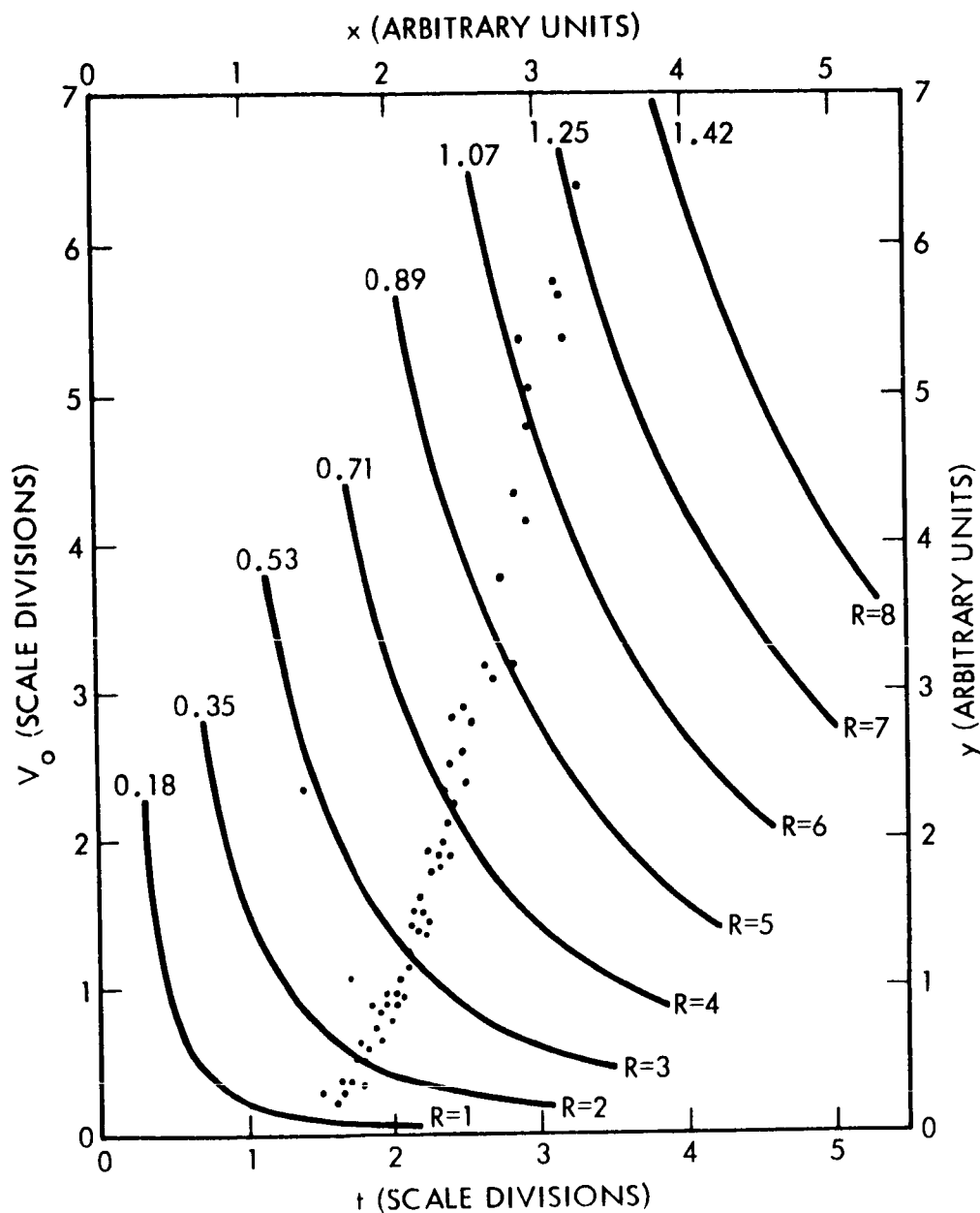


Figure 3. Example of Particle Parameter Analysis using the X-Y Plotter. The Equal R Curves were generated from $R^3 = 5 \times y^2$. The data points were transferred from a photographic record of a typical run. The actual particle radius in microns represented by each R curve is noted at the left-hand terminus of each R curve.

equation of such a line, $y = Cx$, into Eq. (7) yields $r = x(CK)^{1/3}$. Thus measurement of the slope C and the X displacement yields r precisely.

To facilitate measurements, an oscilloscope graticule with equal- R curves etched on it has been prepared. Since the data may be read directly from the photograph, the necessity of transposing the data points has been eliminated.

REFERENCES

1. J. F. Friichtenicht, Rev. of Sci. Instr., Vol. 33, p. 209 (1962).
2. J. F. Slattery, J. F. Friichtenicht and D. O. Hansen, Appl. Phys. Letters, Vol. 7, No. 1, p. 23, July, 1965.

**MICROMETEOROID SIMULATION USING NUCLEAR
ACCELERATOR TECHNIQUES**

APPENDIX H

MICROMETEOROID SIMULATION USING NUCLEAR ACCELERATOR TECHNIQUES

J. F. Friichtenicht, TRW Space Technology Laboratories

ABSTRACT

A two-million volt Van de Graaff accelerator has been modified so as to accelerate microparticles (dimensions the order of microns) to high velocities for micrometeoroid simulation. The modification will be described and the program of research on the physics of high speed impact, which has been undertaken using the facility, will be discussed.

"MICROMETEOROID SIMULATION USING NUCLEAR ACCELERATOR TECHNIQUES"

I. INTRODUCTION

It has been well established that the spatial environment is populated with a class of particulate matter referred to as meteoroids. The existence and properties of these meteoroids have been inferred from studies of the zodiacal light and observations of meteor trails in the earth's atmosphere. More recently, artificial earth satellites and probes have provided platforms from which direct measurements could be made. The origin, composition, and properties of meteoroids are of interest from a strictly scientific point of view. The same properties also concern the spacecraft designer since collisions with such bodies are a definite hazard to space vehicles.

Although the size of meteoroids varies over wide limits, it appears that the bulk of the matter exists in the form of small particles referred to as micrometeoroids. The smallest micrometeoroids may have dimensions the order of a few tenths of a micron or so. Their velocities relative to a spacecraft may be anywhere from zero up to about 85 km/second, depending upon the orbits of the micrometeoroids and the spacecraft. Interpretation of the direct measurements from space satellites and observations of meteor trails has been hampered by the lack of suitable test and simulation facilities and the lack of knowledge concerning the properties of high speed impact.

As a consequence of the requirements for micrometeoroid simulation, members of the Physical Research Division of TRW/STL have been conducting research in this area since 1957. This work has resulted in the development of a device where small grains of matter are charged electrically and accelerated to high velocities by electric fields. The major components of this device are a charged particle injector and a High Voltage Engineering Corporation two-million volt Van de Graaff accelerator. The accelerator has been used in a program of micrometeoroid research since early 1961. The objective of this paper is to describe the operation of this equipment and to give a summary of some of the work which has been accomplished with it.

Applications of the accelerator to meteoroid simulation have proved to be many and varied. Some of the areas of interest in which research has been conducted or contemplated can be placed in the following arbitrary categories.

1. Micrometeoroid detector development program.
2. Meteoroid penetration studies.
3. Effects on spacecraft components and materials.
4. Simulation of meteors.

A brief description of some of the work accomplished in each of these areas will be given below.

II. THE ELECTRIC ACCELERATOR FOR METEOROID SIMULATION

The electrostatic meteoroid accelerator is similar in most respects to conventional low energy ion accelerators; the only major difference being the mechanism by which the particles are charged and the particles themselves. The velocity obtained by a charged particle is given by

$$v = (2q V/m)^{1/2} \quad (1)$$

where q is the charge on the particle, m is the particle mass, and V is the accelerating voltage. The final velocity, therefore, is limited only by the magnitude of the accelerating voltage and the charge to mass ratio of the particles. The magnitude of the voltage used in an electric accelerator is usually limited by economic considerations while the maximum charge to mass ratio is a more fundamental limitation.

In the particle charging mechanism developed by Shelton et al,¹ the particles to be charged are allowed to come in contact with a small charging electrode which is maintained at a high positive voltage with respect to its surrounding surfaces. This is accomplished by a device illustrated schematically in Fig. 1. The particles to be charged, in the form of a fine powder, are stored in a box-like cavity. A flat rectangular plate is supported in a plane parallel to the surface of the powder and is normally maintained at the same electrical potential. When a voltage pulse is applied to this tongue, an electric

field is produced between the tongue and the particles on the surface. The electric field induces a charge on the particles and if the electrical forces are sufficient to overcome inter-molecular and gravitational forces, some of them will be lifted from the powder. When they strike the tongue they become charged in the opposite direction and are repelled from the tongue. In other words, application of a voltage pulse puts some of the particles in motion. Their behavior is similar to that of molecules in a gas and because of collisions with walls and other particles, some of them will effuse out of the small hole and enter the region occupied by the charging electrode. In this region, each time a particle comes in contact with a surface it acquires a charge of the same polarity as that of the surface and is repelled from it. Thus, particles injected into this region bounce back and forth between the two halves of the cavity. Because of this random motion some of the particles come in contact with the small charging electrode. Since the electric field at the surface of the charging electrode is much greater than the electric field on other surfaces within the cavity, the particles acquire a much larger charge. Some of the particles leaving the electrode are intercepted by the small aperture on the axis of the Van de Graaff accelerator tube. Those entering the accelerator tube are subsequently accelerated through the full potential difference of the accelerator.

The conversion of the conventional ion accelerator to a micro-particle accelerator is straightforward, and has been described in the literature.² The ion source and its control circuits are replaced by the charged particle injector and associated circuitry. A block diagram of the components within the high voltage terminal of the Van de Graaff is shown in Fig. 2.

The charge to mass ratio of the particle can be expressed in terms of the electric field at the surface of the particle by

$$\frac{q}{m} = \frac{3\epsilon_0 E}{\rho r} \quad (2)$$

where ϵ_0 is the permittivity of free space, ρ is the density, and r is the radius of the particle. In turn, it can be shown that the

field of the particle after separation and charge redistribution is proportional to the field on the charging electrode. The maximum field to which the particle is subjected occurs when the particle is in contact with the charging electrode. The limit of the charge to mass ratio obtainable is determined by the maximum field which the particle can sustain while in contact with the charging electrode. Good and Mueller³ report that most metals are able to support positive fields in excess of 10^{10} volts/meter. Beyond this limit, appreciable ion evaporation occurs. Because of geometrical factors, sputtering, and other effects this upper limit is generally not achieved. However, we have been able to consistently charge particles to a value such that the surface electric field is about 2.5×10^9 volts/meter.

From Eq. 2 it can be seen that higher charge to mass ratios are obtained for smaller particles and also for low density materials. For most of our work we have used carbonyl iron spheres which are readily available in the correct size range. A more limited amount of work has been done with carbon black particles which, because of their reduced density, obtain considerably higher velocities. The performance of the TRW/STL electrostatic accelerator under nominal operating conditions is illustrated in Fig. 3. Clearly the velocity and mass ranges available do not match the natural meteoroid spectrum. However, the area of overlap is sufficient to allow useful experimentation.

The presence of charge on the accelerated particles has led to the development of electronic detectors for the measurement of particle velocity, charge, and mass. A detector consists of an insulated drift tube mounted coaxially with the beam of particles from the Van de Graaff. The passage of a charged particle through the detector induces a voltage on the detector which is proportional to the charge on the particle and inversely proportional to the capacitance of the detector to ground. The duration of the signal is simply the transit time of the particle through the detector while the amplitude is proportional to the particle charge. In operation, the signal from the detector is amplified and displayed on an oscilloscope and photographed for later analysis. Having measured

the particle velocity and charge and knowing the voltage through which it has been accelerated, the mass of the particle is computed from Eq. 1.

In summary, some of the features which make an electric accelerator particularly adaptable for micrometeoroid simulation are as follows:

1. The entire experiment may be conducted in a vacuum environment.
2. The frequency of injection of particles and the number of particles injected are controlled electrically.
3. The particle parameters of each particle are measured electronically prior to impact.
4. High repetition rates may be obtained thus providing rapid data acquisition.
5. Due to the non-destructive accelerating technique, reliable operation is obtained with minimum down time.

III. DETECTOR DEVELOPMENT PROGRAM

The problem of determining micrometeoroid parameters by means of instruments aboard earth satellites is not trivial. The detection process can be characterized as the remote analysis of a high speed collision between bodies, where the parameters of one of the bodies is completely undetermined. In most instances the response of the detection system to the event is not known. The objective of the detector development program is to assist in the development of sensors by the investigation of those properties of high speed impact which are appropriate. This facility is also used for tests and calibration of completed sensor units.

Since the recovery of instruments from satellite vehicles is complicated and expensive, it is clear that sensors which respond to some transient effect occurring upon meteoroid impact would be desirable. Consequently, most of our work has been concerned with this type of effect. As an example, consider the impact ionization process. We have concluded that some of the atoms near the impact site of a high speed particle are ionized by the large energy release associated with the impact. The emitted charge, which is either

positive or negative, can be collected by means of electrically biased collectors and the resulting signal may be used in various types of meteoroid detectors. The quantity of charge emitted depends upon particle velocity and mass, and upon characteristics of the materials in question. An experimental study of this effect was undertaken and some of the results are illustrated in Figs. 4 and 5. These data were obtained by allowing particles from the accelerator to pass through a grounded grid and impact upon the surface of a thick target, which was biased relative to the grid. A sensitive preamplifier was connected to the target and the total charge leaving the target was measured. For the cases illustrated here, the target was biased negative with respect to the grid so that the signal represented the emission of negative charge from the target. However, the results of opposite bias, which measures the emission of positively charged particles, are virtually indistinguishable from these data.

Figure 4 shows the total charge emitted, normalized to N , the number of atoms in the impacting particle as a function of particle velocity for a tungsten target. Both iron and carbon particles were used in this experiment. It is found that a good empirical fit is obtained to these data by an expression of the form

$$q_c = \frac{KE_p v}{A} \quad (3)$$

where E_p is the kinetic energy of the particle, v the particle velocity, and A the molecular weight of the particle atoms. All of the target materials examined appeared to fit this particular relationship.

The material dependence is illustrated in Fig. 5. Here we show smoothed curves of the type illustrated in Fig. 4 for several target materials. It can be seen that the materials examined fall into two distinct categories. More charge is emitted from the tantalum, tungsten and platinum targets than from targets of copper, beryllium-copper, indium and lead. It is almost certain that the quantity of charge emitted is a function of more than one characteristic of the target material. Because of the complexity of the problem, no attempt has been made to explain material dependence as yet. However, certain characteristics of the materials exhibit a similar grouping.

For example, Ta, W, and Pt all have higher melting and vaporization temperatures than the others. Also, the same materials are classified as good thermionic emitters, while the others are not. Perhaps the most significant property of all is that of resistance to hypervelocity penetration. The craters produced in Pb, In, Cu, and Be-Cu are generally much larger than those in Ta, Pt and W. Investigations of this effect and similar effects are continuing.

The accelerator has been used for test and calibration of several sensor instruments. For example, we measured the crystal transducer response and the minimum sensitivity of the light flash detectors flown on Ranger I. These measurements have been reported by Alexander and Berg.⁴ A thin film penetration detector was flown on Explorer VII by LaGow and Secretan.⁵ Analysis of their data was contingent upon results obtained in laboratory tests with our equipment. At the present time, we are involved with NASA personnel on tests of a multi-parameter micrometeoroid detector system planned for the EGO series of spacecraft.

IV. METEOROID PENETRATION STUDIES

Although we have done very little work in the area of penetration studies, such work will become more necessary as increasingly ambitious space probes are developed. As noted before, meteoroids are a definite hazard to spacecraft and spacecraft must be protected from the effects of such impacts. Because the weight of protective shielding must be included in the weight of a final payload, it would be desirable to keep shielding weight to a minimum. A fairly good knowledge of meteoroid penetration capabilities is required to adequately assess the problem. Practically no experimental measurements on high velocity penetration at velocities in excess of 10 Km/sec exist. Present estimates of meteoritic penetration are based on the hydrodynamic model of hypervelocity impact first proposed by Bjork.⁶ The validity of this model has not been verified. The electrostatic accelerator has the capability of producing high speed particles in the velocity range of interest. In particular, the use of carbon particles results in velocities exceeding 20 km/sec which is in the regime where the Bjork

theory is applicable.

In conventional terminal ballistics studies, a crater is produced in a semi-infinite target and the dimensions of this crater are correlated with parameters of the impacting projectile. Because of the small size of the craters produced by particles from the electrostatic accelerator, sophisticated electron microscopy techniques must be employed in order to achieve quantitative results. Figure 6 is an electron micrograph of a crater produced in an aluminized glass target by the impact of a relatively low velocity iron particle. Clearly, the detail necessary for precise measurement is available. Figure 7 illustrates ordinary microphotographs of craters in a lead target. These craters are the order of 10 microns in diameter and are subject to precise measurement under properly controlled conditions.

V. EFFECTS ON SPACECRAFT COMPONENTS

In many instances, it is not possible to mechanically shield certain components of spacecraft. Aside from catastrophic damage, which is more properly treated under the preceding topic, the operation of such components could be adversely affected by continual micrometeoroid bombardment. For example, some surfaces are especially selected for specific thermal radiation properties for temperature control purposes. Changes of these properties by the erosive effects of micrometeoroid bombardment would ultimately upset the temperature balance and could seriously hamper spacecraft performance. Likewise, the surfaces of optical components would be damaged by such bombardment. Effects of this kind would not become important until an appreciable portion of the surface in question has been damaged. It is clear from present knowledge that this can occur only after an extended period in space.

In order to simulate this kind of damage in the laboratory, it is necessary to bombard the target sample with large numbers of particles. We have tested charged particle injectors capable of injecting particles at a rate in excess of 10 particles/second so that sufficient damage can be inflicted in a day or two of running time. Although we have not conducted these kind of experiments,

it is clear that they are feasible. The results of these experiments would be a valuable contribution to the art of designing spacecraft for long term operation.

In other types of equipment, the impact of a meteoroid could initiate transients which could effect the overall performance of the equipment. For example, an ion propulsion engine which utilizes the contact ionization concept exposes many vulnerable parts to micro-meteoroid bombardment. The effects of such bombardment can be broken up into short and long term effects. The latter would include erosion and pitting of surfaces and contamination by ingestion of meteoritic material. Short term or transient effects include micrometeoroid initiated electrical breakdown. Since ion engines operate close to the electrical breakdown point, an impact which causes charge emission in a manner similar to that described above might trigger a discharge. How damaging such a discharge might be would depend on the particular circumstances, the environment of ions and neutral atoms, the field strengths and voltages, surface conditions, as well as the size and location of the impact.

We are presently involved in assessing this particular problem. From preliminary results, it is clear that micrometeoroids are capable of initiating discharge under certain conditions. Whether such discharges pose a hazard to ion engine operation remains to be seen and will be the subject of more extensive research.

VI. SIMULATION OF VISUAL METEORS

As was mentioned earlier, much of what we know about the natural meteoroid spectrum was deduced from the observation of visual meteors. There is little doubt that the mechanism by which a meteoroid entering the earth's atmosphere produces a luminous trail is generally understood. The incoming particle, traveling at a high velocity, collides with atmospheric molecules at high altitudes. Because of molecular bombardment at relatively high energies, the particle quickly heats up until its temperature becomes limited by vaporization or ablation. Vaporized atoms carry with them the meteoroid velocity. These atoms become excited by collisions with atmospheric gas molecules and emit

visible radiation. Since the atmospheric density is low, the mean free paths are such that the evaporated atoms may radiate their excitation energy at large distances from the original meteoroid. A typical luminous trail is 10 or 20 kilometers long and several hundred meters in diameter. For most meteors the trail ends when the mass of the meteoroid has been vaporized.

There is widespread agreement on this general description, but the specific details of the various interactions involved are in doubt. Very little experimental data is available due, primarily, to the difficulty in performing experiments at hypervelocities and low gas pressures in the laboratory. For natural meteors, the aerodynamic flow is of the free molecular type, i.e., the mean free path of the gas molecules is much larger than particle dimensions. Thus, in order to simulate meteor phenomena with large high speed particles, the gas pressure of the target must be very low and the interaction distances required for experiments would be hundreds of meters long. With small particles, however, the pressure of the gas may be adjusted so that the experiment can be performed within a few meters. The interpretation of experiments conducted with very small particles is aided by the fact that the particle is at substantially the same temperature throughout because of the short thermal time constant. In general, this is not the case for natural meteors. On the other hand, the drag forces acting on a natural meteor do not slow it down appreciably. For small particles the change in velocity because of drag forces must be taken into account.

In the usual formulation of meteor physics, the phenomenon of visual meteors is described by three equations each containing an unknown constant. The first of these equations is the so-called drag equation which is given by

$$m \frac{dv}{dt} = -\Gamma \rho S v^2 \quad (4)$$

where m is the mass, v the velocity, ρ the atmospheric density, S the cross-sectional area of the particle, and Γ is the drag coefficient. The value of the drag coefficient depends upon the geometry of the particle and the exact nature of the interactions of the gas molecules with the surface of the particle. A second meteor equation is the energy balance equation which describes the ablation of the

meteor;

$$\zeta \frac{dm}{dt} = - \frac{\Lambda}{2} S \rho v^3 \quad (5)$$

where ζ is the heat of ablation or vaporization, and Λ is the fraction of incoming energy which heats the particle and is called the heat transfer coefficient. The third equation describes the intensity of light from a meteor trail and is given by

$$I = \frac{\tau}{2} \left(\frac{dm}{dt} \right) v^2 \quad (6)$$

where I is the light intensity and τ is the luminous efficiency.

In application of these equations to experiments, v , $\frac{dv}{dt}$, ρ , and I are measured by photographic techniques. Values of Γ , Λ , ζ , and τ are assumed. The value of m is obtained by the simultaneous solution of the three equations.

It can be recognized that the quantities Γ , Λ , and τ can be measured under certain conditions. In some respects the electrostatic accelerator is uniquely qualified for measurements of this kind. A fairly comprehensive investigation of this phenomenon has begun, and preliminary results have been reported by Slattery et al⁷. The experiments are accomplished by allowing particles from the accelerator to pass through a differential pumping system into a target chamber which is filled with gas at a few mm of Hg pressure. The flight of the particle through the gas can be followed by two methods. When the particle first enters the gas, it retains its charge and its position can be monitored by means of charged particle detectors similar to those described in Section II. At some point along its path, the particle absorbs sufficient energy to melt. At this time, the charge of the particle drops because a molten particle is unable to support the high field at its surface. Usually sufficient charge remains to continue measurements with the charged particle detector. Still later, the particle reaches vaporization temperature and the charge on the particle is lost very rapidly. However, prior to this time, radiation is being emitted which can be observed with photomultiplier tubes. From the onset of light emission, the position of the particle is monitored by a linear array of photomultiplier

tubes. This technique is applicable until the particle is completely vaporized or until it loses sufficient energy to stop radiating.

Our preliminary investigations have been concerned with measurements of the drag coefficient and the heat transfer coefficient under rather special conditions. The drag coefficient is determined by simply measuring the position as a function of time for a given particle and applying Eq. 4, above. We have measured the drag coefficient for gaseous targets of oxygen, argon, and air at pressures from one to two mm of Hg. In all cases the measured drag coefficient is nearly unity.

Values for the heat transfer coefficient were obtained for each of the target gases also. However, our measurements were made for the special case of a solid particle. For this special case, $\frac{dm}{dt}$ is zero and Eq. 5 does not apply. To find λ (defined as the heat transfer coefficient for a solid particle) we equate the energy required to melt the particle to the energy delivered over the time required for the particle to reach its melting point, i.e.

$$mC\Delta T = \int_0^T \frac{\lambda}{2} \rho A v^3 dt \quad (7)$$

where C is the specific heat and ΔT is the change in temperature. The integral was evaluated by direct measurement of v as a function of t for each particle. Assuming that the specific heat and the heat transfer coefficient are constants from room temperature to melting temperature, the values we obtained are as follows:

$$\begin{aligned} \lambda \text{ oxygen} &= 1.06 \pm 0.03 \\ \lambda \text{ argon} &= 0.90 \pm 0.08 \\ \lambda \text{ air} &= 0.86 \pm 0.07 \end{aligned}$$

It should be noticed that the value of λ for oxygen is greater than 1. This is not surprising since the iron of the particle and the oxygen can combine chemically to produce an apparent efficiency of greater than 100%.

Figure 8 illustrates the results of a typical experiment. It was from data like these that the values of λ and Γ were obtained. In Fig. 8, the velocity as a function of time was obtained by the

charged particle type of detector. The temperature curve was computed using the experimental data and Eq. 7. The temperature curve has not been corrected for radiation losses, but the energy loss by radiation is very small compared to the rate of energy input to the particle. The light intensity as a function of time was obtained by the array of photomultiplier tubes mentioned above, but was not used for quantitative measurements. It is shown simply to demonstrate at what point appreciable radiation is observed.

In some respects the measurements described in the preceding paragraphs can be classified as molecular beam physics where the roles of the target and the gas have been reversed. These experiments are equivalent to bombarding a target with molecular beams with energies of from 1 to about 10 eV. This range of energies is extremely difficult to obtain by other techniques and we feel that a great amount of work remains to be done in this particular area.

VII. SUMMARY

In the preceding paragraphs I have attempted to describe an accelerator whose operation and applicability to certain types of experiments is unique. The discussion has been in very general terms and it is reasonably certain that many other specific applications will be uncovered as research with this equipment continues.

Finally, I would like to acknowledge the contributions of my co-workers who were responsible for much of the work described above. These include D. G. Becker, Dr. B. Hamermesh, and Dr. J. C. Slattery. Also, the earlier work of Haywood Shelton, R. F. Wuerker and R. V. Langmuir made the construction of the accelerator possible. Much of the work described above has been conducted under NASA sponsorship.

REFERENCES

1. H. Shelton, C. D. Hendricks, Jr. and R. F. Wuerker, J. Appl. Phys., Vol. 31, 1234 (1960).
2. J. F. Friichtenicht, Rev. of Sci. Inst., Vol. 33, 209 (1962).
3. R. H. Good, Jr. and E. W. Mueller, Handbuch der Physik, Vol. 21, Springer-verlag, Berlin (1956).
4. W. M. Alexander and O. E. Berg, the Fifth Symposium on Hypervelocity Impact, Denver, Colorado, November 1961.
5. H. E. LaGow and L. Secretan, NASA Technical Note D-1722, April 1963.
6. R. L. Bjork, The Third Symposium on Hypervelocity Impact, Armour Research Foundation, October 1958.
7. J. C. Slattery, J. F. Friichtenicht and B. Hamermesh, AIAA Conference on Physics of Entry into Planetary Atmospheres, August 26-28, 1963, Cambridge, Massachusetts.

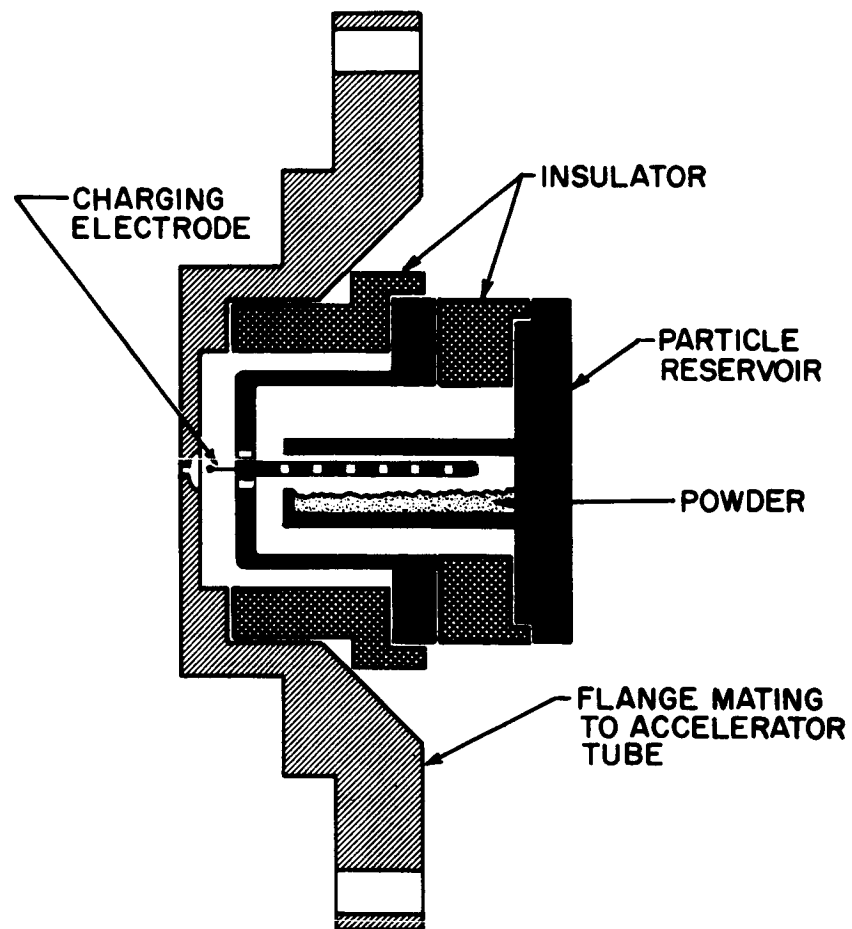


Fig. 1. The Charged Particle Injector.

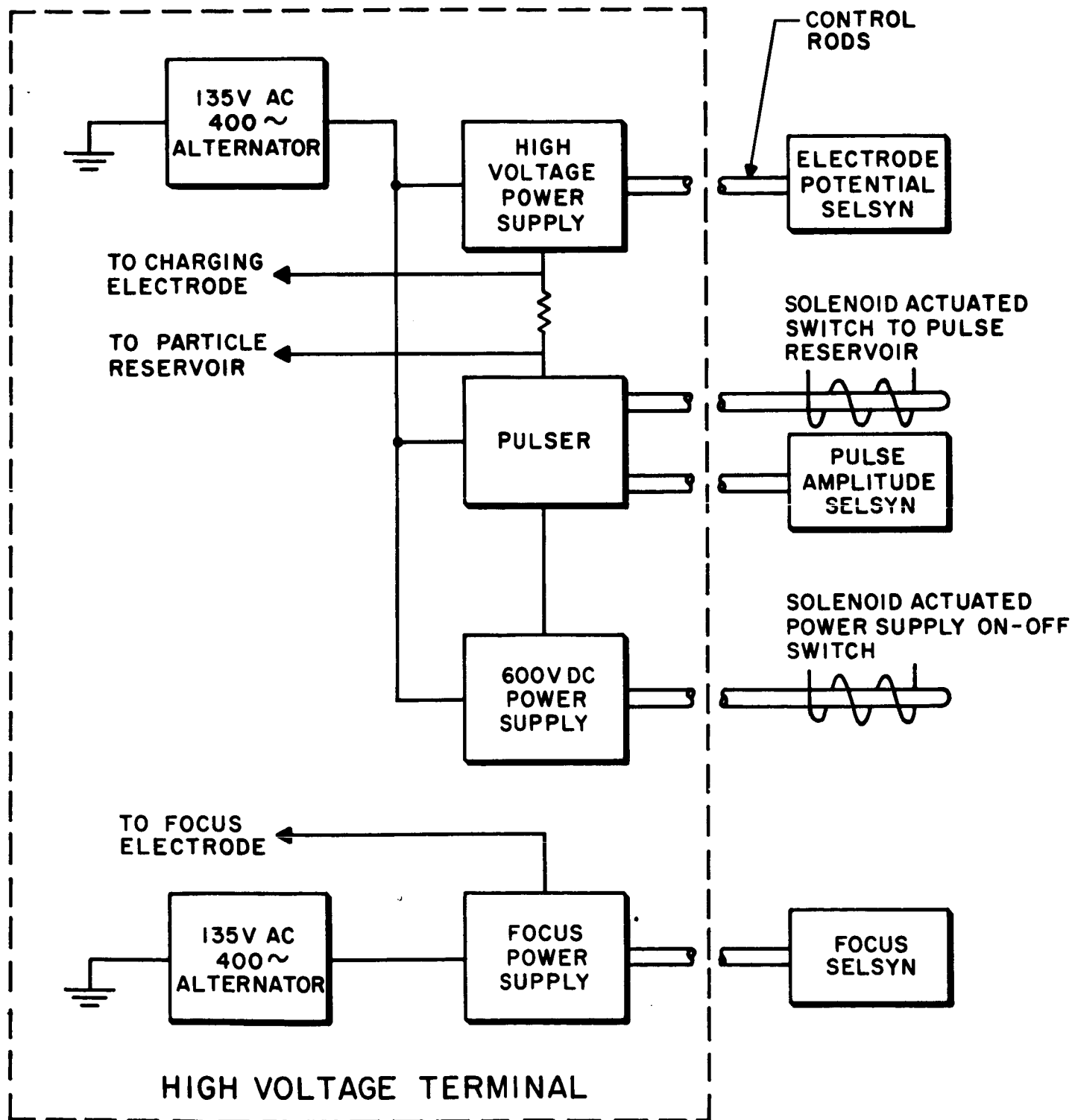


Fig. 2. Block Diagram of the High Voltage Terminal.

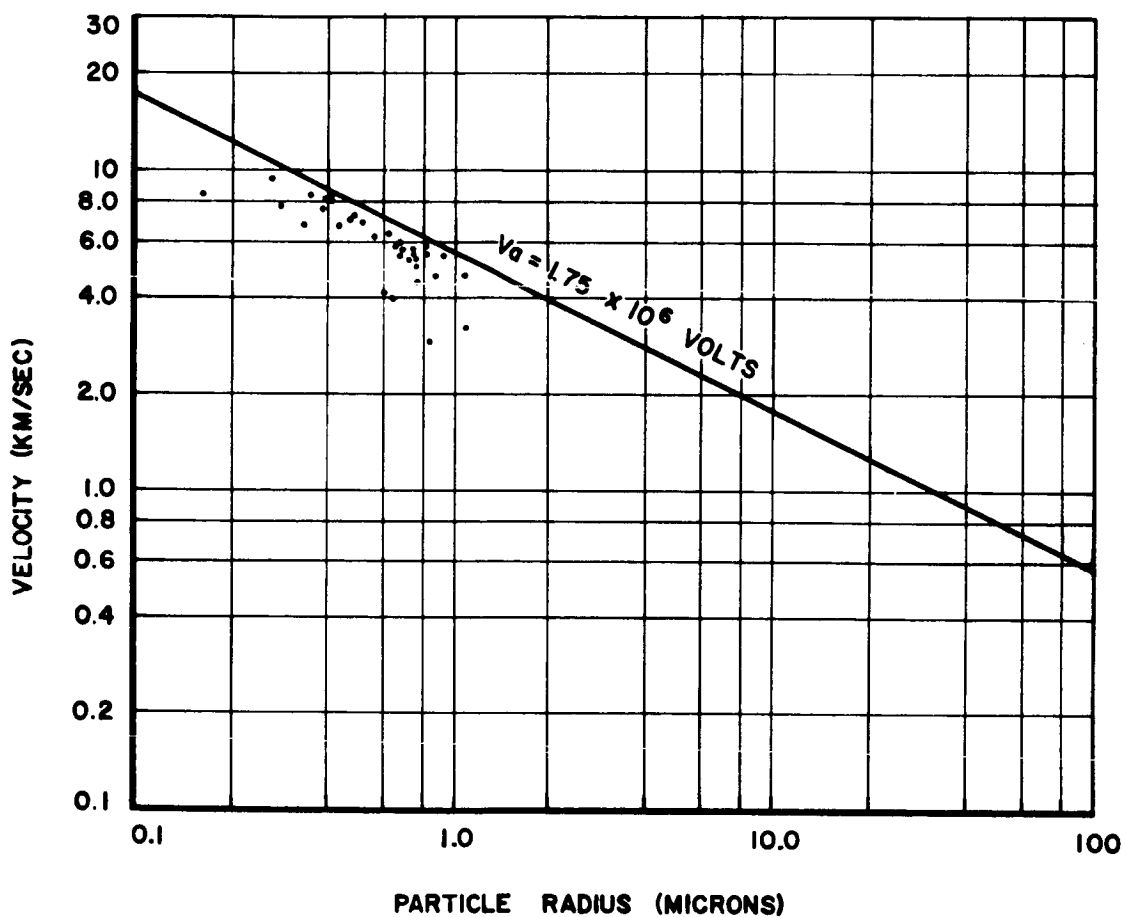


Fig. 3. Performance Curve for an Electrostatic Accelerator. The solid line is the expected performance for particles charged to a value that results in an electric field of 2.5×10^9 volts/meter at the surface of the particle. The points are the result of actual measurements under nominal conditions.

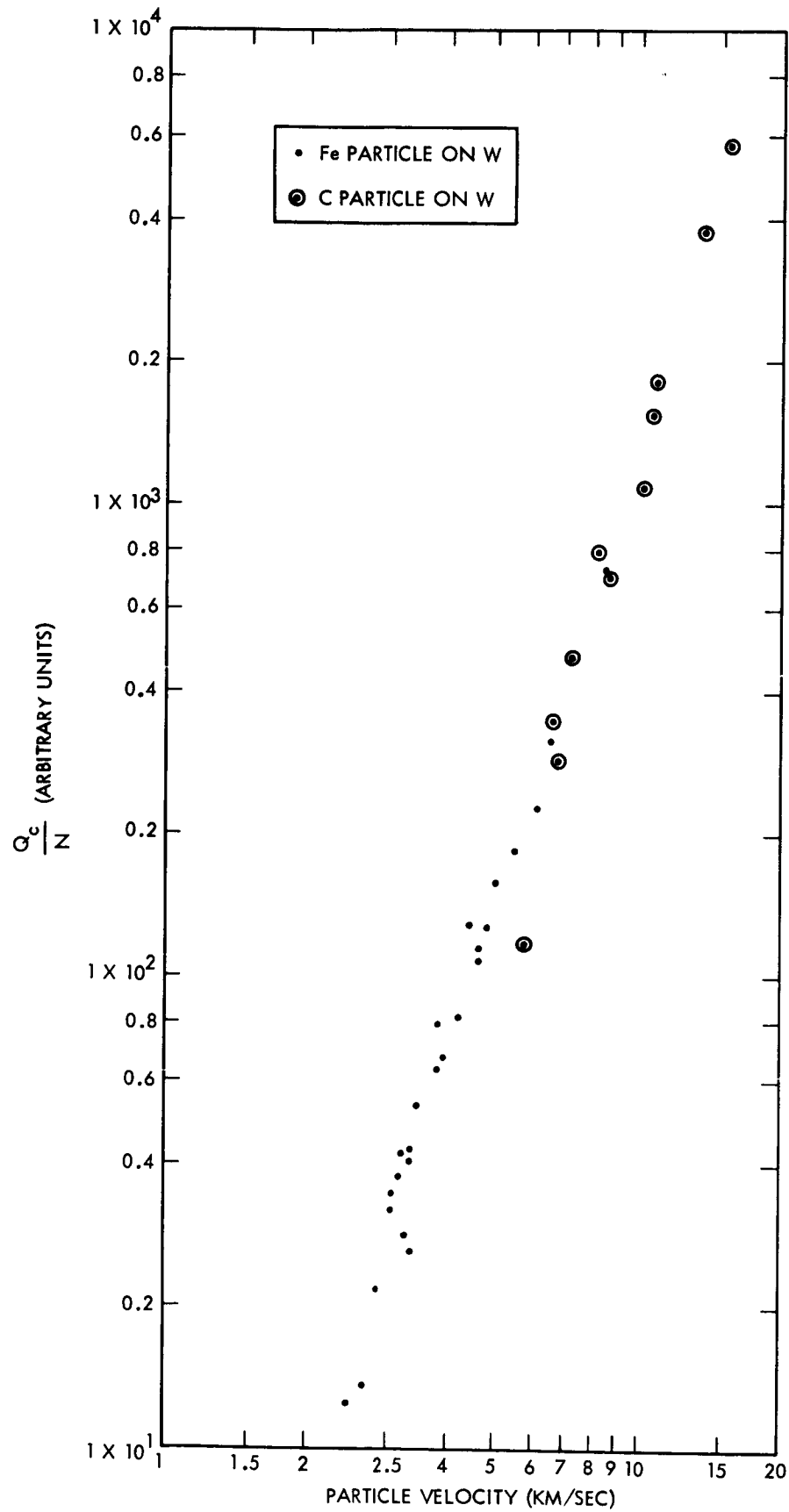


Fig. 4. Normalized Charge Emitted as a Function of Velocity for Iron and Carbon Particle Impacts on a Thick Tungsten Target.

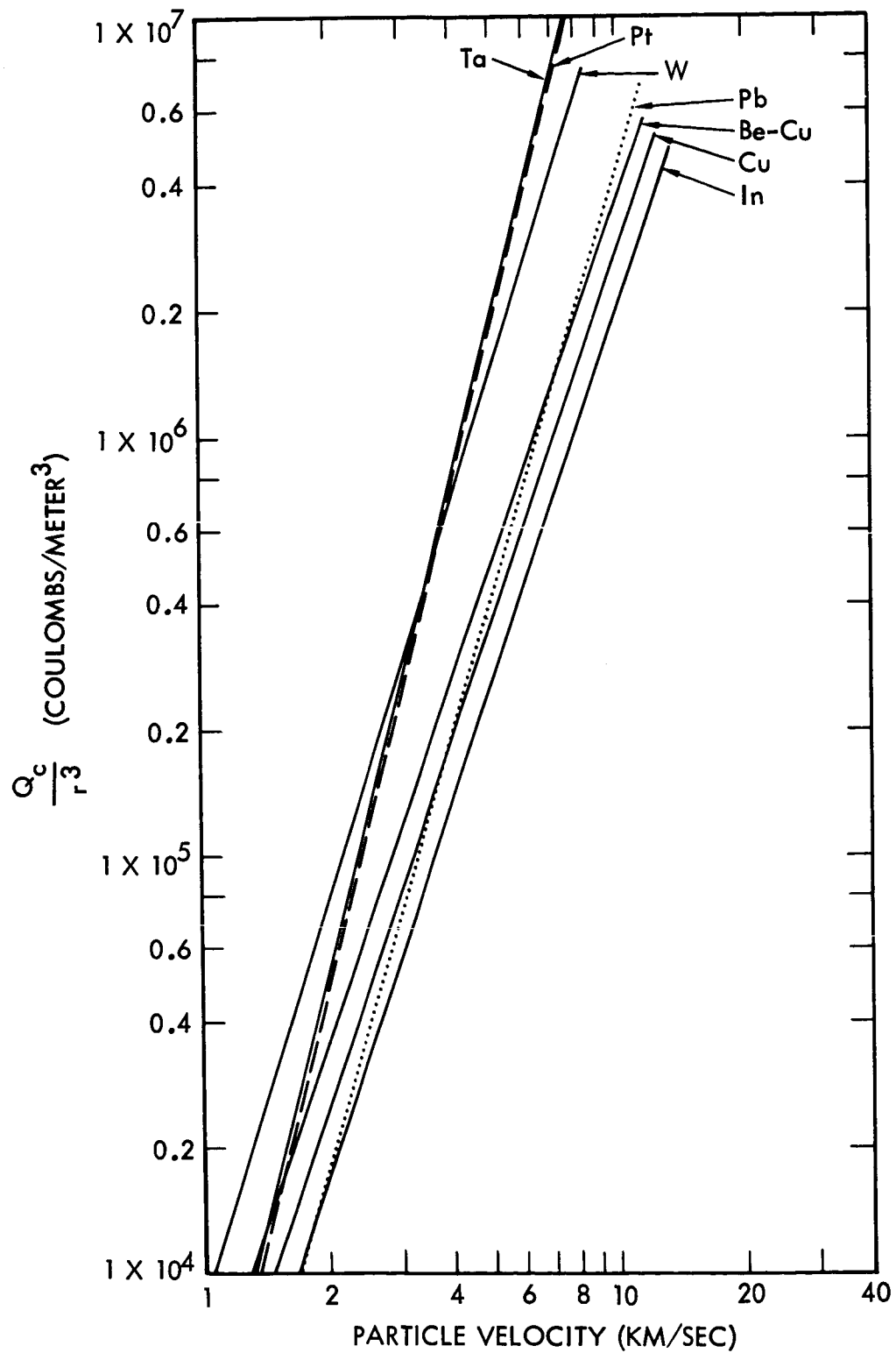


Fig. 5. Normalized Charge Emitted as a Function of Velocity for Iron Particle Impacts on Several Targets.

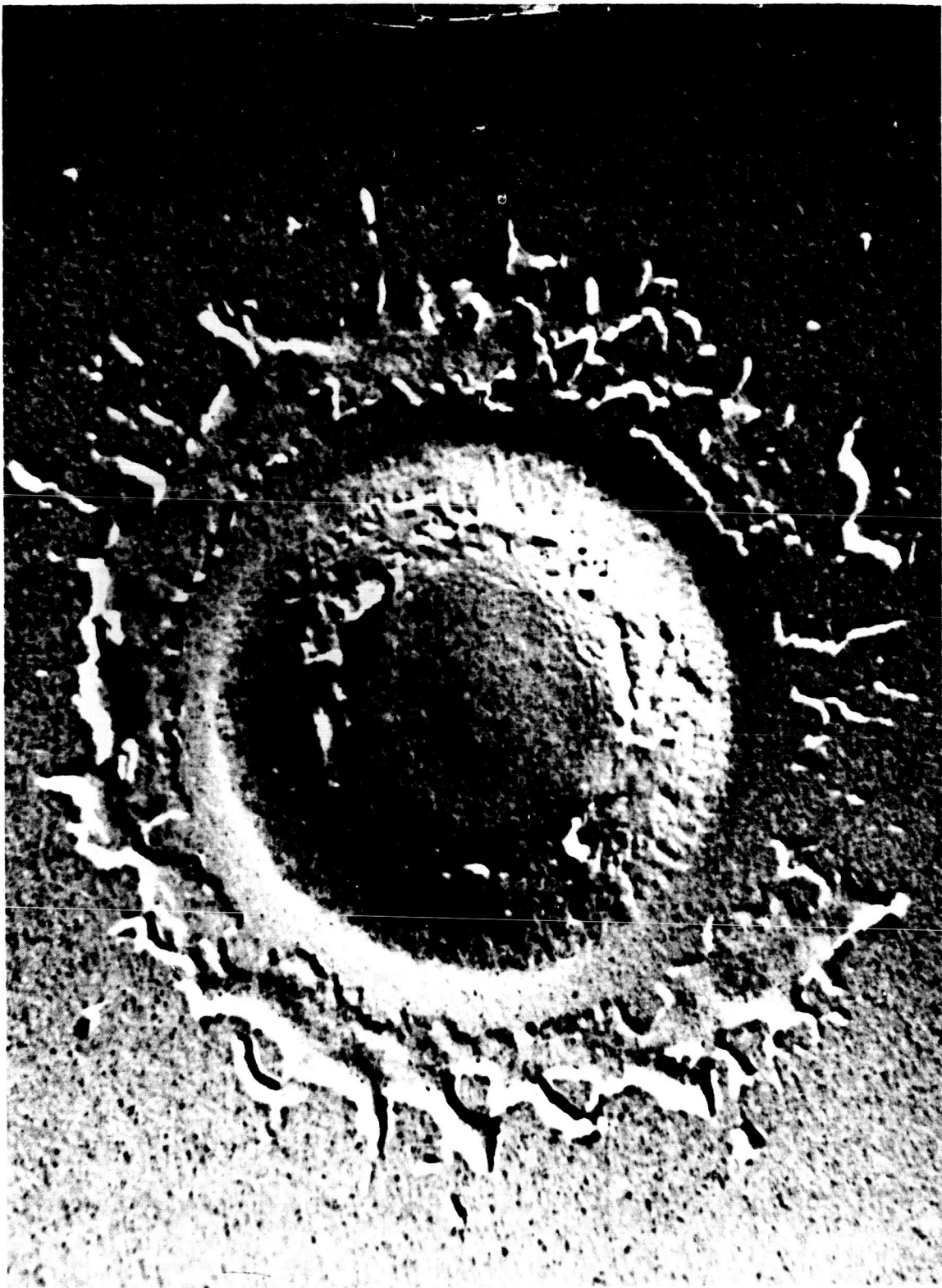


Fig. 6. Electron Micrograph of a Crater in
an Aluminized Glass Target.

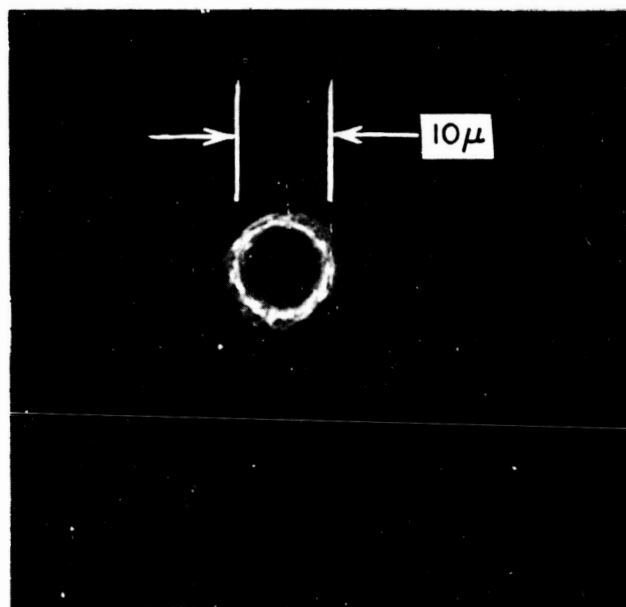
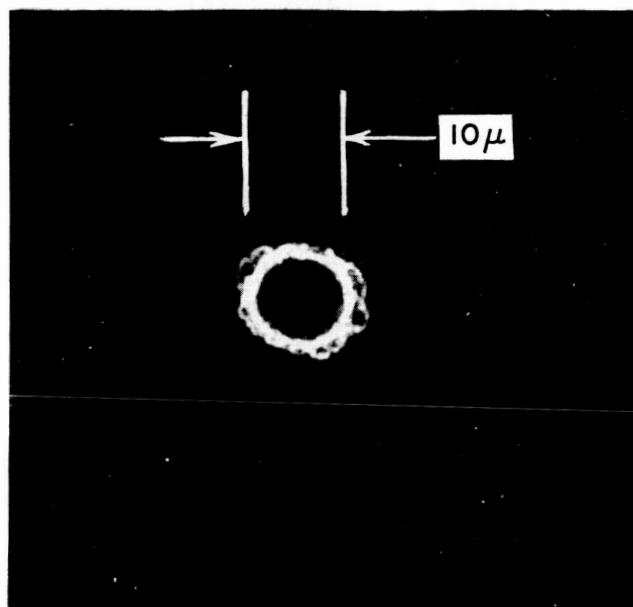


Fig. 7. Typical Micrographs of Craters in Lead Targets.

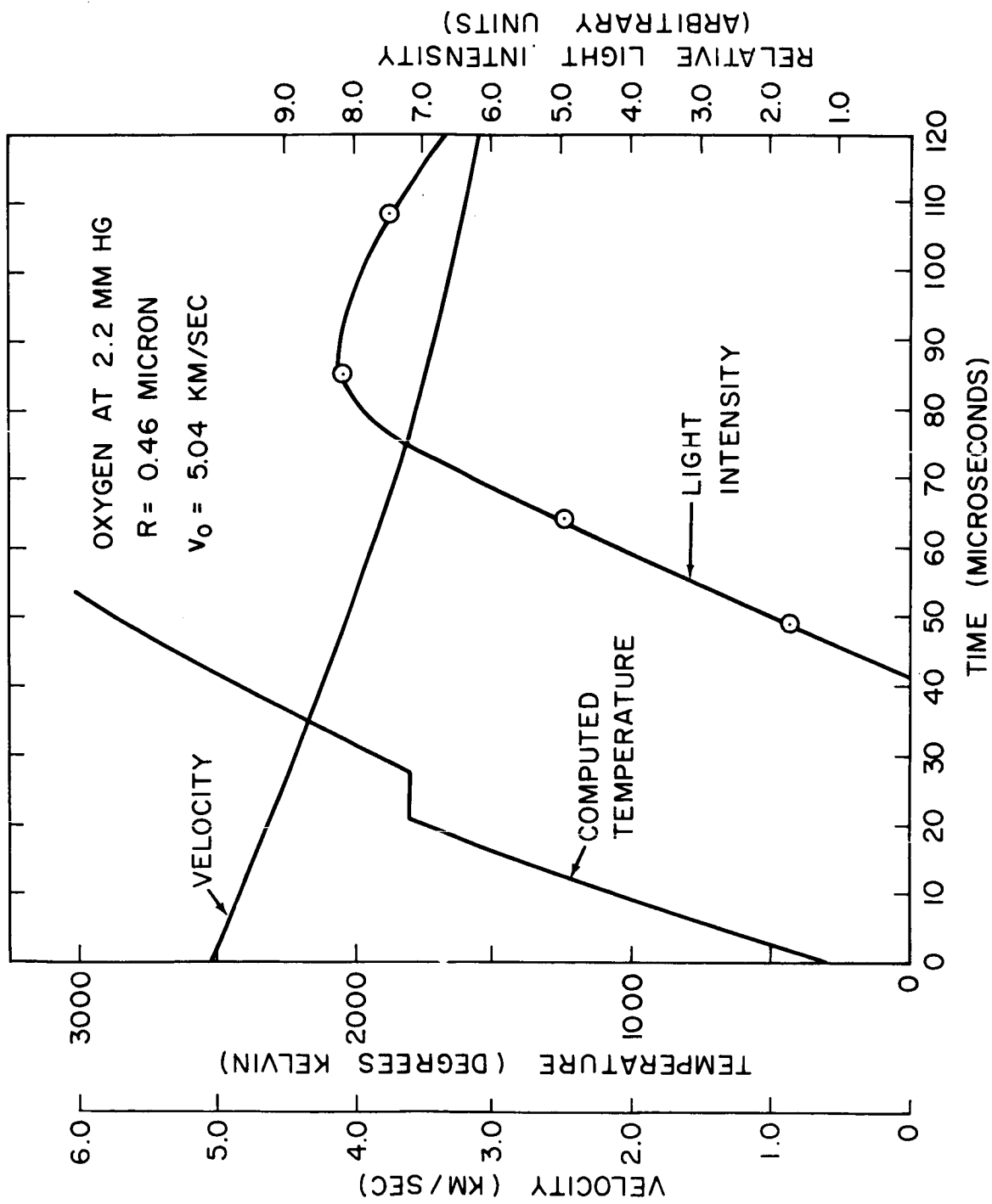


Fig. 8. Curves Illustrating the Simulation of Meteors.

IONIZATION ASSOCIATED WITH HYPERVELOCITY IMPACT

APPENDIX I

14 March 1963

"IONIZATION ASSOCIATED WITH HYPERVELOCITY IMPACT"

by

J. F. Friichtenicht and J. C. Slattery

Prepared for:

**National Aeronautics and Space Administration
Washington D.C.**

Contract No. NASw-561

**PHYSICAL ELECTRONICS LABORATORY
Physical Research Division**

**Space Technology Laboratories, Inc.
a Subsidiary of Thompson Ramo Wooldridge, Inc.
One Space Park, Redondo Beach, California**

IONIZATION ASSOCIATED WITH HYPERVELOCITY IMPACT

ABSTRACT

Interest in the development of micrometeoroid detection systems has led to a program of research at Space Technology Laboratories, Inc., where efforts have been concentrated on phenomena associated with hypervelocity impact which have properties applicable to such systems. It has been found that electrically charged particles are emitted from the site of a hypervelocity impact. Presumably, the large energy release associated with the impact is sufficient to produce ionization and the ions or electrons can be extracted by means of electrical collector systems. The quantity of charge emitted from semi-infinite targets as a function of target material, projectile material, and particle velocity and mass was measured. The experiments were conducted with micron-sized iron and carbon black (graphite) particles from the STL electrostatic hypervelocity accelerator. Data were collected for velocities up to 16 km/sec. All of the data fits the empirical relationship $Q_c = K E_p \frac{v}{A}$, where Q_c is the charge collected, K a constant, E_p the particle energy, A the atomic weight of the particle material, and v the particle velocity. The quantity K contains target material parameters and has not been evaluated, as yet. Qualitative observations of ionization produced from thin foil impacts have also been made.

IONIZATION ASSOCIATED WITH HYPERVELOCITY IMPACT

I. INTRODUCTION

An increasingly large effort has been devoted towards the direct measurement of small bodies in space in recent years. The properties of meteoroids and cosmic dust particles are interesting from both the engineering and scientific points of view, and it appears that experiments pertaining to these particles will be continued for some time to come. The experimental techniques for determining the quantity and properties of particles in interplanetary space by means of instruments aboard satellites and rocket probes and the results of some of the measurements are discussed briefly in a recent paper.¹ Although all of the data are in reasonably good agreement, it is evident that additional, more refined experiments, are required. One of the difficulties encountered in this type of experiment is the development of sensitive, reliable particle sensors.

Generally speaking, the encounter between an earth satellite and a meteoroid in space takes the form of a hypervelocity impact with the meteoroid serving as the projectile and the sensor as the target. The impact velocity may range from nearly zero up to 85 km/sec depending upon the relative orbits of the satellite and the meteoroid. The size range of the particles is also extremely large, although the frequency of occurrence increases with decreasing size. The smallest of them may be only a micron or so in size. Thus, the problem of assessing the characteristics of interplanetary dust can be described as the remote analysis of a hypervelocity impact of a projectile of unknown mass, velocity, composition, and direction, and whose velocity may be such that

¹W. M. Alexander, C. W. McCracken, L. Secretan, and O. E. Berg, "Review of Direct Measurements on Interplanetary Dust from Satellites and Probes", oral paper presented to the COSPAR Meeting, May, 1962.

the impact mechanism is not adequately understood. Considering these complexities, the good agreement of the existing data is all the more remarkable.

Most of the experiments have utilized a crystal transducer type sensor. The assumption is made that the magnitude of the electrical signal resulting from meteoritic impact is proportional to the momentum of the meteoroid. If an average velocity is assumed, the mass distribution of particles can be obtained from this instrument. It is clear from the nature of these assumptions that the development of more sophisticated sensor elements would be desirable. Consequently, Space Technology Laboratories, Inc., has been involved in a research program on those properties of hypervelocity impact which might serve as a basis for meteoroid detection systems. The program has been sponsored by the NASA, under Contract Nos. NASw-269 and NASw-561. One of the properties under study has been the emission of charged particles associated with hypervelocity impact.

We have concluded that some of the atoms near the impact site of a high speed particle are ionized by the large energy release associated with the impact. The emitted charge (either positive or negative) can be collected by means of electrically biased collectors and the resulting signal may be used in various types of meteoroid detectors. The quantity of charge emitted depends upon particle velocity and mass, and upon characteristics of the materials in question. An experimental study of this effect was undertaken and results of these experiments are described below.

II. GENERAL EXPERIMENTAL TECHNIQUES

The STL electrostatic hypervelocity projector was used as a source of high speed particles for all of the work described in the following paragraphs. The operation and properties of this

accelerator have been described in the literature² and need not be discussed here.

The electrostatic method of accelerating particles is generally restricted to particles with dimensions the order of microns or smaller. Carbonyl iron and carbon black (graphite) particles were used in these experiments. The iron particles were quite spherical while the carbon particles were somewhat more irregular in shape. The average size of the iron particles was about 1.5 microns diameter while the average carbon black particle had a corresponding dimension of about 0.6 micron. Particle velocities ranged from 1.5 to 16 km/sec depending upon particle material and size. The upper part of the velocity spectrum was obtained with the carbon particles while the iron particles were restricted to velocities of 10 km/sec and less. The velocity and mass of each particle were measured prior to impact by techniques described elsewhere.³ The size of the particles was then computed from the known mass and density. For the iron particles, the radius can be computed exactly. For the slightly irregular carbon particles we defined an effective radius, r , as the cube root of the quantity $\frac{3m}{4\pi\rho}$, where m is the mass and ρ the density.

For the experiments where the resulting signal was electrical in nature, the signal was displayed on one trace of a Tektronix Model 551 dual-beam oscilloscope while the signal from the particle velocity detector was displayed on the other trace. The signals were photographed with a Polaroid camera for later analysis. Time-of-flight techniques were used to correlate the observed event with the particle producing the event in order to eliminate spurious measurements.

²J. F. Friichtenicht, "Two-Million-Volt Electrostatic Accelerator for Hypervelocity Research", Rev. of Sci. Inst., Vol. 33, 209 (1962).

³H. Shelton, C. D. Hendricks, Jr. and R. F. Wuerker, "Electrostatic Acceleration of Microparticles to Hypervelocities", J. Appl. Phys., Vol. 31, 1243 (1960).

III. IMPACT IONIZATION FROM THICK TARGETS

A. Experimental Procedures

The geometrical configuration of the detector and collector system used in examining charge emission from thick targets is illustrated in Figure 1. Particles from the accelerator pass along the axis of a velocity-charge detector, pass through a grid structure, and impact upon the surface of the target sample at normal incidence. For all of the measurements discussed here, the target was biased 300 volts negative with respect to the grounded grid. With this bias, negative charge produced at the target surface is repelled from the collector while positive charge is retained. The quantity of charge retained by the target is determined from the relationship $q_c = C V$, where C is the electrical capacitance of the collector and V is the amplitude of the induced voltage signal. The RC time constant of the collector system was made long compared to the signal duration so that the signal is proportional to charge as opposed to current flow. We had previously determined that the quantity of collected charge was nearly independent of the polarity and magnitude of the bias voltage for biases exceeding a few tens of volts. For this work, the choice of bias voltage and polarity was made arbitrarily and it is assumed that corresponding results would be obtained with different choices.

Figure 2 is a tracing of a typical photographic record of an event. In this case, a copper target sample was used. The particle detector signal is displayed on the lower trace while the collector charge signal appears on the upper trace. Since the impacting particle is charged, a voltage signal is induced on the collector independently of that produced by subsequent charge emission. This effect accounts for the structure on the upper trace. The particle charge produces the first step in the signal

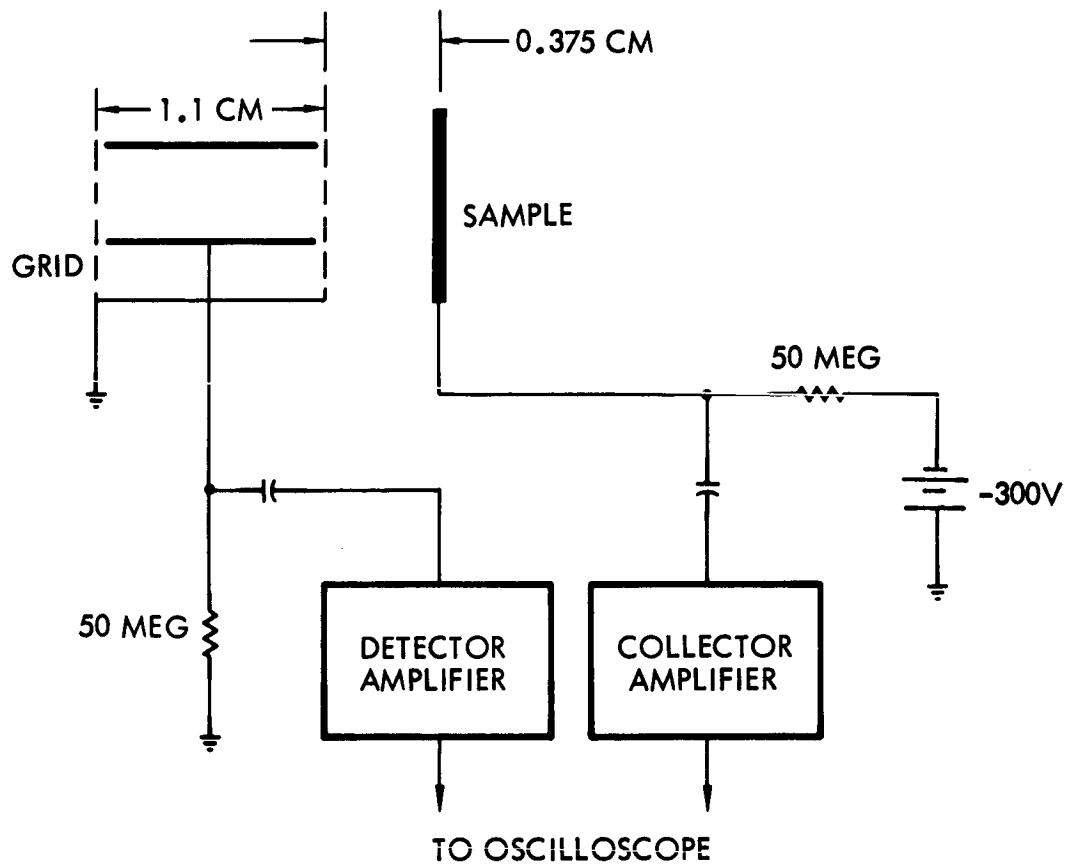


Figure 1. Experimental arrangement for the measurement of impact ionization from thick target impacts.

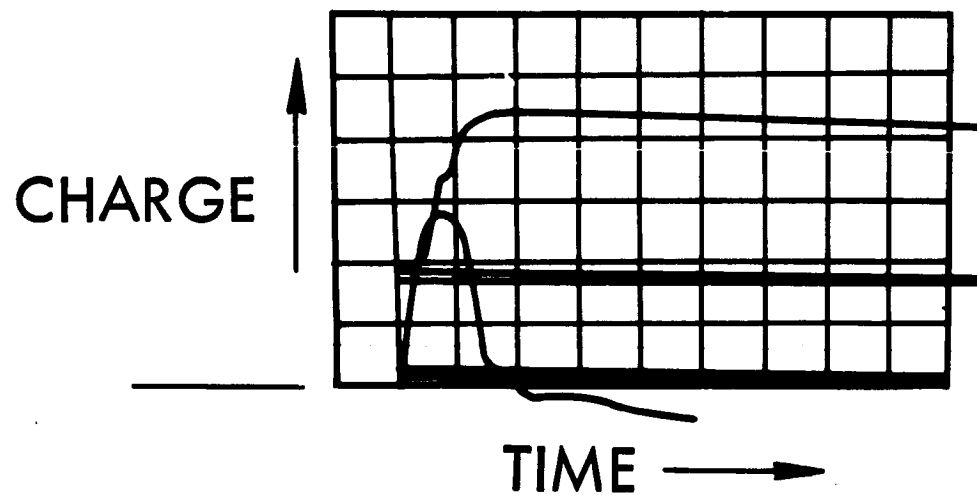


Figure 2. Tracing of an oscillograph obtained from the thick target measurements

while the charge emission effect accounts for the remainder. The total charge emitted is obtained by subtracting the particle charge from the total signal. In cases where the signal from the particle charge was small compared to the total, the particle charge was determined from the particle detector.

B. Velocity Dependence of Impact Charge Emission

Since few theoretical guidelines were available to assist us in interpretation of the experiments, the data were compared on a more or less empirical basis*.

For the purposes of discussion, assume that the amount of charge liberated upon impact is proportional to the kinetic energy of the particle. Further, assume that the energy term is modified by a velocity dependent function which takes into account threshold effects and variations of cratering mechanisms with velocity, i.e., $Q_c \propto E_p f(v)$. This is equivalent to

$$\frac{Q_c}{m} = K_1 v^2 f(v) \quad (1)$$

where m is the particle mass and K_1 is a constant of proportionality.

To evaluate $f(v)$, the quantity, Q_c/r^3 , (which is equivalent to Q_c/m for a given particle material) was plotted as a function of particle velocity for all of the particle-target combinations used. Figures 3 and 4 show these plots for iron particles impinging on targets of tantalum and indium respectively, while Figure 5 shows data for carbon particles on a tungsten target. Generally speaking, these data exhibit little scatter and the

*The format of the succeeding sections is primarily chronological in nature. The data are presented in this way to illustrate the evolution of the final result.

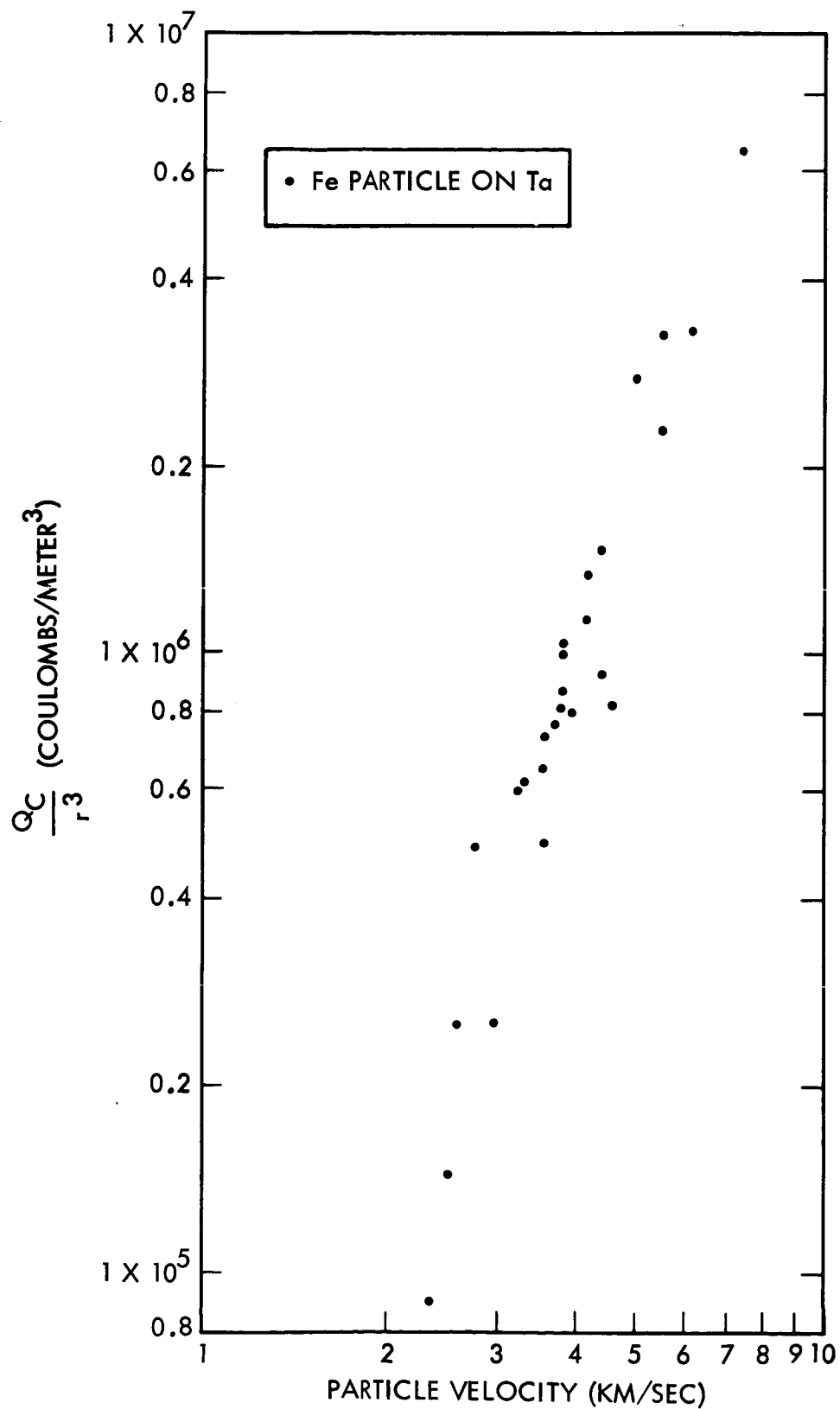


Figure 3. Charge collected normalized to r^3 plotted as a function of particle velocity for iron particle impacts on a thick tantalum target.

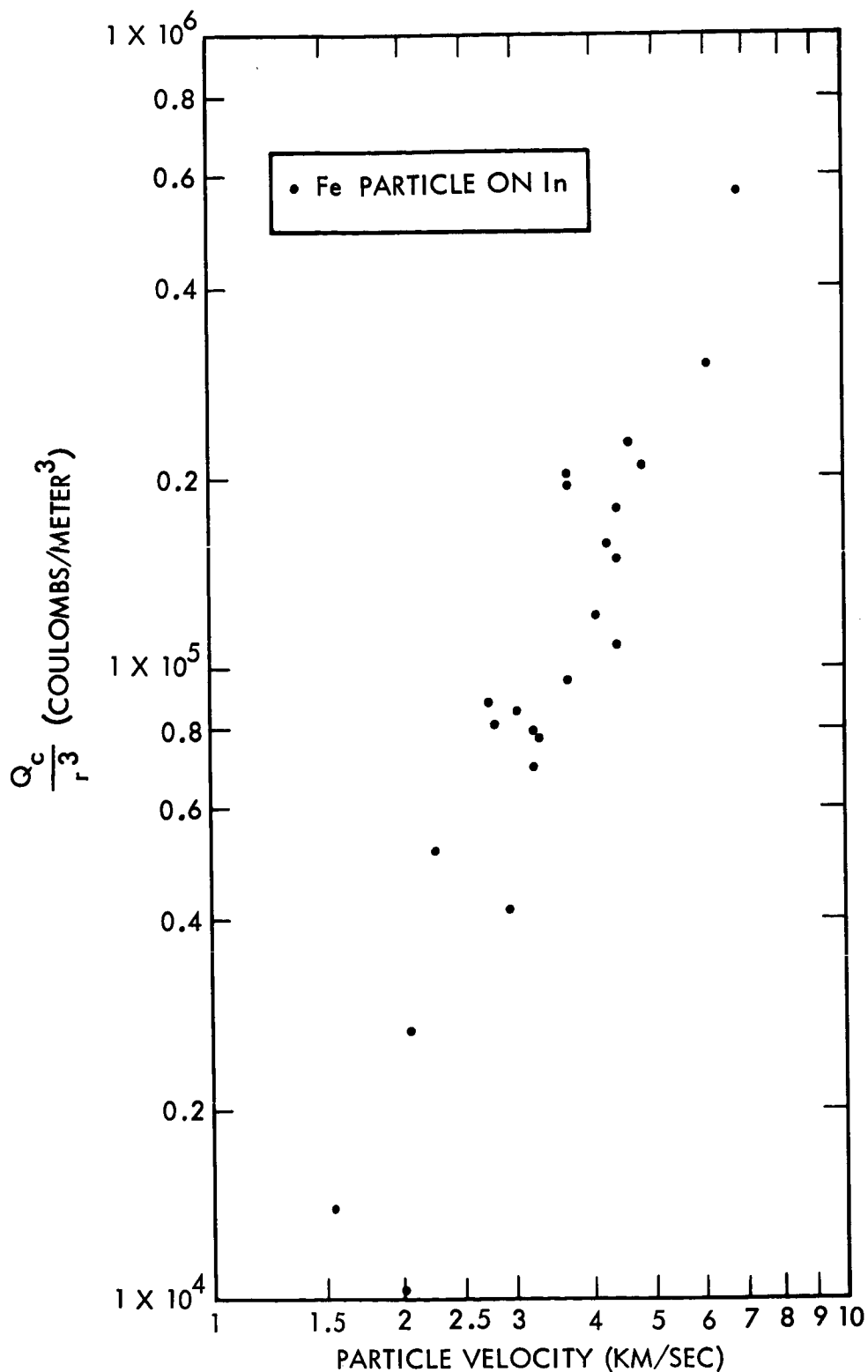


Figure 4. Charge collected normalized to r^3 plotted as a function of particle velocity for iron particle impacts on a thick indium target.

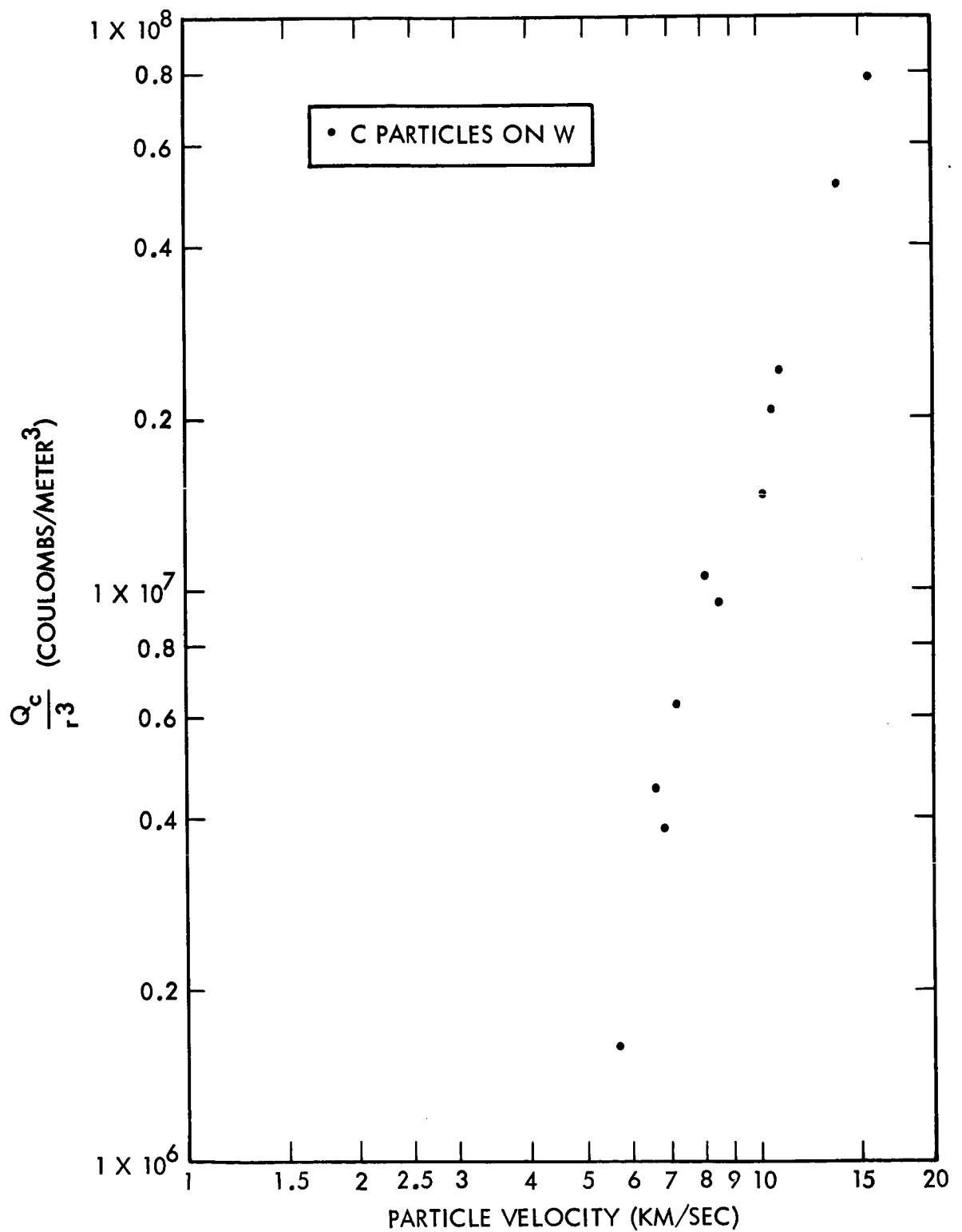


Figure 5. Charge collected normalized to r^3 plotted as a function of particle velocity for carbon particle impacts on a thick tungsten target.

data points tend to lie along straight lines on the logarithmic presentation. The slope of the lines, drawn by eye through the data points, is about three for all of the material and particle combinations used. This implies that $f(v) \approx v$. Consequently, we can write

$$Q_c = K_1 m v^3 \quad (2)$$

It should be emphasized that this is an empirical relationship and is valid only for the conditions described above. It can readily be seen, for example, that the expression is invalid for massive particles at very low velocities since charge emission does not occur under those circumstances. Yet, Equation (2) predicts a charge emission proportional to m .

C. Target Material Dependence

For a given particle mass and impact velocity, the quantity of charge emitted is dependent upon the target material. This is illustrated in Figure 6 where smoothed curves are plotted for each of the target materials. These data were obtained with iron particles. It can be seen that the materials examined fall into two distinct categories. More charge is emitted from the Ta, W, and Pt targets than from targets of Cu, Be-Cu, In, and Pb. With the possible exception of lead, all of the targets exhibit identical results.

It is almost certain that the quantity of charge emitted is a function of more than one characteristic of the target material. Because of the complexity of the problem, no attempt has been made to explain the material dependence. However, certain characteristics of the materials exhibit a similar grouping. For example, Ta, W, and Pt all have higher melting and vaporization temperatures than the others. Also these same materials are

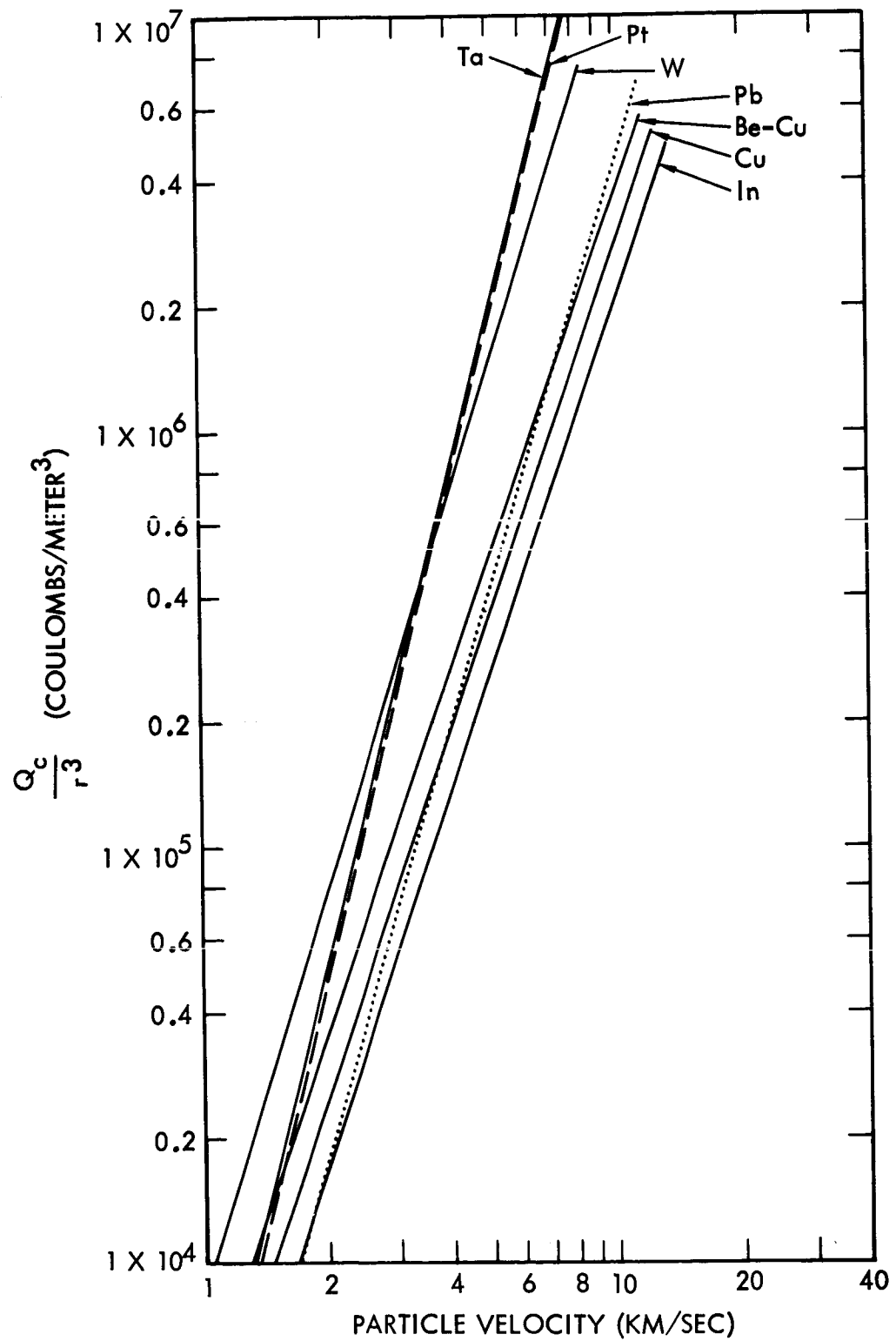


Figure 6. Q/r^3 vs. v for iron particle impacts on several target materials.

classified as good thermionic emitters while the others are not. Perhaps the most significant property of all (based on the discussion of the next section) is that of resistance to hypervelocity penetration. The craters produced in Pb, In, Cu, and Be-Cu, are generally larger than those in Ta, Pt, and W.

D. Particle Material Dependence

As mentioned earlier, both iron and carbon particles were used in these experiments. The relationship given by Equation (2) appears to fit the experimental results for both kinds of particles separately, but does not yield consistent results for both kinds of particles impacting on identical targets. When normalized to particle mass, the amount of charge produced by carbon particles was greater than that produced by iron particles at a given impact velocity. In order to explain this difference, one must invoke a mechanism for the charge production process. Initially, the assumption was made that the charge produced at the impact site was strongly dependent upon the energy per unit mass imparted to the target material. The quantity of charge collected would depend upon the extraction mechanism. For example, the charge could be dependent upon either the surface area or the volume of the emitting material. Application of several combinations of hypervelocity penetration formulae and assumed extraction mechanisms failed to provide the desired agreement. All of these hypotheses assume that the bulk of charge results from ionization of atoms of the target material. Failure to achieve correlation in this manner led to the development of the model discussed below.

Let us assume that most of the charge results from ionization of atoms of the impacting particle. The number of atoms ionized depends upon the number available, the energy required for ionization, and the energy available for ionization. The

kinetic energy of the particle is dissipated in several ways and the relative amount available for ionization is impossible to predict on the basis of existing knowledge on hypervelocity impact. Therefore, let us again adopt the empirical approach. Rather than normalizing the charge to the particle mass, let us normalize it to the number of atoms in the particle. This quantity, Q_c/N is plotted as a function of velocity for iron and carbon particle impacts on a tungsten target in Figure 7 and for a lead target in Figure 8. Since N is proportional to m , the same v^3 dependence is obtained. However, the agreement between the results of using iron and carbon particles is much better in this case. Normalization to the number of atoms is equivalent to the following expression:

$$Q_c = K_2 \frac{N_0}{A} m v^3 \quad (3)$$

where N_0 is Avogadro's number, A the molecular weight of the particle atoms, and K_2 a constant of proportionality. Equation (3) can be rewritten in the form

$$Q_c = K E_p \frac{v}{A} . \quad (4)$$

From this we see that Q_c depends upon the kinetic energy of the particle and upon a quantity which can be interpreted as a factor which determines the fractional part of the energy which is available for ionization. The role of the target in this interpretation is simply that of resisting penetration by the particle. The higher the resistance, the larger is the fraction of energy which goes into ionization.

The problem resulting from empirical data analysis is that one has difficulty in attaching physical significance to the

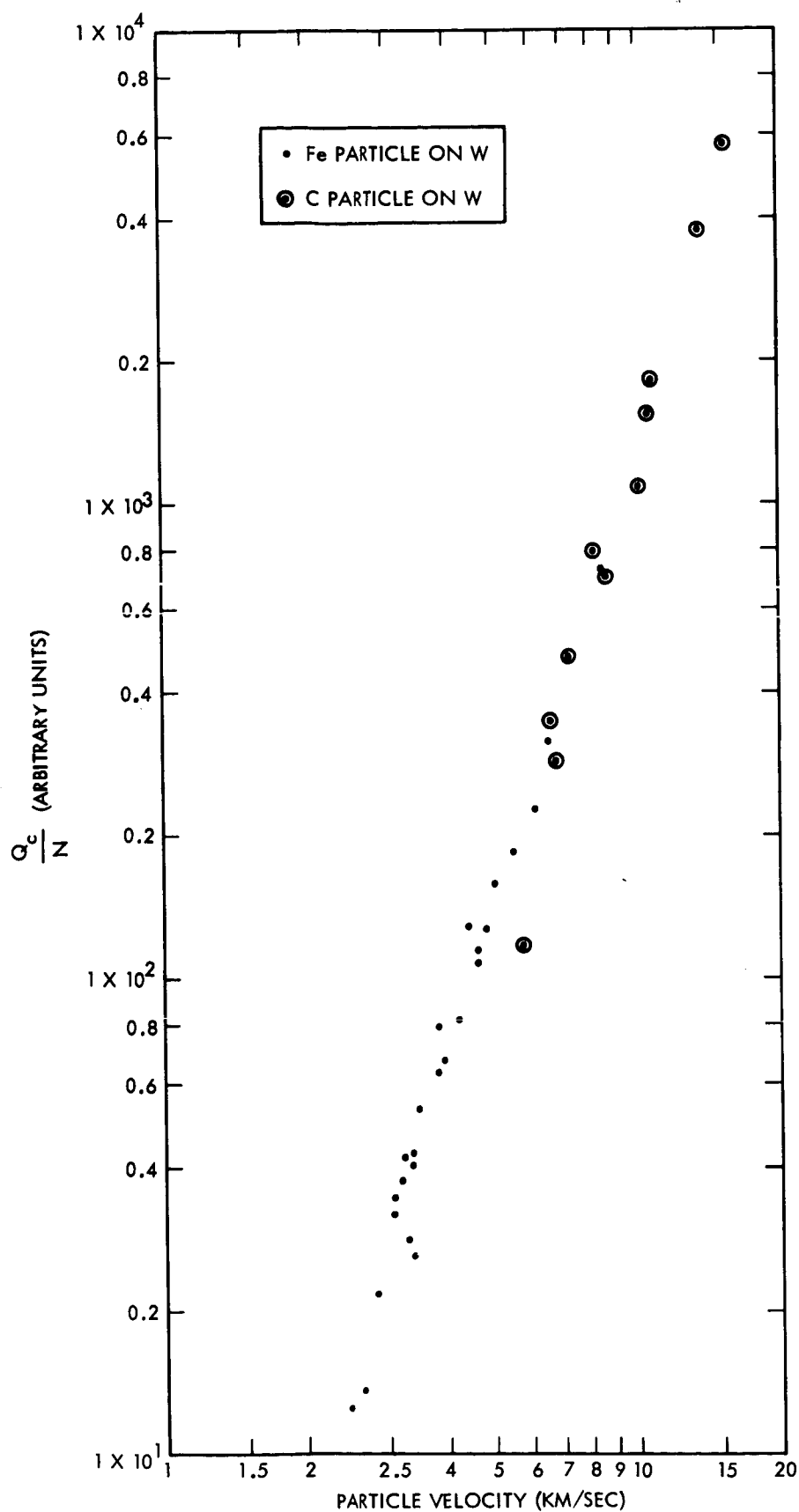


Figure 7. Charge collected normalized to the number of atoms in the particle as a function of velocity for carbon and iron particle impacts on a tungsten target.

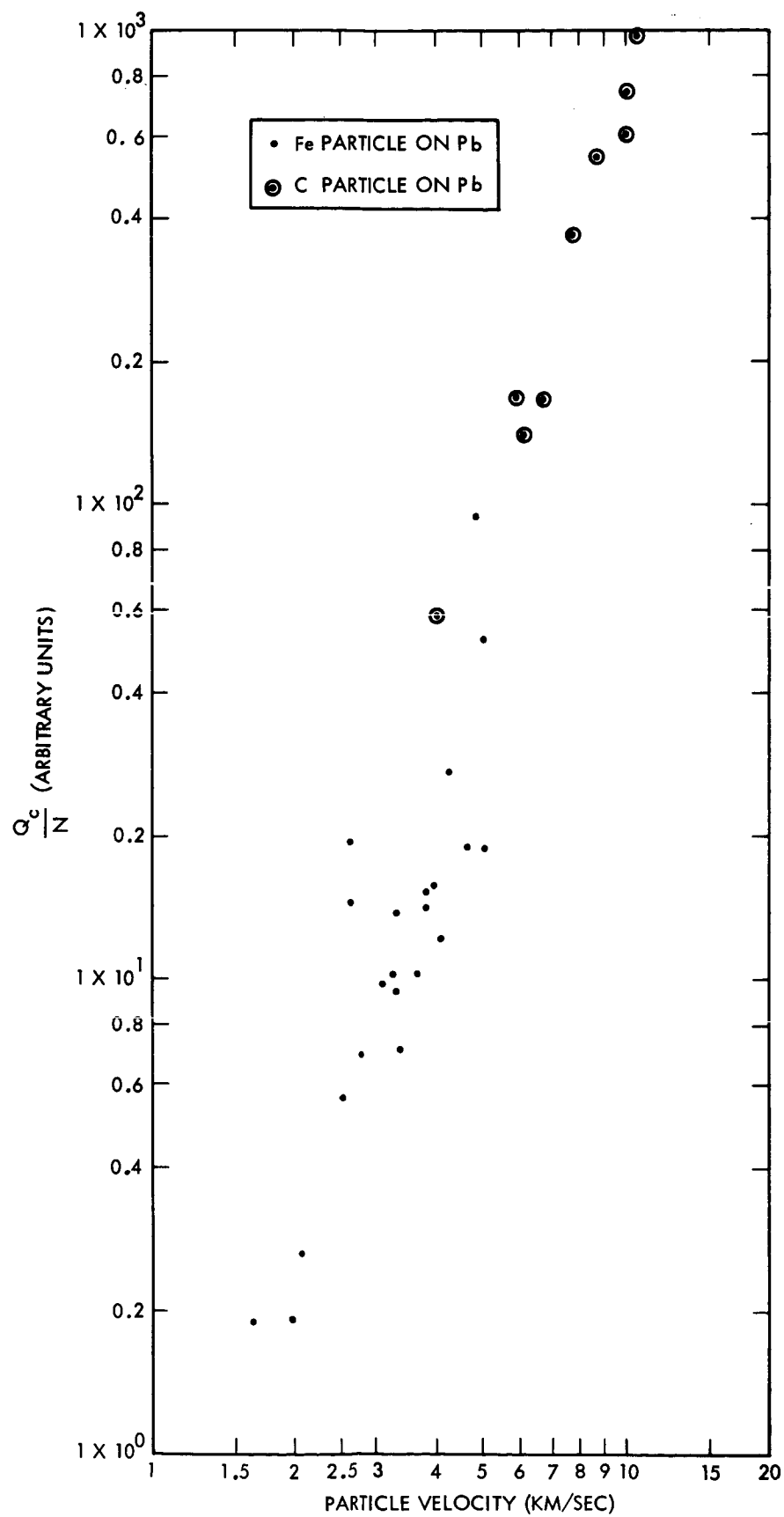


Figure 8. Charge collected normalized to the number of atoms in the particle as a function of velocity for carbon and iron particle impacts on a lead target.

results. The choice of $\frac{V}{A}$ as a multiplying factor is strictly empirical and we cannot justify it from a physical point of view. Despite these drawbacks, one must have a framework within which to work and the approach used in the preceding section provides such a framework. Additional experiments should be helpful in developing physical concepts to describe the charge emission phenomenon.

IV. IMPACT IONIZATION FROM THIN TARGETS

Ionization produced by particle impacts on thin foils has also been the subject of experimental investigation. The observations have been more qualitative in nature than thick target measurements because of the increased complexity. A brief discussion of the more interesting observations is given in the following paragraphs.

We have found that electrical charge is produced by a high speed particle impact on a thin foil. The charge can be collected by means of various types of electrically biased collectors placed on the "downstream" side of the foil. Generally, we find that the charge collected is greater in magnitude than would be predicted on the basis of thick target measurements. One possible explanation of the the results (suggested by O. E. Berg from NASA) is that "spray" particles from the foil interact with the surface of collectors. Each spray particle would produce charge upon impact in a manner analogous to that described in Section III.

Since the velocity and size distribution of spray particles is dependent upon the nature of the impact, qualitative analysis is difficult. The nature of the impact depends upon particle velocity and the thickness of the foil relative to the size of the particle. We have observed at least three types of impacts, namely: (1) those where the energy loss is small and the particle passes through the foil intact; (2) those where particle break-up

occurs; and (3) those where the particle appears to be completely vaporized. A recently developed technique has enabled us to photograph these events. The foil is placed in the high pressure region (pressure the order of a few mm Hg) of a differential pumping system. Debris from a high speed impact interacts with the gas leaving trails which can be photographed with the aid of a sensitive image intensifier tube. Typical photographs are shown in Figure 9. Figure 9-a shows a particle which passes through the foil with only a slight brightening of its trail. The fragmentation of a particle is illustrated in Figure 9-b. In this case, large discrete trails are left by the fragments. Complete vaporization of a particle is shown in Figure 9-c. These are unretouched photographs and the consistent pattern on the photographs is the result of a low-level image intensifier background which is repetitive from photograph to photograph.

V. SUMMARY

Preliminary experiments on the impact ionization effect have been described along with an empirical analysis of the results. Clearly, more definitive measurements are required to adequately assess the impact ionization effect. A continuing program of research may answer some of the questions raised by the results of experiments described above. The authors wish to express their appreciation to Mr. N. L. Roy for his invaluable assistance in the acquisition of the data described in this report.



a



b



c

Figure 9. Photographs of particle impacts on an 800 Å thick gold foil in a low pressure oxygen atmosphere.

IMPACT IONIZATION FROM FRAGILE TARGETS

APPENDIX J

TECHNICAL REPORT

"IMPACT IONIZATION FROM FRAGILE TARGETS"

July 1965

Prepared for

National Aeronautics and Space Administration
Washington, D. C. 20546

Contract No. NASw-936

J. F. Friichtenicht
Prepared by
J. F. Friichtenicht
Manager, Meteoritics Dept.

D. B. Langmuir
Approved by
D. B. Langmuir
Director

PHYSICAL ELECTRONICS LABORATORY
Physical Research Division

TRW Systems
One Space Park, Redondo Beach, California

IMPACT IONIZATION FROM FRAGILE TARGETS*

I. INTRODUCTION

The properties of hypervelocity impact on fragile or granular targets is of interest because of the similarity to meteoroid impact on the moon. There is considerable evidence to support the "dust layer" hypothesis for the lunar surface. The effects of meteoritic impact on the formation and moderation of such surfaces are not well understood. A number of experimenters, principally Gault, et al¹ from NASA Ames Research Center, have conducted cratering and penetration measurements on granular targets and have studied the properties and magnitudes of ejected material. This work was done using light gas gun techniques and was primarily concerned with simulation of meteoritic impact on the lunar surface.

It was first suggested by Maurice Dubin² of NASA Headquarters that the impact ionization effect and observations of high-speed impact in a low pressure gas environment might be valuable diagnostic tools for measurements of this type. The sections below describe the initial experiments done on the impact ionization effect using fragile targets.

II. EXPERIMENTAL PROCEDURES

Earlier work³ indicates that the rapid energy release associated with the impact of high-speed particles on metallic surfaces results in vaporization and ionization of material near the impact point. For a number of particle-target material combinations, it was found that the total charge produced upon impact Q fits the empirical relationship

$$Q = k mv^3 \quad (1)$$

* This work supported by the NASA under Contract NASw-936.

where m and v are the particle mass and velocity, respectively, and k is a constant depending upon the materials involved. For a given particle material, Q depends upon the target material. All of the materials tested fall into two distinct groups. At a given velocity, more charge is produced with tungsten, tantalum, and platinum targets than with targets of indium, copper, beryllium-copper, and lead. Our interpretation of these results was that the primary role of the target was resistance to penetration which limits the energy release to a smaller volume.

The objective of the present experiment is to study the effect of target structure on the amount of ionization produced upon impact by a high velocity particle. The measurements were conducted in much the same manner as described in Ref. 3. The TRW Systems electrostatic hypervelocity accelerator⁴ was used for all of the measurements. After passing through detectors for measurement of particle velocity and mass (see Ref. 4), the particles impacted on the target surface at normal incidence. A grounded grid is placed in front of the target. For this experiment, the target was biased 300 volts negative with respect to the grounded grid. The target to grid spacing was about 3 mm yielding an electric field at the target surface of 10^5 volts/meter. In this arrangement, free electrons created at the target surface are repelled while the positive ions are retained, thus producing a positive signal. The signal is amplified by a high input impedance amplifier and displayed on a dual beam oscilloscope along with the detector signal. The decay time constant of the input stage of the preamplifier is such that the amplitude of the output signal is proportional to total charge detected. The portion of the signal due to the particle charge was subtracted to yield the net charge created by the impact.

Two types of targets were used; one was a solid target of Armco iron while the other was a target made up of carbonyl iron spheres identical to those used in the accelerator. The targets are presumed to be similar except in structure, i.e., the iron

spheres were very loosely bound. The particulate target was formed by milling a recess in a slightly magnetized holder. Particles were placed in the recess and smoothed as much as possible with a knife blade. The retaining power of the magnet was sufficient to hold the particles in place even when the target was in a vertical position. To ensure that target geometry was reproduced, a small disk of Armco iron was machined to fit the recess for use as the solid target.

III. EXPERIMENTAL RESULTS

The results of the experiment are illustrated graphically in Fig. 1 where the net charge produced Q is normalized to particle mass and plotted as a function of velocity for both types of targets. The points represent the data acquired with the solid target while the crosses represent the particulate target data. Within the scatter exhibited by the data points, there appears to be no marked difference in the impact ionization produced between the two types of targets at high velocities. Both sets of points follow the v^3 dependence which has been noted before. At lower velocities (~ 6 km/sec and smaller), less charge is produced by impact on the particulate target. In fact, about 10 data points, which are not shown on the graph, were below the limit of detectability. This is probably understandable, because at low velocities the strength of the target enters into most aspects of hypervelocity impact. Since the target composed of particles is so weak, most of the particle kinetic energy is probably absorbed by competing mechanisms.

The particulate target was examined with an optical microscope following particle bombardment. Although no quantitative measurements were made, it was evident that much larger craters were formed in the particle target than in the solid iron target. Further measurements on both the impact ionization effect and cratering in weak targets are required in order to fully assess the applicability of such experiments to simulated lunar bombardment. In particular, the possibility of obtaining weak targets with more precise properties should be explored. The effect of grain size should be evaluated, also.

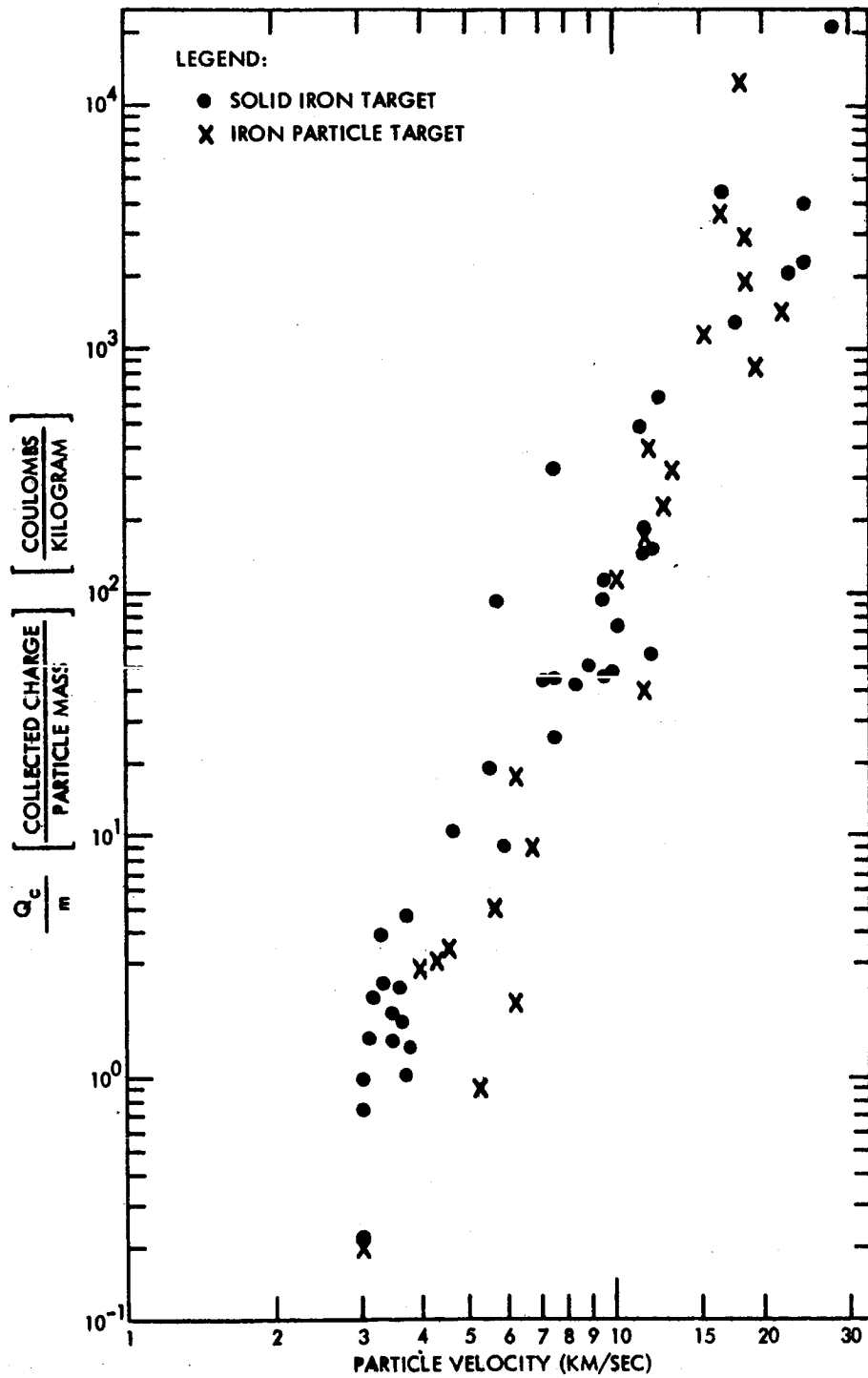


Fig. 1. Normalized Impact Charge Production as a Function of Particle Velocity for Solid and Particulate Iron Targets.

REFERENCES

1. Gault, Shoemaker, and Moore, "Spray Ejected from the Lunar Surface by Meteoroid Impact", NASA Technical Note D-1767, 1963.
2. Maurice Dubin, Private Communication.
3. J. F. Friichtenicht and J. C. Slattery, "Ionization Associated with Hypervelocity Impact", NASA Technical Note D-2091, August 1963.
4. J. F. Friichtenicht, "Two-Million-Volt Electrostatic Accelerator for Hypervelocity Research", Rev. of Sci. Instr., Vol. 33, 209-212, 1962.

**EXPERIMENTS ON THE IMPACT-LIGHT-FLASH
AT HIGH VELOCITIES**

APPENDIX K

TECHNICAL REPORT

"EXPERIMENTS ON THE IMPACT-LIGHT-FLASH
AT HIGH VELOCITIES"

July 1965

Prepared for

National Aeronautics and Space Administration
Washington, D. C. 20546
Contract No. NASw-936

J. F. Friichtenicht
Prepared by
J. F. Friichtenicht
Manager, Meteoritics Dept.

Bernard Hamermesh (for)
Approved by
D. B. Langmuir
Director

PHYSICAL ELECTRONICS LABORATORY
Physical Research Division
TRW Systems
One Space Park, Redondo Beach, California

EXPERIMENTS ON THE IMPACT-LIGHT-FLASH AT HIGH VELOCITIES

I. INTRODUCTION

One of the observable phenomena associated with hyper-velocity impact is the so-called impact light flash produced by the conversion of some fraction of the projectile kinetic energy to radiant energy. The light flash provides a mechanism for the observation of high-speed impact phenomena. In addition, it has been used as a meteoroid counter in micrometeoroid detector systems,¹ and it is hoped that some property of the impact flash may be used in such systems to determine meteoroid mass and velocity. In this context Rosen and Scully² have suggested that photometric measurements of the impact flash at two different wavelengths may provide the desired information.

Traditionally, the depth of penetration and the size of craters formed have been the most significant engineering parameters of high-velocity impact, and by far the bulk of experimental and theoretical work has been concerned with these aspects of high-speed impact. The effects of melting and vaporization have only recently been considered in hypervelocity penetration theory.³ Some properties of the vapor cloud can be observed directly by photographic techniques,⁴ while others may be inferred from indirect measurements such as those of ionization processes.⁵ The existence of ionization suggests that the vapor cloud may possess plasma-like characteristics, including self-luminosity due to the excitation of neutral gas atoms. Thus quantitative measurements of the properties of the impact light flash can provide information on vaporization effects.

In an early study⁶ of the impact light flash conducted with large projectiles from a light gas gun, line spectra arising from excitation of residual gas atoms in the target chamber appeared to account for most of the observed radiation. The more

recent experiments of Rosen and Scully (Ref. 2) were conducted in a vacuum of less than 10^{-2} mm Hg using small projectiles approximately 50 microns in diameter. Since the residual gas interactions were negligible, the observed radiation was attributed to blackbody emission from heated particles or droplets ejected from the target. On the basis of this assumption, they were able to correlate the peak flash intensity with the amount of material ejected from the target.

This report describes experiments on the impact light flash conducted with very small (approximately 1 micron) particles over the velocity range from about 2.5 km/sec up to nearly 40 km/sec. The results of measurements using unfiltered photomultiplier tubes suggested that the emission spectrum was similar to that of a blackbody radiator. Apparent blackbody temperatures were measured by two-color photometric techniques similar to those used by Rosen and Scully, and similar results were obtained over the range of velocities common to both experiments. However, a significant departure from the rate of increase of temperature with velocity predicted by Rosen and Scully was observed. Although no attempt has been made to determine the source of radiant energy, it appears likely that two sources exist: One is blackbody emission from heated material, the other radiation from excited atoms in the vapor cloud.

II. EXPERIMENTAL PROCEDURES

A. Particle Acceleration and Analysis

In all of the work discussed here the TRW Systems electrostatic hypervelocity accelerator⁷ was used. In this accelerator small particles are first charged electrically by a process described elsewhere⁸ and then injected into the accelerating electric field of a 2-million-volt Van de Graaff Generator. Here they are accelerated to a final velocity given by $v = (2qV/m)^{1/2}$, where V is the accelerating voltage, m is the mass of the particle,

and q is its charge. As described in Ref. 8, the q/m of a particle is proportional to the reciprocal of the particle radius. As a consequence of this relationship, the electrostatic method of accelerating particles is most effective for very small particles. Under optimum conditions, iron particles of 1 micron diameter reach a final velocity of about 7 km/sec. (Smaller particles, or particles composed of lower density materials, achieve correspondingly higher velocities. As examples, carbon particles have been accelerated to velocities in excess of 20 km/sec, and sub-micron iron particles have been accelerated to nearly 40 km/sec.) Carbonyl iron spheres (98% Fe) with a mean diameter of about 1.5 microns were used for all of the experiments described below.

The charge and velocity of each particle are determined after it has been accelerated but before it strikes the target surface. This is accomplished by measuring the magnitude and duration of the voltage signal induced by a particle as it passes through a cylindrical drift tube of known capacitance and length. The charge is given by $q = CV_i$, where V_i is the amplitude of the induced voltage pulse and C is the capacitance of the drift tube to ground. The velocity is simply $v = \ell/t$, where t is the transit time through a cylinder of length ℓ . The mass of the particle is found from $m = 2qV/v^2$.

Usually the signal from the detector is amplified and displayed on an oscilloscope trace, which is photographed for subsequent analysis. The signals from the photomultiplier tubes (PMT's) used to observe the light flash are also recorded photographically. When only a single PMT was used, its signal was displayed on one trace of a dual-beam oscilloscope while the detector signal was displayed on the other. When several tubes were in use simultaneously, each signal was displayed on a separate oscilloscope trace. All of the oscilloscopes were triggered from a common source (either the detector signal itself or the output signal from the velocity selector system described below) to ensure time correlation of the observed signals.

Most of the high-velocity data (i.e., above about 10 km/sec) were obtained with the aid of a recently developed velocity-selection system. The carbonyl iron particle source is characterized by a wide distribution of particle sizes (with diameters from about 0.1 to 3.0 microns). As a consequence of the charging process, the smaller and less frequently occurring particles achieve the highest velocities. Since the very high velocity particles appear so rarely, direct photography of each particle signal is not a very satisfactory way of acquiring high-velocity data. To alleviate this problem, the velocity-selection system is used to produce a trigger pulse whenever a particle within a predetermined velocity interval appears. This is accomplished by means of two particle-detection stations and a simple logic circuit. The signal from the first detector opens a narrow gate at some predetermined delay time. The signal from the second detector is fed to the gate; if the gate is open, a trigger pulse is generated but if the signal arrives at any other time no signal is generated. Both the delay time and the width of the gate pulse are adjustable. In practice, the trigger pulse is used to trigger the sweep circuits of the oscilloscopes, which display the signals from a third particle detector and the PMT's. The particle velocity and mass are determined by analysis of the signal from the third detector.

B. Impact-Flash Measurement Techniques

For the single-PMT measurements of the impact flash from glass targets, particles from the accelerator passed through a particle detector and then struck a glass target whose surface was normal to the direction of the particle beam. The target, which was in the form of a disc, also served as a vacuum window. The PMT was optically coupled to the rear of the window with Dow-Corning 200 Fluid. In some cases, the front surface of the target-window was coated with an extremely thin but opaque film of aluminum. The purpose of the film was to shield the PMT from light emitted from the vapor cloud, thus limiting these measurements to the "body flash". Under these circumstances the signal

from the PMT appears as a large amplitude spike followed by a lower-level, exponentially decreasing signal. It is presumed that the spike represents the body flash. Experiments appear to bear this out, since the amplitude of the initial spike is essentially unaltered by the presence or absence of the aluminum film.

Most of the front-surface impact-flash measurements and all of the spectral measurements were made using the target chamber shown in Fig. 1. This chamber provides viewing ports for four PMT's, which view the surface of the target at an angle of 45° to the normal. Particles from the accelerator enter the chamber through the aperture between the phototubes and impact at the center of the target, the point of impact lying at the apex of the pyramid formed by the axes of the viewing ports. The viewing ports are sealed by thin Lucite windows. The PMT's are held against the viewing ports by an aluminum structure that also has a recess for standard 2 x 2 inch optical filters. The internal surfaces of the chamber are polished to increase light-gathering efficiency, and all optical joints are made with a thin layer of silicon grease to reduce light losses at the interfaces.

RCA 6199 photomultiplier tubes with S-11 spectral response were used for all of the measurements. Standard PMT circuitry was used, with the photocathode at about 1000 volts negative and the anode grounded through the load resistor. A high-impedance voltage divider supplied the correct operating voltage to the dynodes. The last few stages were backed up by capacitors to avoid nonlinearities arising from large signal levels. The frequency response was adjusted by varying the anode capacitance to ground. The output signals were fed to wide-bandpass cathode-followers and from there directly to the oscilloscopes.

Although the PMT's were not calibrated against a standard blackbody radiation source, a certain amount of care was taken in determining the over-all response. The most critical factors affecting over-all response are the spectral response of the PMT-

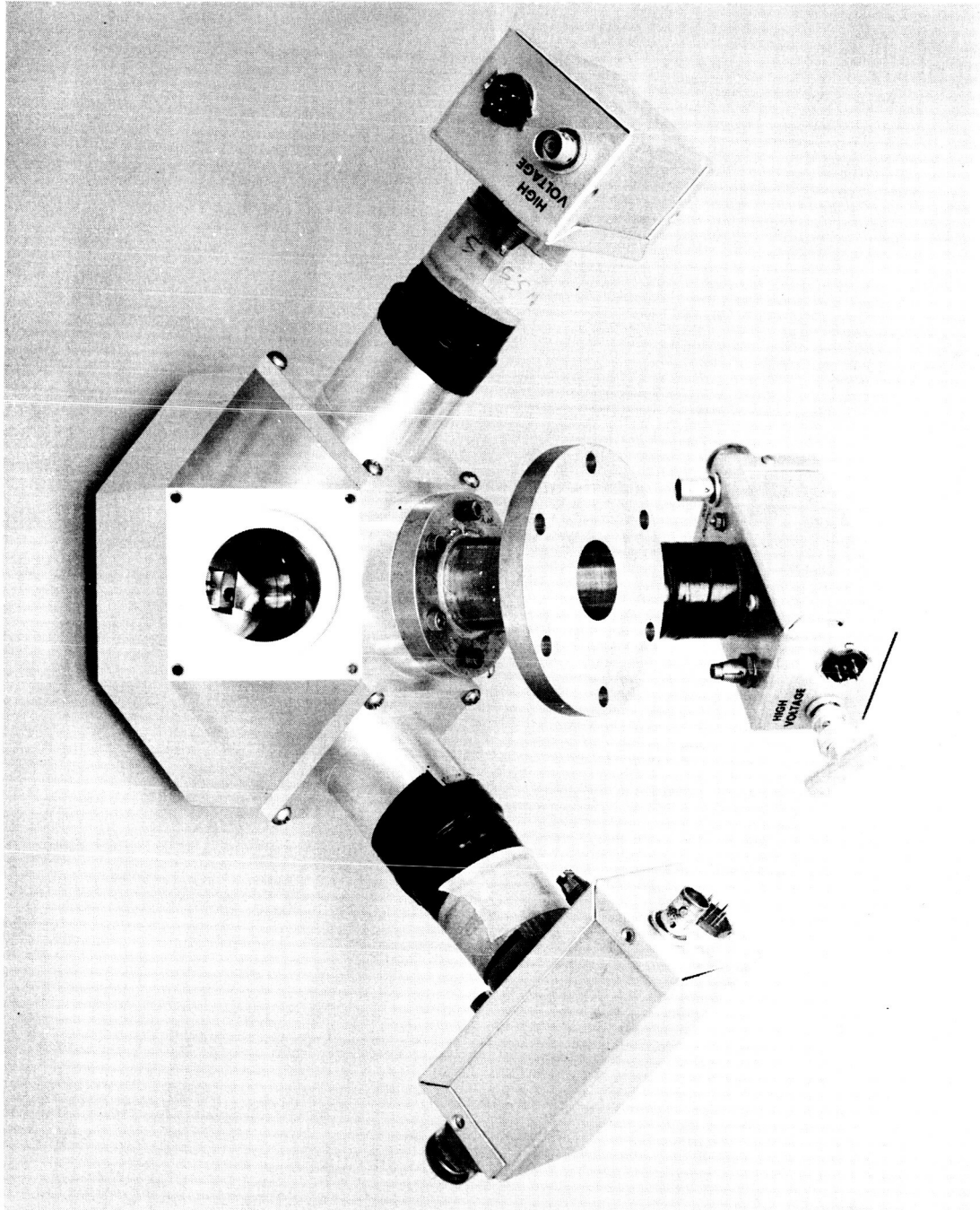


Figure 1. Impact Light Flash Target Chamber Assembly.

filter combination and the gain of the electron-multiplier assembly.

The spectral response characteristics of the PMT-filter combinations were determined from the S-11 spectral characteristics curve published by the manufacturer and from the transmission characteristics of the filters (also supplied by the manufacturer). The spectral response of two filtered PMT's that were used as a pair for the photometric measurements are shown in Fig. 2. Another pair of filtered PMT's with a similar, but slightly different spectral response was also used, but they are not illustrated. For purposes of analysis, it was assumed that the area under a particular curve represents the sensitivity to radiant energy at the peak wavelength.

To determine the gain of the electron-multiplier assemblies, the gains of the tubes that comprised a pair for the temperature measurements were adjusted to a common value. A pulsed neon light served as the calibrating source, and the gain was set by a potentiometer which adjusted the total voltage across the dynode chain. To account for possible variations in the light source intensity, each tube was checked several times. In practice, all four PMT's were fed from a single high-voltage power supply. Since electron multiplication is a strong function of voltage, the supply voltage was monitored continuously by a digital voltmeter and maintained at a value constant to about one part in a thousand. Under these conditions, the variation in electron gain was probably no greater than 1 or 2%.

C. Two-Color Temperature Measurements

In the experiments, the actual property measured is the intensity of light emission at two different wavelengths. To convert these measured values to the apparent temperature, the experimental data are used with the Planck blackbody radiation law, namely,

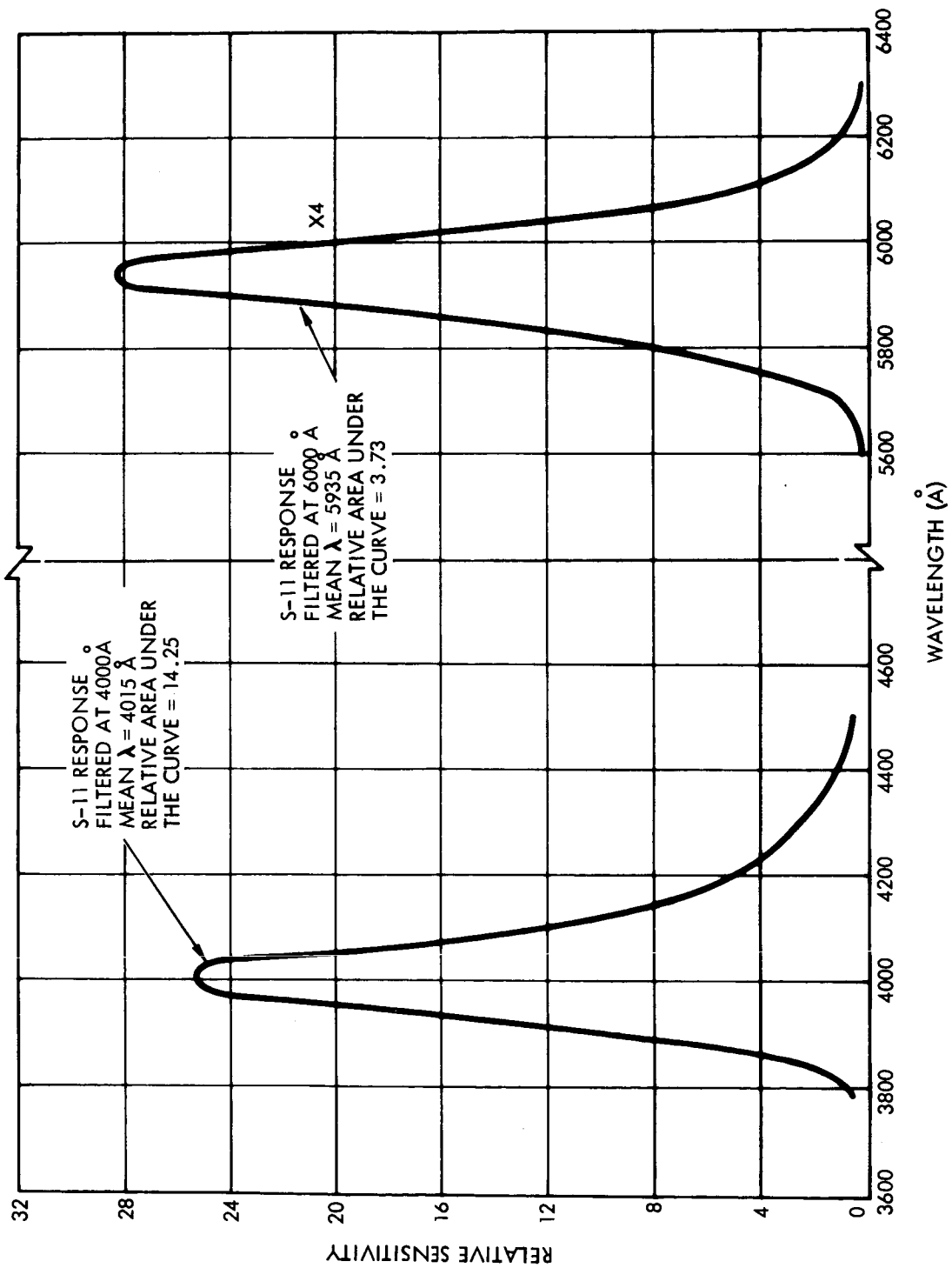


Figure 2. Spectral Response Characteristics of Two Filtered RCA 6199 Photomultiplier Tubes used as a Pair in the Two-Color Photometric Measurements.

$$\Psi_{\lambda} = \frac{K_1}{\lambda^5} \frac{1}{e^{\frac{(K_2/\lambda T)}{-1}}}, \quad (1)$$

where Ψ_{λ} is the intensity at wavelength λ , T is the temperature of the radiator, and K_1 and K_2 are constants. The magnitude of the output signal from a PMT sensitive only at wavelength λ is given by

$$I_{\lambda} = S_{\lambda} \Psi_{\lambda}, \quad (2)$$

where S_{λ} is the radiant sensitivity. The ratio of the light intensity at two different wavelengths i and j defines the temperature uniquely, as given by

$$\frac{I_i}{I_j} = \frac{S_i}{S_j} \left(\frac{j}{i} \right)^5 \frac{e^{\frac{(K_2/jT)}{-1}}}{e^{\frac{(K_2/iT)}{-1}}} \quad (3)$$

In the present case S_{λ} is proportional to the area under the appropriate spectral response curve. The curve for converting from measured signal level ratios to apparent blackbody temperature, as calculated from Eq. (3), is given in Fig. 3 for the spectral response characteristics indicated in Fig. 2.

III. EXPERIMENTAL RESULTS AND DISCUSSION

A. Single-Phototube Observations

As mentioned in the previous section, the body flash in glass targets is characterized by an intense, short-duration flash followed by a lower-intensity emission that decays with a relatively long time constant. The duration of the initial spike

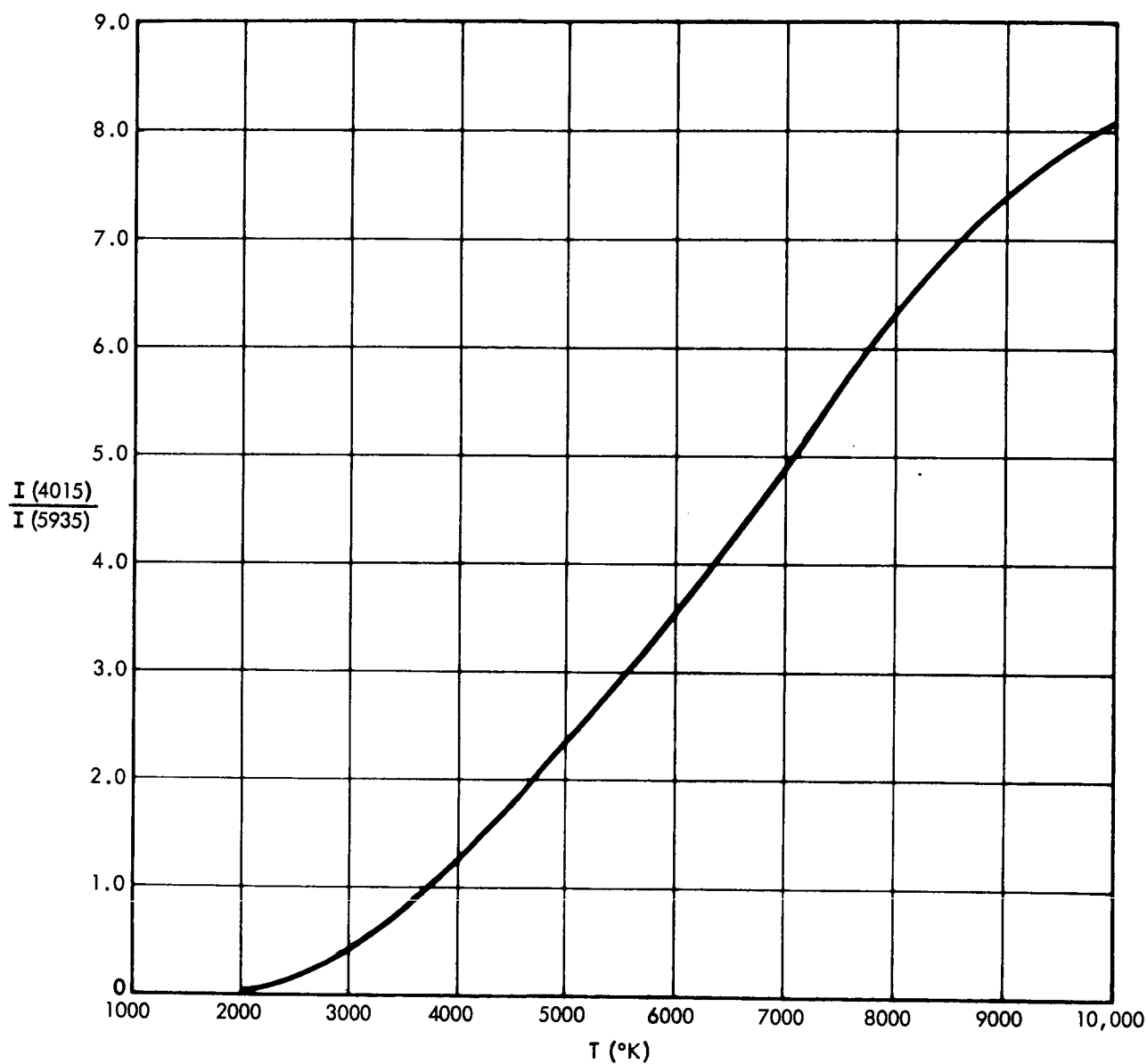


Figure 3. Calibration Curve for Conversion from Intensity Ratios to Apparent Blackbody Temperature. This curve applies to the PMT-filter combinations illustrated in Fig. 2.

is about $0.2 \mu\text{sec}$, while the low-intensity portion of the emission persists for as long as $10 \mu\text{sec}$. For most measurements, the PMT signal was integrated electronically to facilitate the procedures. Thus in the results obtained, the magnitude of the signal is proportional to the total radiant energy emitted but is dominated by the high-intensity portion. Typical results are illustrated in Fig. 4, where the peak light-flash amplitude divided by the mass of the particle is plotted as a function of particle velocity. Normalizing to particle mass has the effect of presenting the data as if the particles were of a uniform mass, and is based on the assumption that the magnitude of the light flash is directly proportional to particle mass.

Data for impacts on a solid tantalum target are shown in Fig. 5. In this case, of course, the impact flash was observed from the front face of the target. Again, the output signal was electronically integrated. The signal waveform observed in this manner is somewhat different in that the initial spike that is characteristic of the body flash is not nearly so prominent as that obtained with glass targets. In fact, it is questionable that it appears at all. Generally, the signal rises to peak value in about 50 nanosec and then decays exponentially with a time constant of about $5 \mu\text{sec}$. Because of the integration, the signal amplitude is proportional to the total radiant energy within the spectral range of the PMT.

Over the limited velocity range covered by these data points, the body flash from glass targets, as represented in Fig. 4, is more strongly velocity dependent than is the flash observed from a solid metallic target. Straight-line "eye" fits to the points imply that on glass targets the body flash increases as about the seventh power of velocity, while in the other case the slope is only about three. As can be inferred from results discussed later, this difference is not attributable to the differences in target materials and hence, must be indicative of the difference between the body flash viewed from the rear of the target and

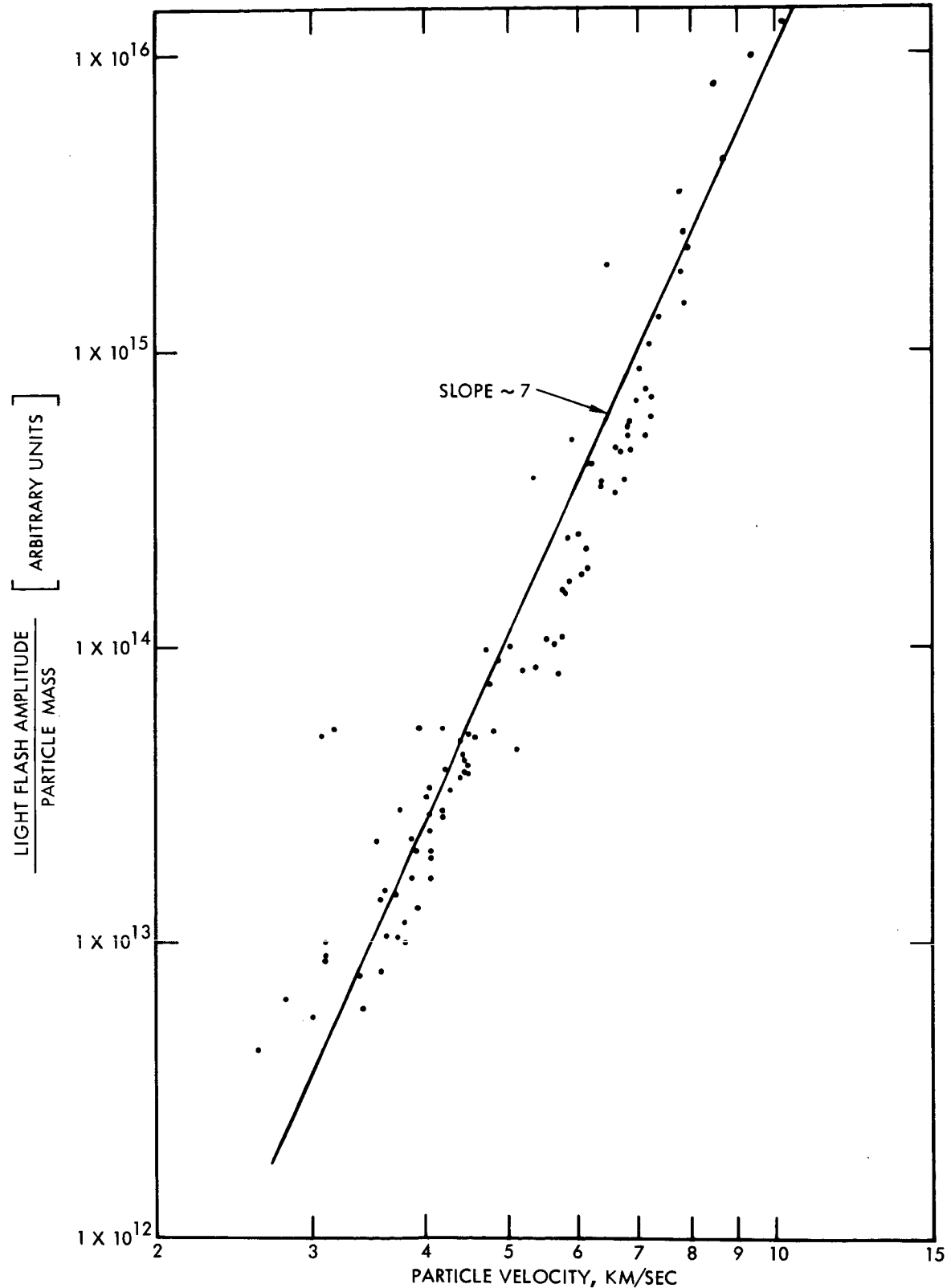


Figure 4. Light Flash Intensity over the Visible Range Normalized to Particle Mass as a Function of Impact Velocity for a Glass Target. An RCA 6199 Photomultiplier with S-11 response was used.

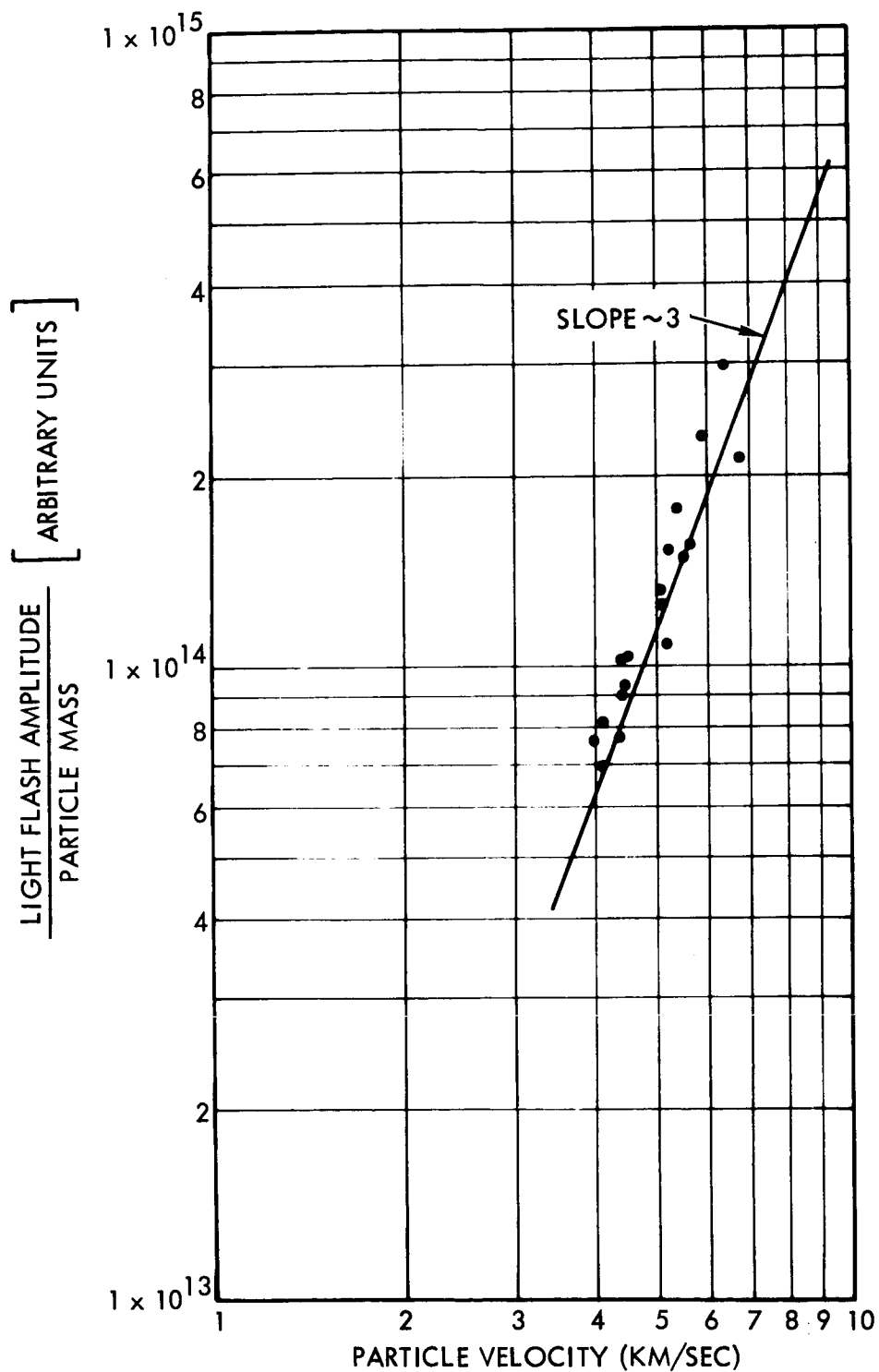


Figure 5. Normalized Light Flash Intensity as a Function of Particle Velocity obtained with a Tantalum Target and an unfiltered RCA 6199 Photomultiplier Tube.

radiation viewed from in front of the target.

B. Spectral Measurements

Two-color photometric measurements were conducted to determine apparent blackbody temperature as a function of particle impact velocity on tantalum and fused-quartz (Vycor glass) targets. The term "apparent" means that the temperature was determined on the assumption that the source of light is an ideal blackbody radiator, although there is no direct evidence to support this assumption.

Two separate temperature determinations were made for each target material. The only difference between the two test arrangements (aside from very slight differences in the spectral response of the filters used) was the output circuitry of the PMT's. For one pair of tubes the output signals were integrated by shunting the 100 K Ω anode resistors with 100 pf capacitors, giving an RC decay time of 10 μ sec. In the other case, no capacitors were added and the effective RC decay times were less than 1 μ sec. In the first case, the net effect of the integration is that the total radiant energy from the flash is measured at some fixed wavelength; in the second, the signal is more nearly proportional to the instantaneous radiant intensity at the wavelength specified by the spectral response characteristics of the PMT's. Since the intensity is a strong function of temperature in the range under study, the response in either case is dominated by radiation from the flash while it is at high temperature, and the peak amplitudes of the signals are representative of the maximum temperature.

In principle, the cooling of the flash could be monitored by measuring the ratio of the appropriate signals as a function of time. However, it was found that the signals decay to the noise level so rapidly that measurements of this type did not appear feasible under the present circumstances.

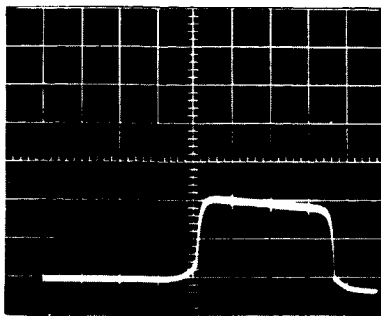
Generally speaking, the integrated signals provided the best-quality data, particularly at low signal levels. This

higher quality stems from the fact that the integration tends to minimize the effects of statistical fluctuations in the electron-multiplication process, which are sizable for small signals. However, measurements made with the non-integrating circuitry provide an internal check for consistency of the results.

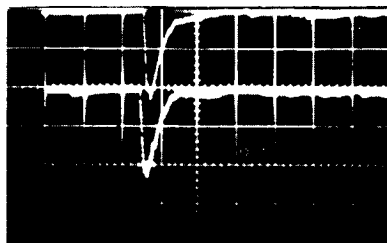
A set of oscillographs depicting the raw data obtained for an event under somewhat favorable conditions is shown in Fig. 6. The uppermost picture shows the detector signal, while the oscillograph in the center displays the integrated output signals at 5935 \AA and 4015 \AA (upper and lower traces, respectively). Similar traces for the PMT's with broadband external circuitry are shown in the lower photo, where the upper trace gives the intensity at 5885 \AA and the lower gives the intensity at 4050 \AA .

Ideally, one needs only to measure the ratio of the amplitudes of the pair of signals to determine the apparent temperature. A case where this was done is illustrated in Fig. 7. These data were obtained from the integrated intensity measurements on a tantalum target. Clearly, the results show a steadily increasing temperature with particle velocity. One gets the impression that the ratio of intensities is increasing more slowly at the high velocities, but the scatter in the data points prevents quantitative verification of this point. The results presented in Fig. 7 are not as satisfactory as those presented later since to obtain accurate data, high-quality signals must be obtained simultaneously from both PMT's, and this was not always the case. Often the signal from one of the two PMT's was either too large or too small to be measured accurately, and at the higher temperatures the blue-sensitive PMT produced larger and more easily measured signals, which apparently led to a high-temperature bias.

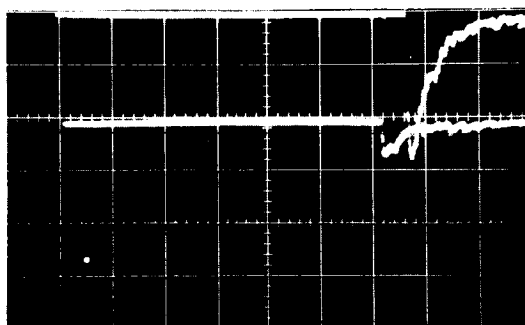
To alleviate this problem and to minimize the scatter exhibited by the points in Fig. 7, an averaging technique was employed. In this method the peak light-flash amplitude, normalized to particle mass, was plotted as a function of particle



6a



6b



6c

Figure 6. Oscillographs Illustrating the Response of the Various Sensors. The uppermost picture shows the signal from the particle velocity-charge detector. The photograph in the center shows the signals from the PMT's with integrating output characteristics. The upper trace in this picture was derived from a PMT sensitive at 5935 Å while the lower trace corresponds to the intensity at 4015 Å. Similar signals from the PMT's with broadband external circuitry are shown in the lower picture with the upper and lower traces giving the intensity at 5885 Å and 4050 Å respectively.

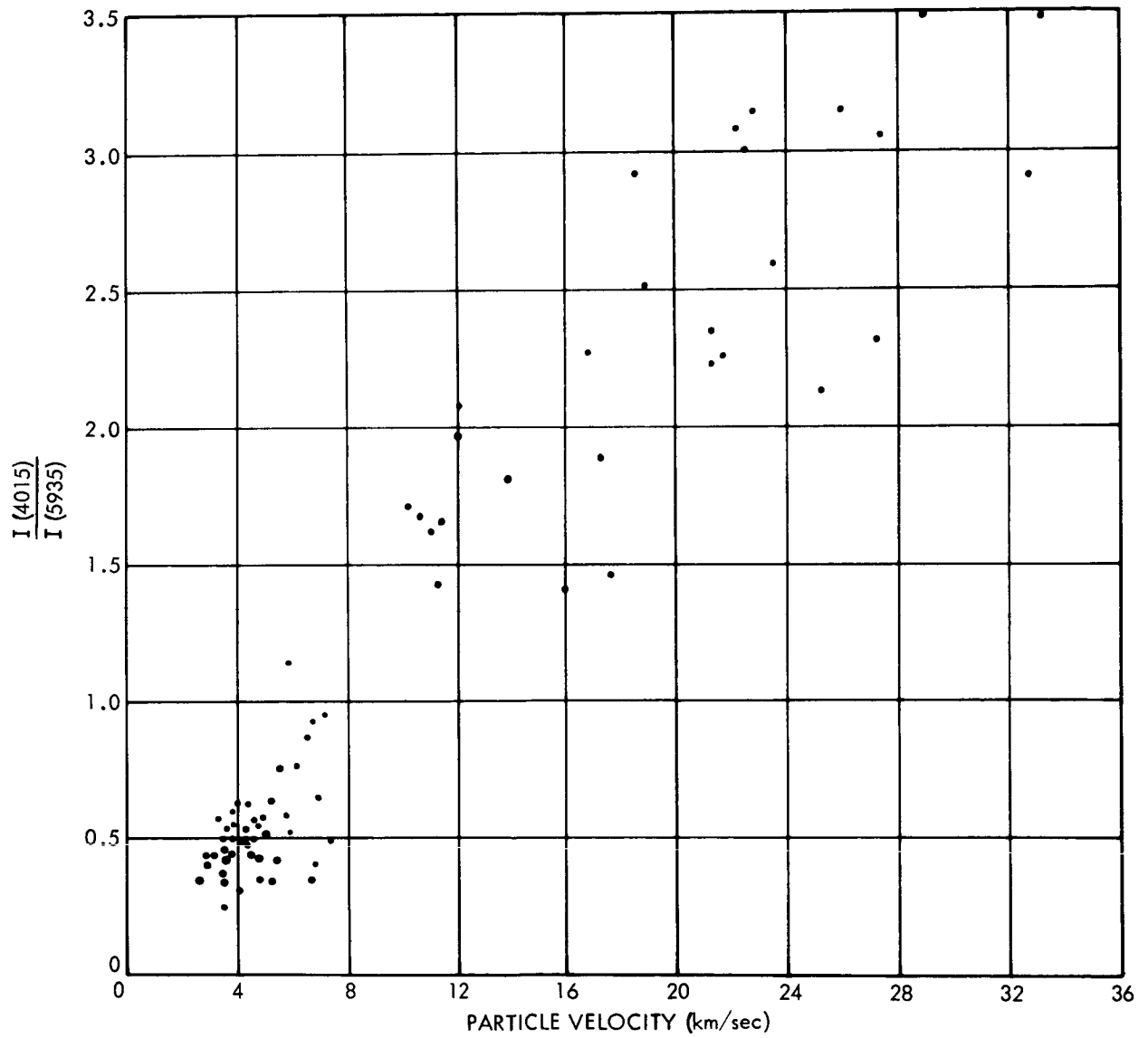


Figure 7. Direct Ratios of Impact Flash Intensity at 4015 Å and 5935 Å as a Function of Velocity for a Tantalum Target. In this case, the output signals from the PMT's were integrated.

velocity for each of the PMT's. A smooth curve was fitted to each set of data. The ratio of the values of the appropriate two curves at a selected velocity then yielded an average maximum blackbody temperature at that velocity.

The data are presented in Figs. 8 through 11. The points represent the logarithms of the measured values of the peak signal amplitude in arbitrary units normalized to the measured particle mass at the velocity indicated. The strong velocity dependence of the light flash as measured at a fixed wavelength is evident from these figures, since the light-flash amplitude increases by about 5 or 6 orders of magnitude over the velocity range covered. The curves were fitted to the data points by an iterative process. First the unweighted data were fitted to polynomials of second and third degree by standard computer methods. Gaps in the distribution of data points prevented an entirely satisfactory curve fit by this technique. Next, average values of the normalized light-flash amplitudes were determined over narrow velocity intervals, and these values were fitted by inspection. The curves defined in this manner and the computer-generated curves were compared for consistency. Obvious differences were rationalized by inspection, and the final curves as indicated in the figures were defined. Obviously, personal judgment plays a major role in defining the curves this way. Although the element of judgment precludes a quantitative estimate of the fitting errors, it is felt that the final results are quite representative of the actual temperatures involved. The final results relating apparent blackbody temperatures to impact velocity are given in Figs. 12 through 15.

As was mentioned above, the highest quality data were obtained when the output signals from the PMT's were integrated. Results obtained under these conditions are shown in Fig. 12 for a tantalum target and in Fig. 13 for the fused-quartz target. In both cases the apparent temperature increases with velocity, as might be expected, but appears to be asymptotically approaching a limiting temperature of about 5000°K . Although the problem has not

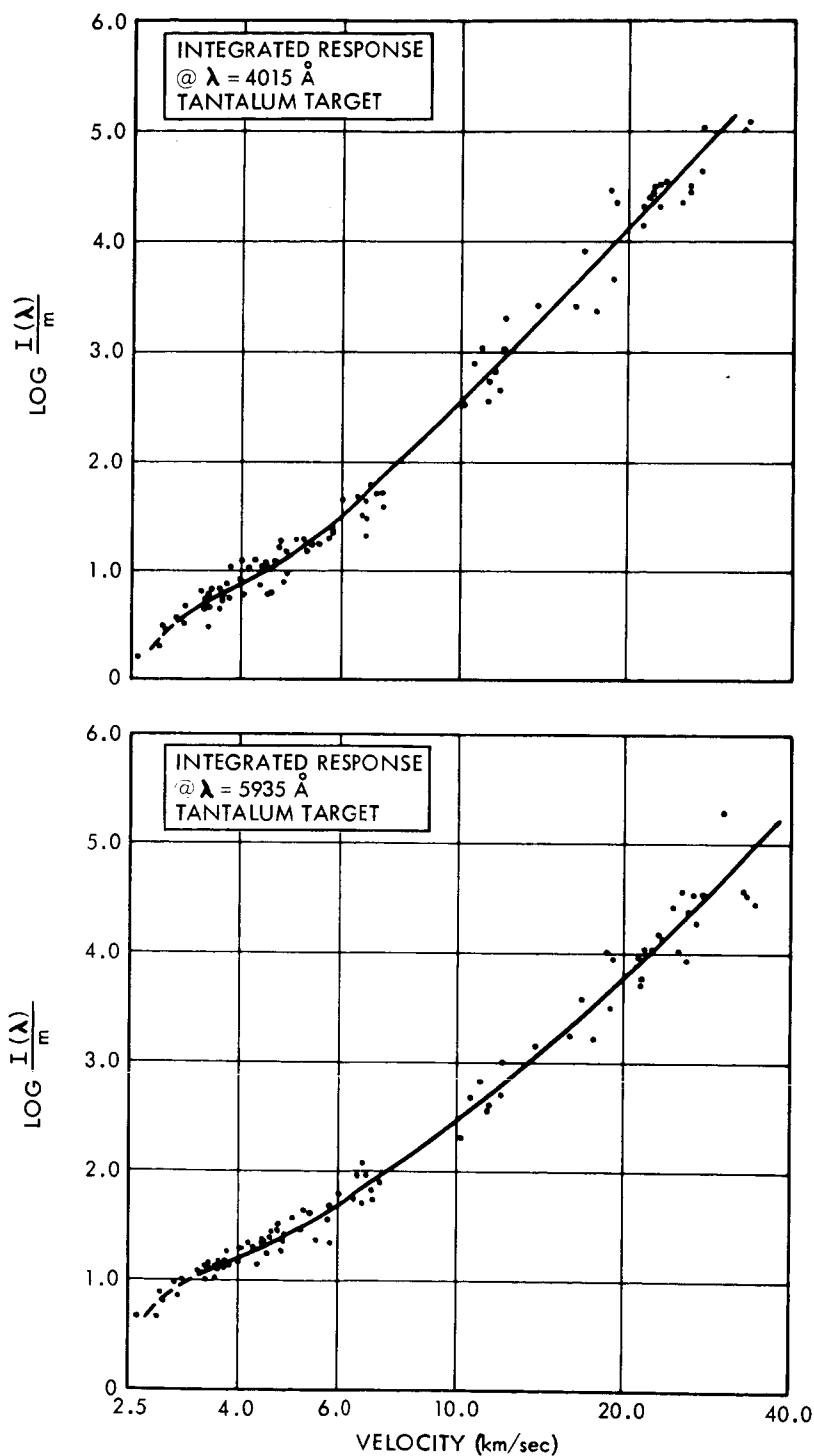


Figure 8. Logarithm of the Integrated Light Flash Intensity Normalized to Particle Mass as a Function of Velocity for PMT's Sensitive at 5935 Å and 4015 Å and a Tantalum Target.

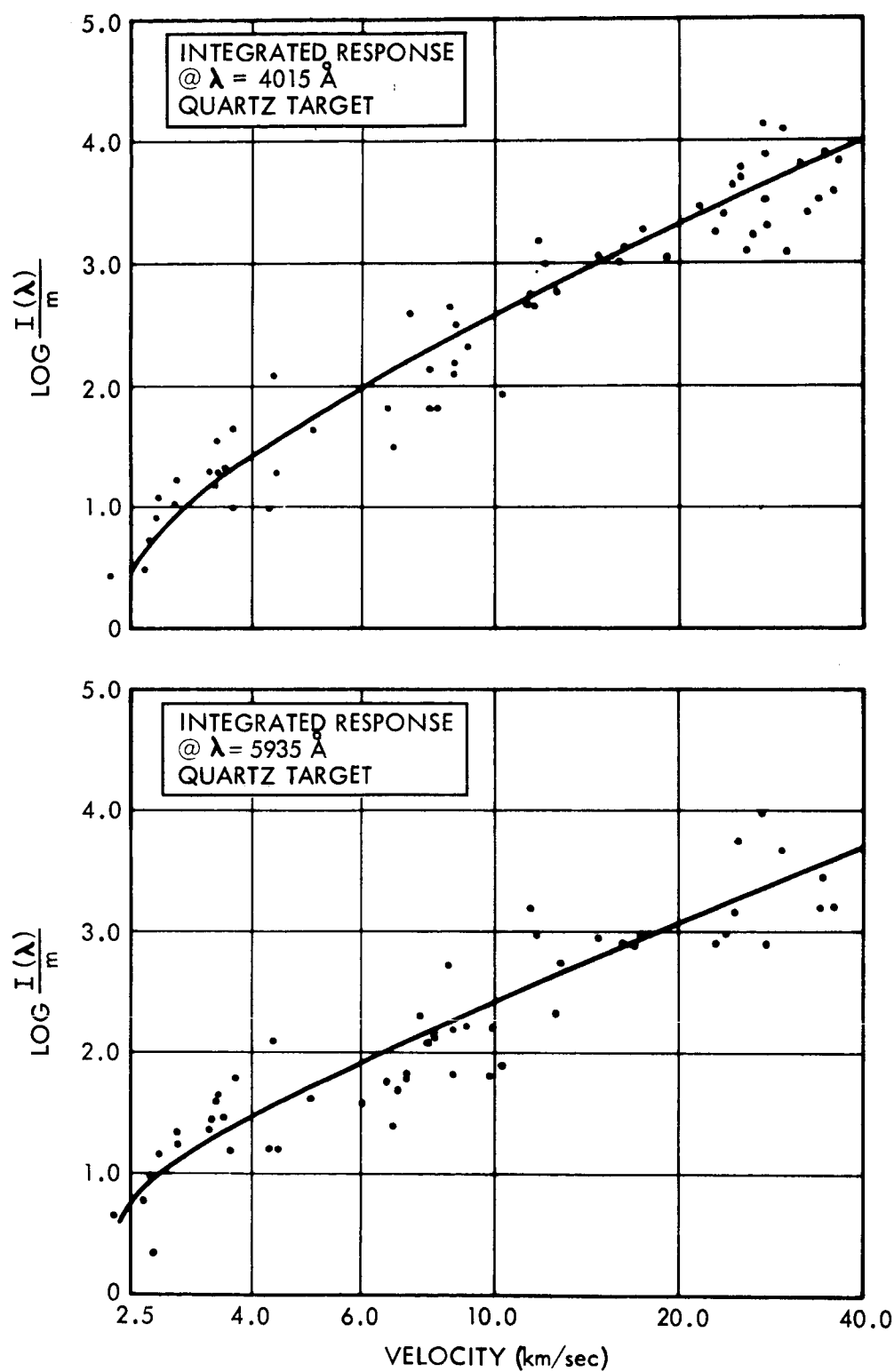


Figure 9. Logarithm of the Integrated Light Flash Intensity Normalized to Particle Mass as a Function of Velocity for PMT's Sensitive at 5935 Å and 4015 Å and a Fused-Quartz Target.

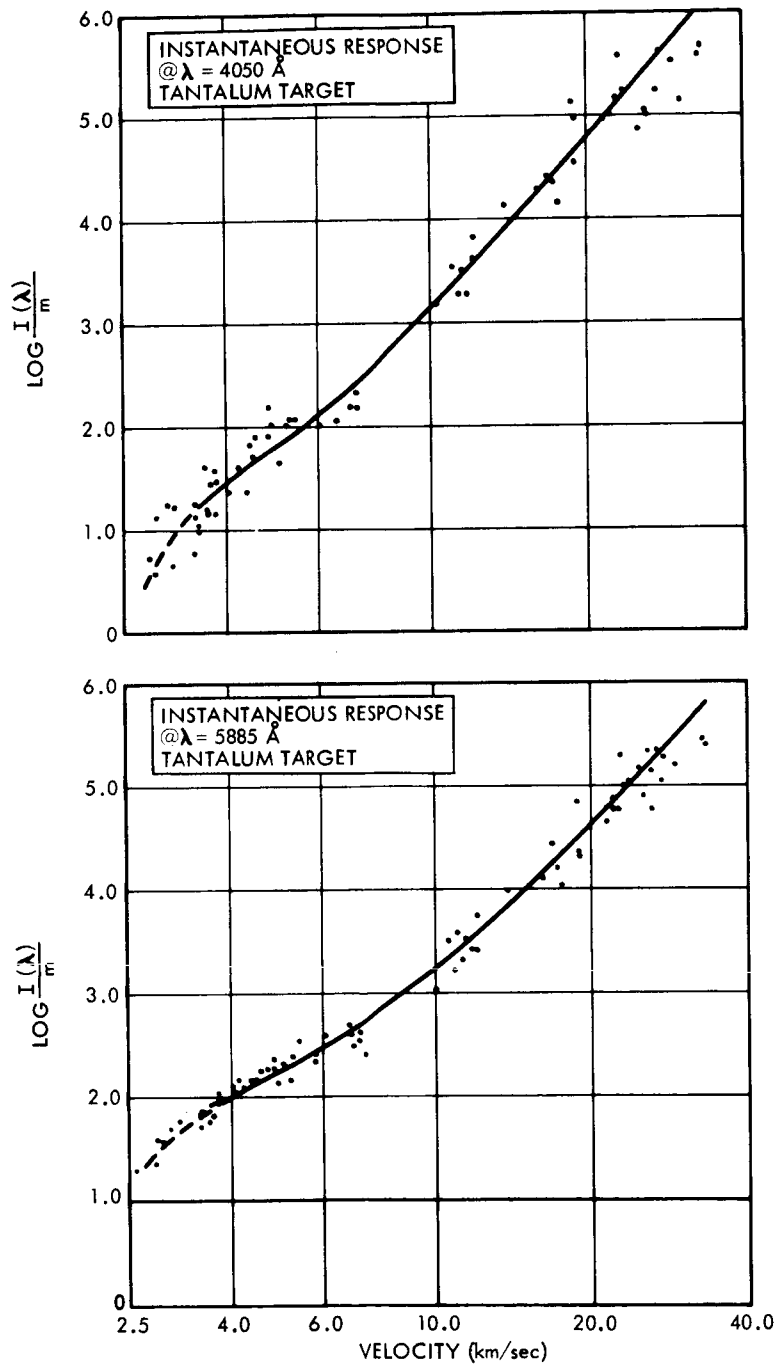


Figure 10. Logarithm of the Maximum Instantaneous Flash Intensity Normalized to Particle Mass as a Function of Velocity for PMT's Sensitive at 5885 Å and 4050 Å and a Tantalum Target.

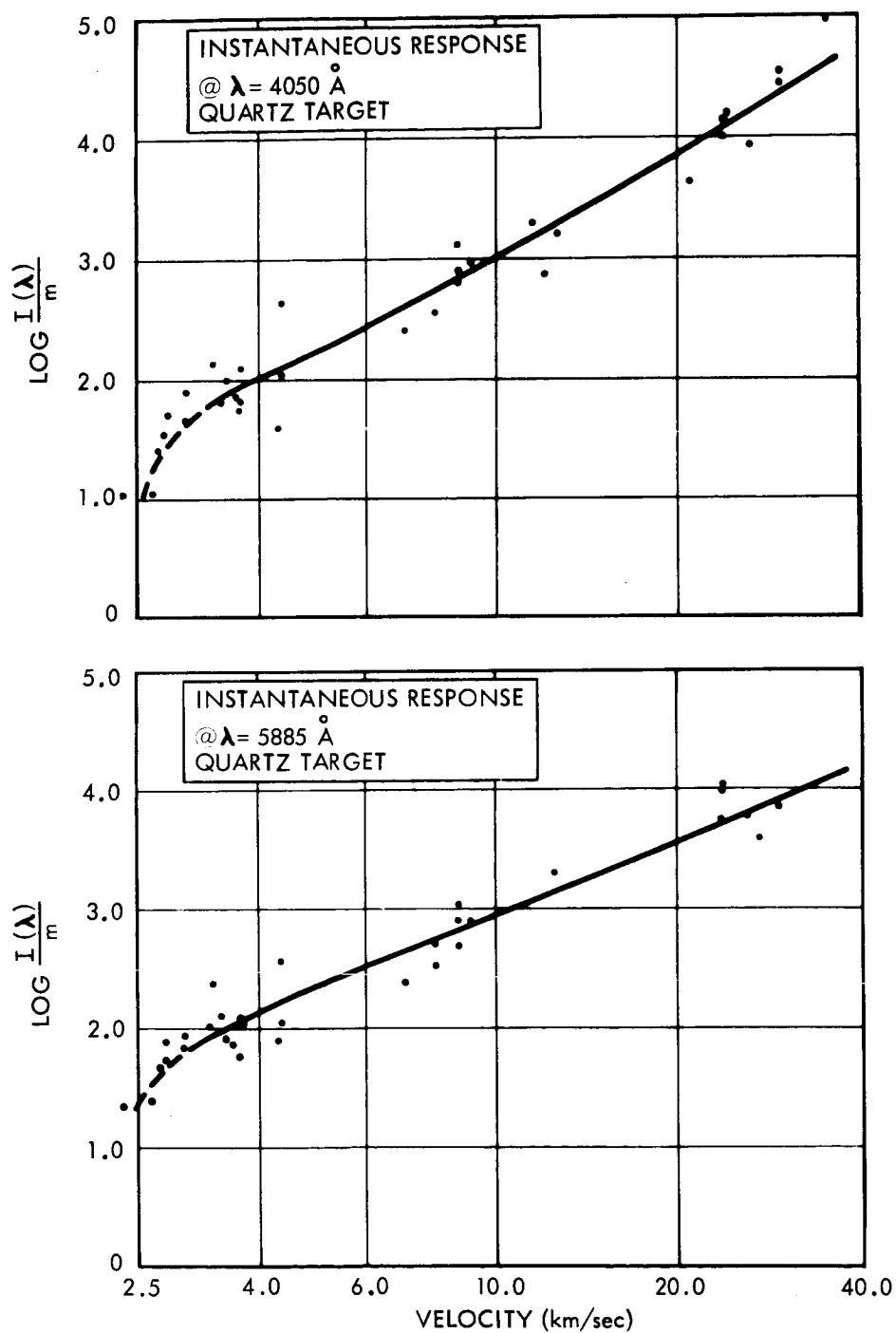


Figure 11. Logarithm of the Maximum Instantaneous Flash Intensity Normalized to Particle Mass as a Function of Velocity for PMT's Sensitive at 5885 Å and 4050 Å and a Fused-Quartz Target.

been treated analytically, it is probably safe to assume that the temperature limit is imposed by more efficient radiation cooling at higher temperatures and by the absorption of energy by competing mechanisms, such as ionization of the vapor atoms.

Although the same limiting temperature is approached for both types of targets, markedly higher temperatures are measured at low velocities with the quartz target. The lower heat conductivity of quartz may account for this effect, since the energy release is confined to a smaller volume of material at a correspondingly higher temperature. The apparent difference in measured temperatures at about 3 km/sec and below is probably the result of uncertainties in the curve fitting procedure rather than any actual difference. Also, the radiation levels in this region barely exceed the threshold for detection.

The temperature measurements made with the wideband-response PMT's are shown in Figs. 14 and 15 for the tantalum and quartz targets, respectively. Generally, the results obtained are similar to those discussed above; however, the curves are more complicated in form. It is felt that this difference arises from uncertainties in fitting the individual curves to the data points. For example, the increase in temperature indicated at about 25 km/sec in Fig. 14 arises from a small number of data points and may represent only a statistical fluctuation.

It is interesting to compare the results here with the results of similar experiments conducted by Rosen and Scully (Ref. 2). In their experiments the apparent blackbody temperature was measured for glass particles impacting on a lead target over the velocity range of about 4 to 15 km/sec. They found that the data, when plotted in the same form as shown in Fig. 12, could be fitted by a straight line, which implies that the ratio of intensities is proportional to the impact velocity raised to some power. Over the same velocity range, a straight line would provide a reasonably close approximation to the segment of the curve shown in Fig. 12. Furthermore, the maximum temperature they measured

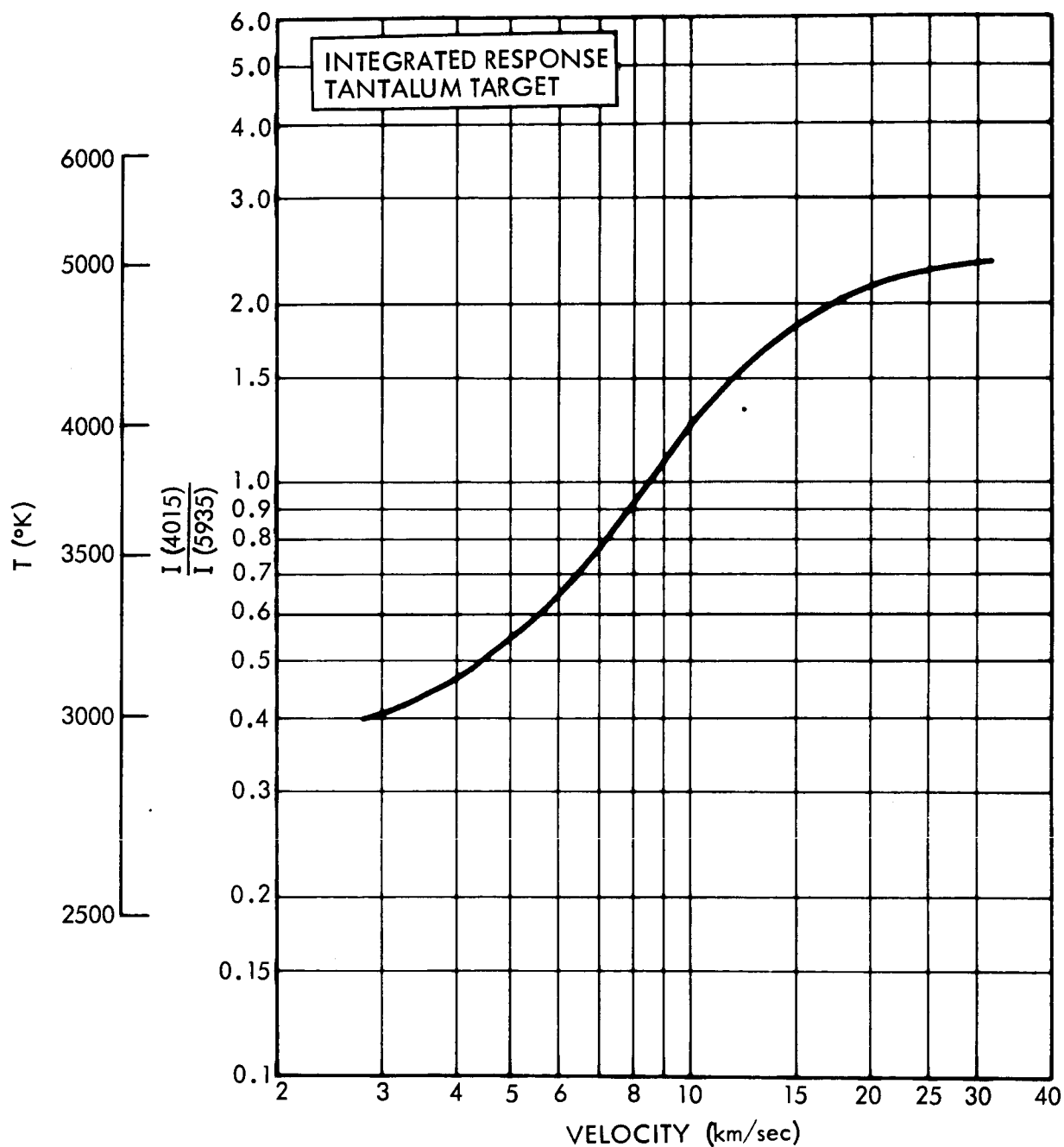


Figure 12. Apparent Blackbody Temperature of the Impact Light Flash as a Function of Particle Velocity obtained from Integrated Light Intensity Measurements on a Tantalum Target.

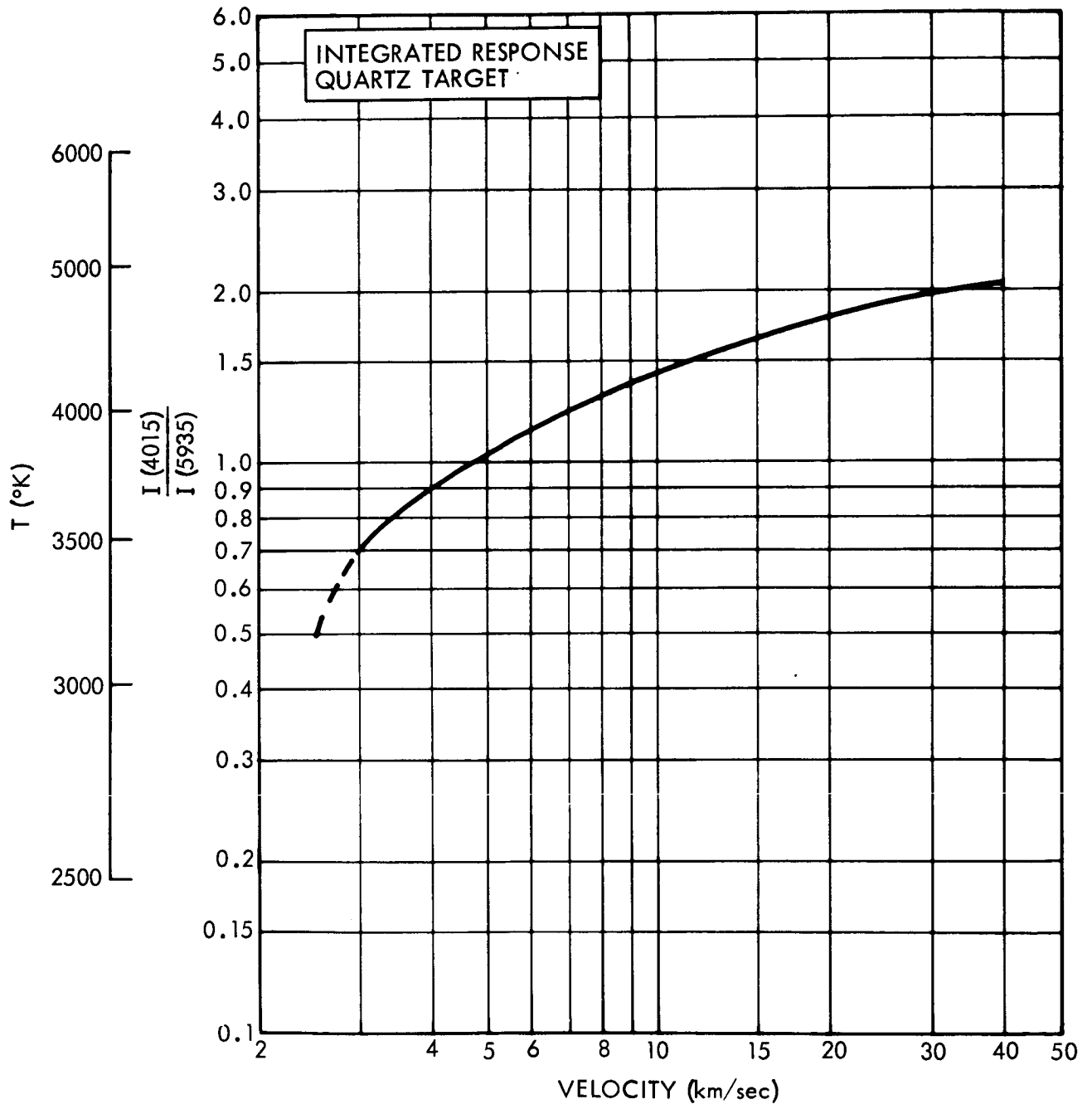


Figure 13. Apparent Blackbody Temperature of the Impact Light Flash as a Function of Particle Velocity obtained from Integrated Light Intensity Measurements on a Fused-Quartz Target.

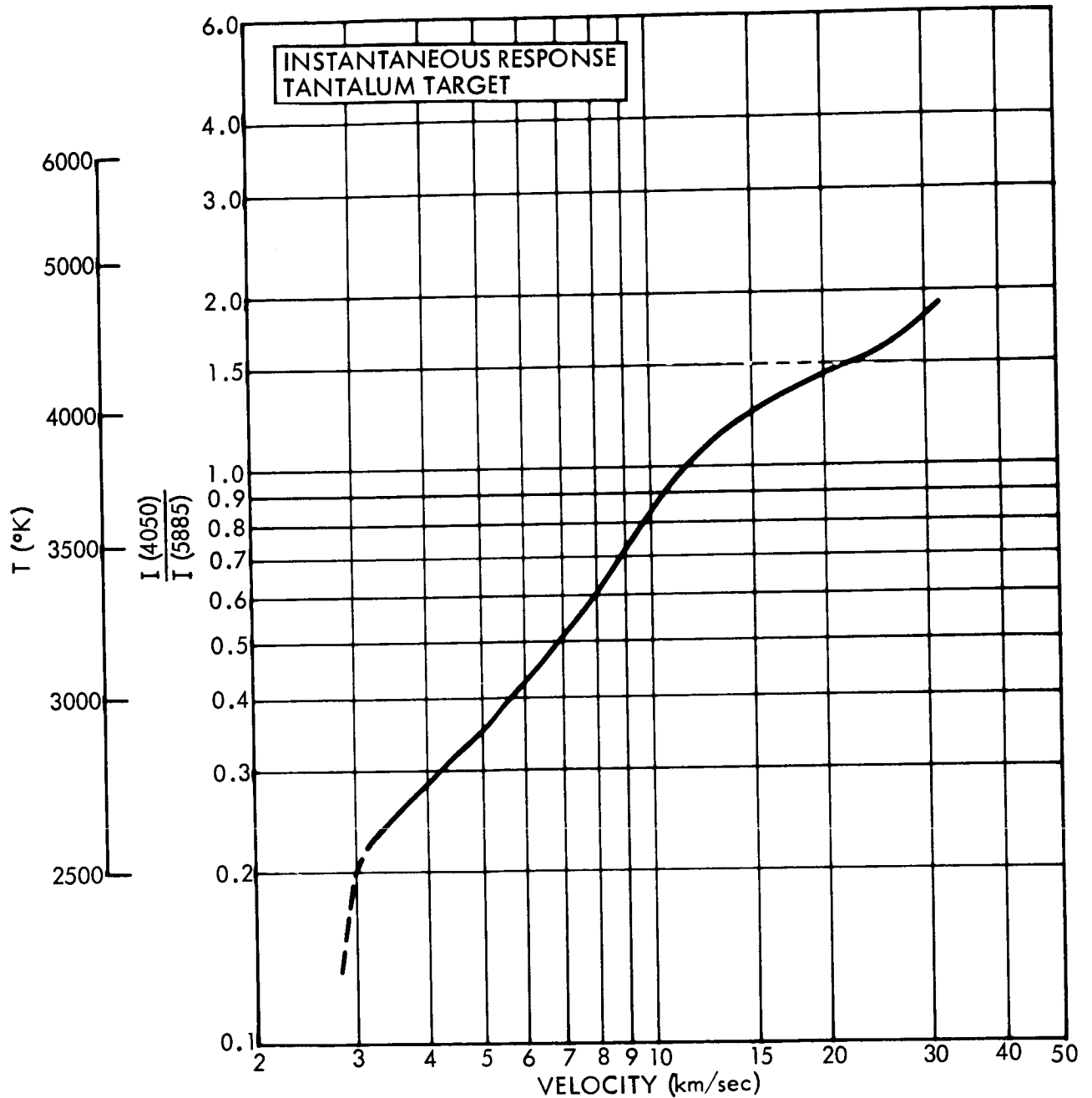


Figure 14. Apparent Blackbody Temperature of the Impact Light Flash as a Function of Particle Velocity obtained from Maximum Instantaneous Flash Intensity Measurements on a Tantalum Target.

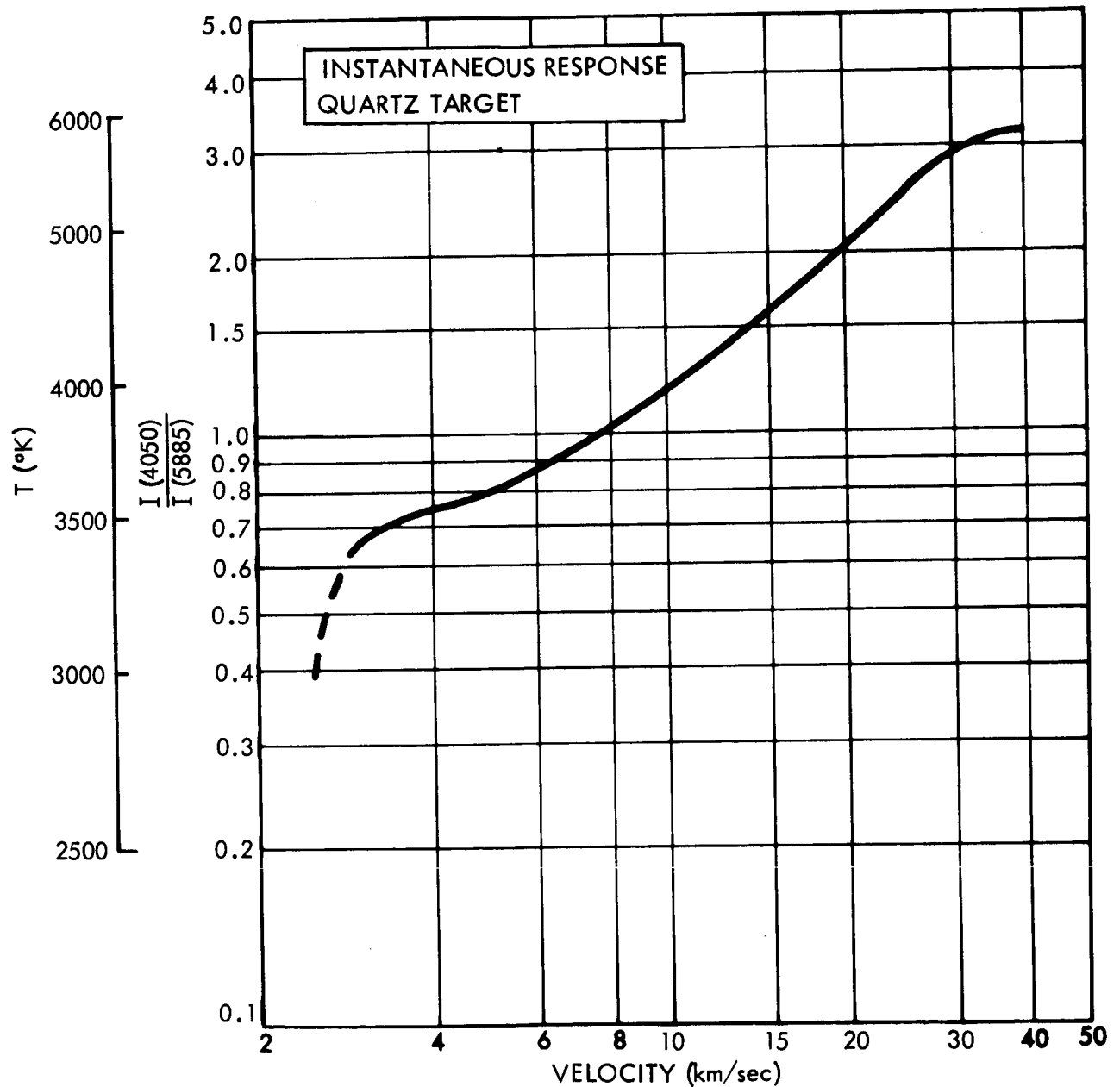


Figure 15. Apparent Blackbody Temperature of the Impact Light Flash as a Function of Particle Velocity obtained from Maximum Instantaneous Flash Intensity Measurements on a Fused-Quartz Target.

was about 5000°K , which is nearly identical to the maximum temperature measured here. Thus the results from the two experiments are compatible over the velocity range where direct comparison is valid. However, results obtained with higher-velocity particles show conclusively that the extrapolation to meteoric velocities suggested by Rosen and Scully is not valid.

IV. SUMMARY

The experiments described above have extended measurements on the impact light flash to particle velocities of nearly 40 km/sec. The very strong velocity dependence exhibited by the impact flash suggested that the source of light was similar to a black-body radiator. On this assumption, two-color photometric measurements designed to determine an "apparent" blackbody temperature were conducted. The results indicate that the apparent temperature increases rapidly up to about 15 km/sec. At higher velocities the rate of temperature increase is smaller and asymptotically approaches a value of about 5000°K . The results obtained here are in good agreement with the results of Rosen and Scully over the velocity range common to both experiments.

As suggested earlier, the results here are related to meteorite detection systems and to basic studies of hypervelocity impact phenomena. Clearly, additional work, both theoretical and experimental, is required to correlate the results obtained here with other properties of high-speed impact.

REFERENCES

1. O. E. Berg and L. H. Meridith, Journal of Geophysical Research, Vol. 61, 751 (1956).
2. F. D. Rosen and C. N. Scully, Proceedings of the Seventh Hypervelocity Impact Symposium, Vol. VI, Published by the Martin Company, Orlando, Florida, February, 1965.
3. R. L. Bjork, Proceedings of the Sixth Hypervelocity Impact Symposium, Vol. II, Published by the Firestone Tire and Rubber Co., Cleveland, Ohio, August, 1963.
4. C. J. Maiden, J. W. Gehring, and A. R. McMillan, "Investigation of Fundamental Mechanisms of Damage to Thin Targets by Hypervelocity Projectiles," Final Report TR 63-225, September, 1963.
5. J. F. Friichtenicht and J. C. Slattery, "Ionization Associated with Hypervelocity Impact," NASA Technical Note TN D-2091, August, 1963.
6. R. W. Grow, R. R. Kadesch, E. P. Palmer, W. H. Clark, J. S. Clark, and R. E. Blake, Proceedings of the Fourth Hypervelocity Impact Symposium, Published by Air Proving Ground Center, Eglin Air Force Base, Florida, September, 1960.
7. J. F. Friichtenicht, Rev. of Sci. Instr., Vol. 33, 209 (1962).
8. H. Shelton, C. D. Hendricks, Jr., R. F. Wuerker, Journal of Appl. Phys., Vol. 31, 1243 (1960).

**RESPONSE OF MICROPHONE METEORITE DETECTORS TO THE
IMPACT OF HIGH VELOCITY PARTICLES**

APPENDIX L

TECHNICAL REPORT

RESPONSE OF MICROPHONE METEORITE DETECTORS TO THE
IMPACT OF HIGH VELOCITY PARTICLES

May 1965

Prepared for
National Aeronautics and Space Administration
Washington, D. C. 20546

Contract No. NASw-936

J. F. Friichtenicht
Prepared by
J. F. Friichtenicht

D. B. Langmuir
Approved by
D. B. Langmuir
Director

PHYSICAL ELECTRONICS LABORATORY
Physical Research Division
TRW Space Technology Laboratories
One Space Park, Redondo Beach, California

RESPONSE OF MICROPHONE METEORITE DETECTORS TO THE
IMPACT OF HIGH VELOCITY PARTICLES*

I. INTRODUCTION

Most of the direct measurements on the properties of micro-meteoroids have utilized microphone detectors. These consist of piezoelectric crystals which are mechanically coupled to metallic plates or "sounding boards". The crystal responds to mechanical vibrations induced in the sounding board by the impact of a micro-meteorite. The output of the microphone is an electrical signal with an amplitude proportional to the magnitude of the mechanical vibrations. Despite the widespread use of this type of sensor, the overall response of the detector to dynamic properties of the meteoroids has not been firmly established. In their comprehensive compilation of meteorite data, Alexander, et al¹ assumed a momentum dependence based on the results of tests conducted at very low impact velocities. A momentum dependence has also been reported² for impact velocities up to about 4 km/sec. In contrast, the theoretical treatment of Stanyukovich³ and the experiments of Denardo⁴ using large particles at velocities up to 7.8 km/sec suggest an energy dependence.

This report gives the results of tests using very small particles with impact velocities up to 7.5 km/sec. Although the results are not completely definitive, they show that the overall response of a microphone detector lies somewhere between the momentum and energy dependences suggested by other experimenters.

II. EXPERIMENTAL APPARATUS AND PROCEDURES

High speed particles from the STL electrostatic accelerator⁵ were used for the measurements described in this report. In this device, small particles are charged electrically by an inductive process⁶ and are injected into the accelerating field of a 2-million volt Van de Graaff generator. The final velocity attained

*This work conducted under NASA Contracts NAS5-763 and NASw-936.

by the particle is given by

$$v = (2 qV_a/m)^{1/2} \quad (1)$$

where V_a is the accelerating voltage and m and q are the particle mass and charge. As shown in Ref. 6, the q/m of the particles is proportional to the reciprocal of particle radius. Consequently, the electrostatic method of accelerating particles is applicable only to small particles. Under optimum conditions, a 1 micron diameter iron particle achieves a final velocity of about 7 km/sec. Higher velocities can be achieved with smaller particles, but the momentum of smaller particles is reduced correspondingly. The limiting sensitivity of the microphone detectors prohibited the use of higher velocity particles for these experiments.

The charge and velocity of each particle from the accelerator are determined prior to impact by measuring the magnitude and duration, respectively, of a voltage signal induced on a cylindrical drift tube of known capacitance and length which the particle traverses axially. The charge is given by $q = CV_i$ where V_i is the magnitude of the induced voltage pulse and C is the capacitance of the drift tube. The velocity is simply $v = l/t$ where t is the time required to pass through a cylinder of length l . Knowing the accelerating voltage, the mass of the particle can be computed from Eq. (1).

The signal on the drift tube was amplified and displayed on one trace of a dual beam oscilloscope while the signal from the microphone detector was displayed on the other. Both traces were triggered by the leading edge of the voltage pulse from the velocity-charge detector. By taking account of the flight time from the charge detector to the point of impact, one can be assured that both signals were produced by the same particle.

The crystal transducer acquired for these tests was typical of those used in flight experiments. It consisted of a cylindrically

shaped lead zirconate crystal encapsulated in an aluminum can. Preliminary tests showed that the microphone was not sufficiently sensitive to be used directly with particles from the accelerator. As a consequence of this, the crystal was removed from the can and suspended in a rubber grommet with its axis parallel to the beam of particles from the accelerator. The signal from the crystal was derived from a pickup loop at one end of the crystal. The face of the crystal exposed to the beam of particles was grounded. Two types of impact surfaces were used. The first was a layer of conducting silver paint while the other was a polished aluminum disc cemented to the crystal. Since there was no apparent difference in response for the different surfaces, the results from both were combined in the data analysis.

The signal from the microphone was fed to a wide band amplifier. The waveform at the output of the amplifier was an exponentially decreasing oscillatory signal with frequency of about 100 kc as illustrated in Fig. 1-a. The signal shown resulted from the impact of a glass bead dropped from a height of a few centimeters. To reduce some of the low frequency noise problems associated with mounting the microphone in the test chamber, the amplified signal was fed through a relatively low Q resonant circuit tuned to the resonant frequency of the crystal. The circuit is shown in Fig. 1-b and a typical signal is illustrated in Fig. 1-c. The amplitude of the microphone signal was measured at the point of maximum excursion from the base line. Since the circuitry is composed entirely of linear elements and the frequencies are fixed, it can be shown that the measured maximum amplitude is always proportional to the amplitude of the first half cycle at the output of the crystal.

III. RESULTS

Most of the hypotheses regarding the response of microphone detectors can be reduced to the form $V = K m v^a$ where the value of K depends upon the nature of the impact, m and v are

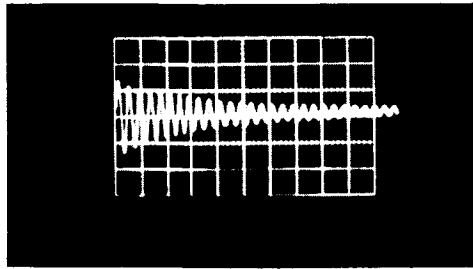


Figure 1-a

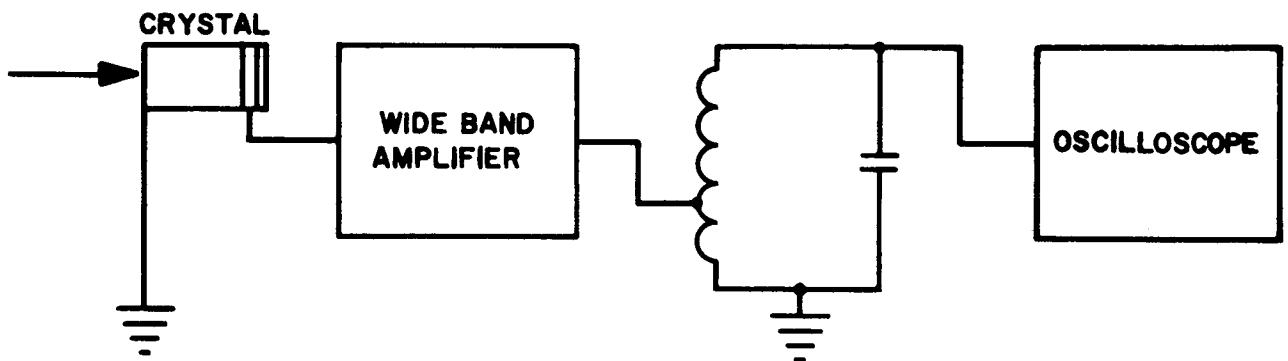


Figure 1-b

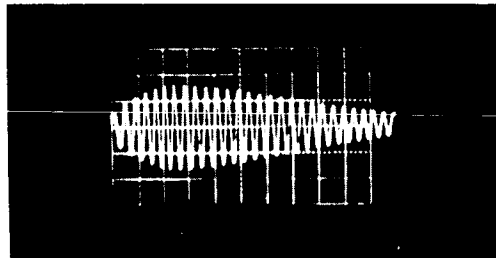


Figure 1-c

Figure 1. Schematic Diagram of the circuit used in the Microphone Detector Tests. The waveform at the top of the figure is obtained at the output of the amplifier while the waveform at the bottom is at the output terminal of the tuned circuit.

the particle mass and velocity, and α is an undetermined exponent. There are essentially three types of impacts to be considered. These are elastic impacts, completely inelastic impacts, and inelastic impacts enhanced by the expulsion of material from the crater which increases the momentum imparted to the crystal. For elastic impacts $K = 2$ and $\alpha = 1$. For the completely inelastic case K and α would both be unity. The third type of impact is probably the most applicable in the present context and is certainly the most difficult to interpret. R. L. Bjork, quoted by Dubin,⁷ contends that the momentum contribution from expelled material may be as much as two and one-half times the momentum of the impacting particle at 70 km/sec. Although it is probably an oversimplification of the case, the assumption has been made that K is a constant over the experimental range and that the velocity dependence is contained completely by the exponent α .

The data are presented in two forms. In Fig. 2 the microphone output signal is normalized to the particle mass and plotted as a function of impact velocity. Since the particle parameters are near the limiting sensitivity of the microphone system, the data points exhibit considerable scatter which prohibits precise measurements. However, the trend of the data is obvious. A line drawn through the data points by eye as shown yields a value for α of 1.7. This is in contrast to $\alpha = 1$ for momentum dependence and $\alpha = 2$ for an energy dependence.

The data from Fig. 2 are replotted in Fig. 3 to more adequately demonstrate the departure from the commonly assumed momentum dependence. Here the magnitude of the microphone output signal is plotted against particle momentum. An independent momentum calibration point was obtained by dropping plastic beads weighing approximately 100 micrograms on the face of the crystal from a known height. This was done in air, but no drag corrections were made nor was the coefficient of restitution taken into account. However, the computed momentum was good to about 10% which is sufficient for comparison purposes. Using this point and the

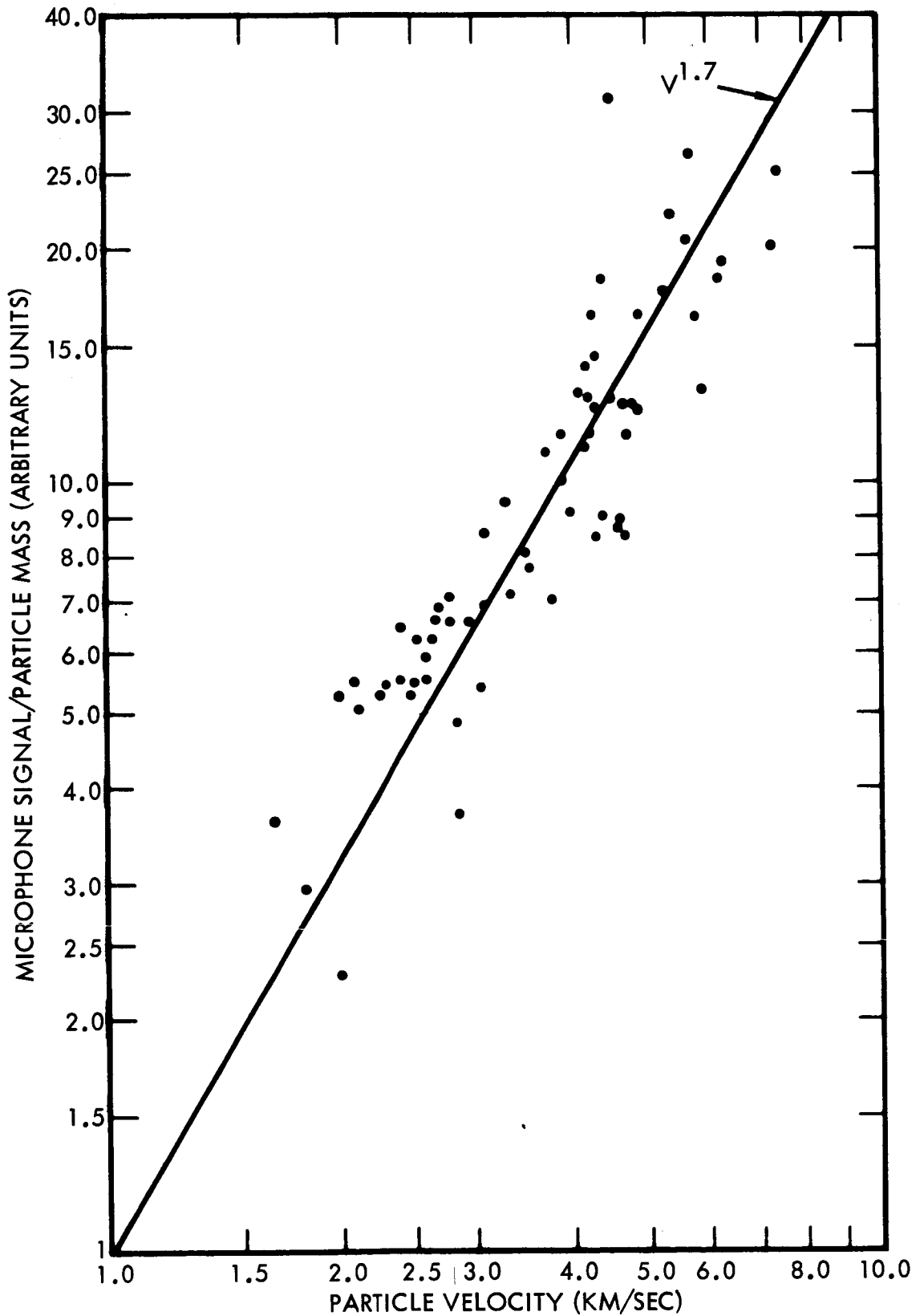


Figure 2. Amplitude of Microphone signal normalized to particle mass plotted as a function of impact velocity.

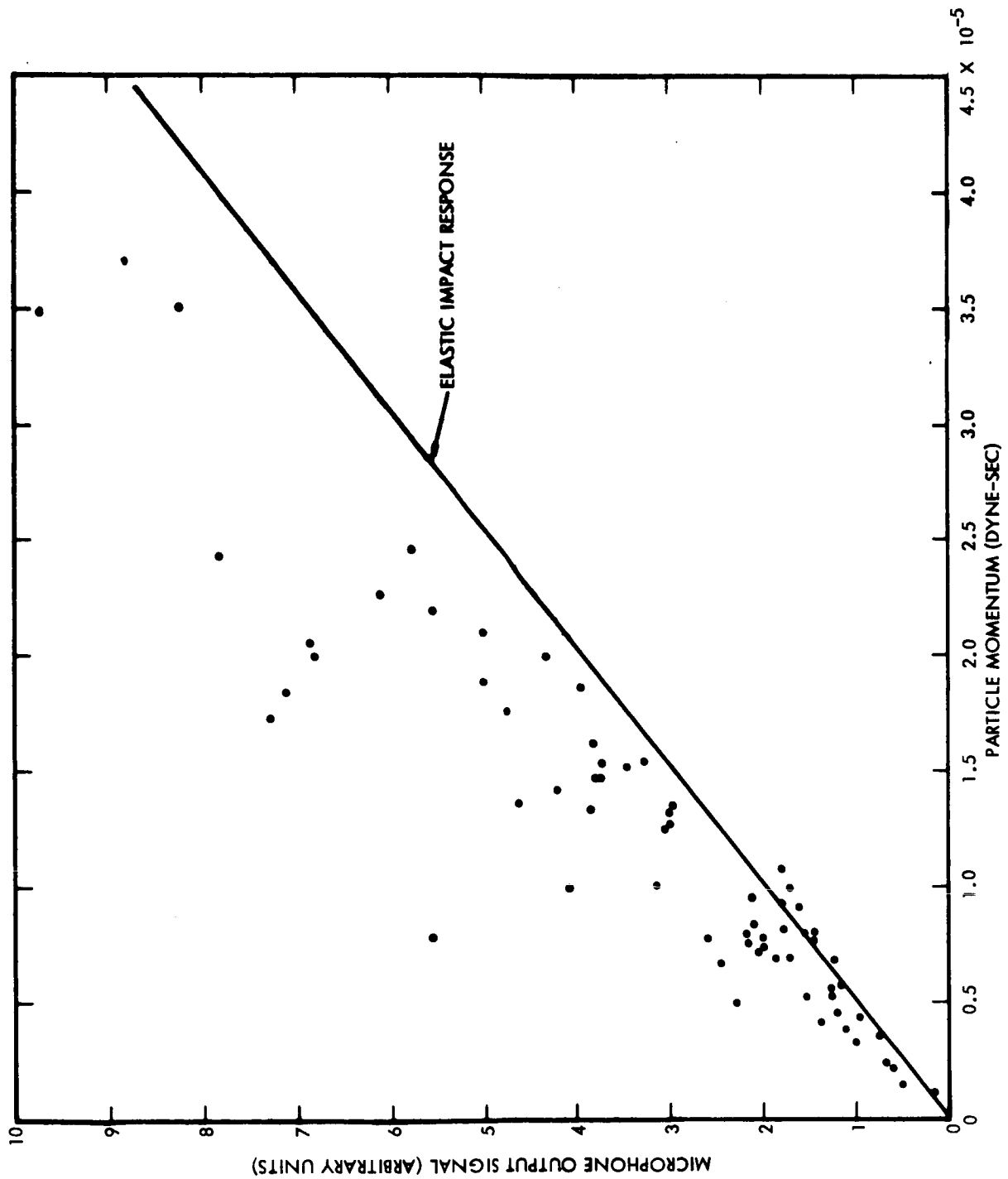


Figure 3. Output Pulse Amplitude of the Microphone Detector vs. the momentum of the impacting particle.

origin as the other, the elastic impact line corresponding to the transfer of two units of momentum was drawn on the graph. Nearly all of the data points obtained with high velocity particles lie above the elastic impact line. This indicates that the ejected material imparts at least as much (and in most cases more) momentum than does the impacting particle over the velocity range covered.

IV. SUMMARY

Although considerable modification of a typical microphone detector was required in order to obtain measurable signals, the results of the measurements described above are quite general in nature. The results imply that the response of microphone detectors cannot be characterized as simply momentum or energy dependent. In order to more fully assess the situation, a much more detailed study should be conducted. On the other hand, the empirical approach, such as that utilized here, provides information which should be considered in the analysis of data from flight experiments.

REFERENCES

1. W. M. Alexander, C. W. McCracken, L. Secretan, and O.E. Berg. Paper presented at the Cospar Meeting, Amsterdam, May, 1962. (To be published.) Also available as NASA TN D-1669, 1962.
2. G. D. Anderson, et al, Proc. Third Symposium on Hypervelocity Impact, F. Genevese Ed., Armour Research Foundation, Illinois Institute of Technology, Chicago, 1959, p. 361.
3. K. P. Stanyukovich, Artificial Earth Satellites, Vol. 4, Plenum Press, New York, 1961, p. 292.
4. B. Pat Denardo, NASA Technical Note TN D-1210, 1962.
5. J. F. Friichtenicht, Rev. Sci. Instr., Vol. 33 (1962) p. 209.
6. H. Shelton, C. D. Hendricks, Jr., and R. F. Wuerker, J. Appl. Phys., Vol. 31 (1960) p. 1243.
7. M. Dubin, Space Research, Proc. of the First International Space Science Symposium, Interscience Publishers, Inc., New York, 1960, p. 1042.

**THE INTERACTION OF MICROMETEORITES
WITH GASEOUS TARGETS**

APPENDIX M

22 July 1963

"The Interaction of Micrometeorites
with Gaseous Targets"

by

J. C. Slattery, J. F. Friichtenicht
and B. Hamermesh

Prepared for:

NASA Headquarters
Washington 25, D.C.

Contract No. NASw-561

PHYSICAL ELECTRONICS LABORATORY
Physical Research Division
Space Technology Laboratories, Inc.
One Space Park
Redondo Beach, California

TABLE OF CONTENTS

	Page
I. INTRODUCTION.	1
II. EXPERIMENTAL APPARATUS AND TECHNIQUES	4
III. MEASUREMENT OF THE DRAG COEFFICIENTS.	7
IV. MEASUREMENT OF THE HEAT TRANSFER COEFFICIENT.	9
V. SUMMARY	15
REFERENCES.	26

FIGURE CAPTIONS

- Figure 1. Schematic diagram of experiment.
- Figure 2. Photograph of experimental apparatus.
- Figure 3. Typical oscilloscope trace. The upper trace shows the output of the primary detector. The vertical scale is 0.1 volts/div and the sweep speed is 5.0 μ sec/div. The lower trace shows the output of the fifteen-station detector. The vertical scale is 0.1 volts/div and the sweep speed is 50 μ sec/div.
- Figure 4. Least-squares fit of reciprocal velocity versus time for a typical particle.
- Figure 5. Graph of charge versus time for a typical particle illustrating the method used to find the time of melting.
- Figure 6. Graph of charge versus time for a particle which displays loss of charge during latter part of trajectory.
- Figure 7. The solid curve is the Rayleigh limit (see text) for liquid particles with a surface tension of $\sigma=1200$ dynes/cm. Each cross and open circle represents one experimental particle. The cross represents the initial charge and the open circle represents the charge after the particle has melted.
- Figure 8. Graph illustrating measured velocity and measured light output for a typical particle. Included is a plot of particle temperature computed assuming a heat transfer coefficient of unity. See text for a more complete discussion.

THE INTERACTION OF MICROMETEORITES WITH GASEOUS TARGETS

J. C. Slattery, J. F. Friichtenicht and B. Hamermesh
Space Technology Laboratories, Inc.
One Space Park
Redondo Beach, California

ABSTRACT

Experiments have been conducted on the interaction of simulated micrometeoroids with gaseous targets. Iron spheres from 0.5 to 2.0 microns in diameter were accelerated to speeds up to 7 km/sec in the STL Electrostatic Accelerator. Oxygen, argon and air were used as target gases. Gas pressures ranged from 1 to 2 mm of Hg which insured that conditions for free molecular flow were realized. Values of the drag coefficient C_D and the heat transfer coefficient λ were determined. In this paper, λ is defined as the fraction of particle kinetic energy converted to internal energy and is applicable only for solid particles. The results are consistent with a value of C_D nearly equal to 1 for all of the gases. The values of λ depended upon the gas used and ranged from 0.8 to about 1.0.

I. INTRODUCTION

The entry of a meteoroid into the earth's atmosphere is observable from the earth by visual and radar techniques. Data from these observations are used to deduce physical parameters of the meteor and the upper atmosphere. However, the mass and density of the meteoroid are unknown and certain assumptions must be made concerning the physical constants involved. For example, values must be assigned to the drag coefficient, the efficiency of energy transfer to the particle, the fraction of kinetic energy converted to light and the efficiency for creating ion pairs. A summary of the theory of meteoric processes and a discussion of existing data may be found in Ref. 1. We are concerned in this paper with only the drag coefficient and the heat transfer coefficient.

Following the notation of Ref. 1, we will review briefly the theory of meteors. If a particle of mass m , having a velocity v , enters a region of the atmosphere having a density ρ , some of the momentum of the particle is transferred to the gas molecules and the particle is decelerated according to

$$m \frac{dv}{dt} = - \Gamma A \rho v^2 \quad (1)$$

where Γ is the drag coefficient and A is the projected area of the particle.

A second equation is obtained by considering the conservation of energy. A fraction Λ of the energy of the particle is converted into heat, which manifests itself by raising the temperature of the body, melting, vaporization, or fragmentation. In the general theory, it is assumed that the primary mechanism for energy dissipation is by vaporization of the meteoroid. The particle collides with a mass of gas equal to $(\rho v A)$ per unit time and since the relative velocity of particle and gas molecule is v , we find

$$\zeta \frac{dm}{dt} = - \frac{\Lambda}{2} A \rho v^3, \quad (2)$$

where ζ is the energy per unit mass required to vaporize the particle. The kinetic energy lost by deceleration has been neglected in Eq. (2), since this is negligible for naturally-occurring meteoroids.

The ablated atoms collide with gas molecules and radiation is emitted. Since an iron atom moving at a velocity of 22 km/sec has an energy of about 140 electron volts, it is clear that there is sufficient energy to excite and ionize the atoms of the meteoroid as well as the atoms in the atmosphere. Meteor streams generally have velocities above 22 km/sec and meteor spectra indicate that the excited atoms of the meteoroid emit most of the observed radiation.

If τ is the fraction of the kinetic energy of the ablated material which is converted into light, the intensity of light I emitted is

$$I = - \frac{\tau}{2} \left(\frac{dm}{dt} \right) v^2. \quad (3)$$

Since the ablated atoms ionize the gas, we may write an equation for the number q of ion pairs formed per centimeter of travel in the gas. This equation is

$$q = - \left(\frac{dm}{dt} \right) \frac{1}{v} \frac{\beta}{\mu} \quad (4)$$

where β is the ionization probability and μ is the mass of the evaporated ion.

The four equations above may be applied to the experimental data to determine some of the parameters required by the theory. A visual or photographic measurement yields v , dv/dt , ρ (from the height of occurrence and a knowledge of the height versus the density of the atmosphere), and I as functions of time. The radar measurements yield v , ρ and q . We note that the four equations involve 6 parameters Γ , Λ , A , ζ , τ and β , so that we have an underdetermined set of equations. A further difficulty occurs because some of these parameters are likely to be velocity dependent.

For the purposes of this paper, we will be concerned mainly with Eqs. (1) and (2). As will be described later, meteoroid processes can be studied in the laboratory under controlled conditions. The experimental apparatus allows one to project artificial micrometeoroids having diameters the order of 1 micron and moving at speeds up to 8 km/sec into gas targets. The composition and density of the target gas are known and the parameters of the particles are specified.

It is well to point out that there are certain differences between these experiments and the entry of a meteoroid into the earth's atmosphere. The meteoroids which give rise to visible trails and radar echoes are much larger than the experimental particles. Therefore, the thermal equilibrium time constant for our particles is much shorter. In most respects this is a desirable characteristic for the kinds of measurements we have made since the phase (solid, liquid or vapor) of the particle is more easily specified. A further difference is that the change of velocity is not negligible, so in applying Eq. (2) corrections must be made for the loss of kinetic energy due to deceleration. In the general theory, Eq. (2) is valid only for the case where the meteoroid is losing mass by ablation. In fact, it is assumed that meteoroids

are not observable until ablation occurs. Most of our measurements, however, have been concerned with a determination of the heat transfer coefficient while the particle is in the solid phase. This quantity, denoted by λ , is defined in Section IV. Finally, the experimental particles are electrically charged. This difference does not alter the basic measurements but does provide a very useful tool for following the particle and observing it as it undergoes changes of phase.

In the experiments, simulated micrometeoroids were projected into various gases and m , v , dv/dt and charge loss were measured as functions of time. Since the particles are very nearly spherical and their density is known, the value of A may be found. Using an appropriate value of ζ with Eqs. (1) and (2), values of Γ and λ were obtained. In addition, the emission of light was observed as a function of time. While these last measurements can lead to values of τ , only preliminary results of this type will be discussed.

II. EXPERIMENTAL APPARATUS AND TECHNIQUES

The STL electrostatic hypervelocity accelerator² was used as a source of high-speed particles for all of the measurements described in this paper. In this accelerator, small particles are charged electrically by a process described elsewhere³ and are injected into the accelerating field of a 2-million volt Van de Graaff generator. Here they are accelerated to a velocity given by

$$v = \left(\frac{2qV}{m} \right)^{1/2} \quad (5)$$

where V is the accelerating potential, m is the mass of the particle and q its charge. As described in Ref. 3, the q/m ratio obtainable is proportional to the reciprocal of the particle radius. Consequentl

the electrostatic method of accelerating particles is most effective for particles with small radii. Under optimum conditions, a one-micron diameter iron particle achieves a final velocity of about 7 kilometers/second. Higher velocities can be obtained with particles of less dense materials. For example, carbon particles have been accelerated to more than 20 km/sec. For the experiments described here, only carbonyl iron spheres with an average diameter of about 1.5 microns were used.

The charge and velocity of each particle issuing from the accelerator are determined by measuring the magnitude and duration, respectively, of a voltage signal induced on a cylindrical drift tube of known capacitance and length, through which the particles pass. The charge is given by $q = CV_1$, where V_1 is the magnitude of the induced voltage pulse and C is the capacitance of the drift tube to ground. The velocity is simply $v = \ell/t$, where t is the time to pass through a cylinder of length ℓ . The mass (hence, the radius) of the particle is found from $m = 2qV/v^2$, where V is the accelerating voltage. Generally, the signal on the drift tube is amplified and displayed on an oscilloscope trace which is photographed for later analysis. Detectors for determining particle position relative to the axis of the detector have also been developed. These are described in Ref. 3.

The conditions for hypersonic free molecular flow for particles of this size range are satisfied for pressures of about 25 mm Hg, or less. Since the accelerator section is maintained at high vacuum, a transition region from high vacuum to the gas target is required. This is accomplished by means of a differential pumping system illustrated schematically in Fig. 1. Two intermediate pressure regions are provided. Gas flow from one region to another is restricted by means of the constrictions shown in the figure. The smallest constriction is 0.050" in diameter and 0.60" long. With

this system, pressures up to about 5 mm Hg can be maintained in the target section while maintaining a pressure of 2.0×10^{-5} mm Hg in the accelerator section. The conditions for free molecular flow are also satisfied at much lower pressures, but the energy loss per unit path length becomes so small that measurements of the effects are difficult. For the sake of convenience, we have chosen to work at pressures of about 2 mm of Hg. The pressure in the target region is adjusted by the variable leak control and the pressures in the various regions are monitored by appropriate gauges. In operation, particles from the accelerator pass through a charge-velocity detector, then through the series of constrictions into the target region. The focusing properties of the accelerator are such that about 50% of the particles from the accelerator enter the target region.

Two types of measurements were conducted during the course of this work. One was concerned with the measurement of particle position and charge as a function of time. This measurement made use of a series of fifteen coaxial drift tubes (referred to as station detectors in Fig. 1) interspersed with grounded drift tubes. Each of the active drift tubes functions as a charge-velocity detector as described above. The detectors were connected in parallel and amplified by a common preamplifier.

Preliminary measurements on radiant energy emission were made with the same target chamber. Ten photomultipliers (RCA Type 7117 Multiplier Phototube with S-4 spectral response) were placed along the trajectory of the particle with a three-inch separation between tubes. The signals from the phototubes were fed through cathode-follower amplifiers to an impedance-matching network where the outputs were added together. The combined signals were then displayed on an oscilloscope. The duration of the signal from each tube was short compared to the transit time between photomultipliers

so that a typical signal consisted of a series of ten, or fewer, discrete pulses. The amplitude of each pulse was proportional to the radiant energy incident on the photocathode of the tube. In the cases where fewer than ten pulses appeared, correlation was accomplished using time-of-flight techniques utilizing the time base generated by the primary detector. The gains of the phototubes were adjusted periodically to a common, although arbitrary, value by means of a modulated tungsten filament light source.

A photograph of the complete experimental system is shown in Fig. 2. The base of the Van de Graaff can be seen through the opening in the wall at the right. The differential pumping section is near the center of the picture. The photomultipliers and cathode followers can be seen in place along the target section which is about one meter in length.

III. MEASUREMENT OF THE DRAG COEFFICIENTS

The velocity of a solid spherical particle traveling through a rarefied gas should obey the fundamental drag equation, derivable from Eq. (1):

$$\frac{dv}{dt} = - \frac{[\rho \pi r^2]}{m} v^2 \quad (6)$$

where ρ is the gas density, r and m are the particle radius and mass, v is the particle velocity and $[\]$ is the drag coefficient. This equation may be integrated to give:

$$\frac{1}{v} = \left[\frac{[\rho \pi r^2]}{m} \right] t + \frac{1}{v_0} \quad (7)$$

The quantity in brackets is constant for a given particle. Therefore, a graph of reciprocal velocity versus time should be a straight line with a slope directly proportional to the drag coefficient. Experimentally we measured distance versus time and computed the average velocity between points.

The position measurement was accomplished with the fifteen-station detector described above. The detector signal was amplified by a calibrated preamplifier and presented on an oscilloscope with calibrated vertical amplifiers and sweep speeds. A tracing of a typical oscilloscope picture is shown in Fig. 3. The upper trace is from the primary detector located just ahead of the differential pumping system and the bottom trace is from the fifteen-station detector inside the gas.

Each oscilloscope trace was measured with a traveling microscope and a plot of reciprocal velocity versus time was made for each particle. A typical plot is illustrated in Fig. 4. The best straight line fit for each set of points was found by a least-squares analysis. A value of Γ was then computed using the particle parameters derived from the primary detector. The gas pressure was measured with a calibrated thermocouple gauge, corrected for the thermal conductivities of the different gases.

The results of these measurements are presented in Table I. The radius and initial velocity of each particle are included. All the data were taken at gas pressures such that the molecular mean free path was large compared to the particle diameter and the conditions for hypersonic free molecular flow were fulfilled.

Although there is some spread in the data, we are led to the conclusion that the drag coefficient is very close to unity for iron particles and the three different gases used.

IV. MEASUREMENT OF THE HEAT TRANSFER COEFFICIENT

In order to describe the energy transfer from the gas to the particle, we have followed the treatment normally used to describe meteoroid entry into the atmosphere. The mass of gas striking the particle per unit time is $(\rho \pi r^2 v)$, where ρ is the gas density, πr^2 is the particle projected area and v is the particle velocity. The energy brought in by the gas is $1/2 (\text{mass}) \times (\text{velocity})^2$ and a fraction λ of this energy is converted into particle internal energy. Thus, we have:

$$\frac{dE}{dt} = \frac{\lambda}{2} \rho \pi r^2 v^3 \quad (8)$$

where E is the internal energy of the particle. We are defining the heat transfer coefficient λ by the equation above.

If we could follow the temperature of a particle proceeding through the gas, the behavior would be somewhat as follows: Along the first part of the path, all the energy is going into raising the temperature while radiation and vaporization losses are negligible. When the temperature reaches 1535°C , the melting point, there is an interval of constant temperature during which the particle melts. The thermal time constant for a spherical particle is of the order of $t \approx Cr^2\rho/k$, where C is the specific heat, k is the heat conductivity, ρ is the particle density and r is the radius. For a one-micron diameter iron particle, this time is about 2×10^{-8} seconds. Since the times involved in our experiments are of the order of tens of microseconds, we expect the particle to be at a substantially uniform temperature.

Once the particle has melted, the temperature will start to rise again, since energy is still pouring in. At some later time the energy lost by thermal radiation becomes important and the

temperature does not increase as rapidly. However, the vast majority of our particles are fast enough so that they are temperature limited, not by radiation, but by vaporization. The temperature climbs to something over 3000°K , where the energy lost by vaporization and radiation balances the input energy.

The particle continues to slow down and the energy being delivered decreases. The temperature, limited by vaporization, also decreases. Finally, a point is reached where there is little energy lost by vaporization, and the temperature is controlled by the thermal radiation. The time constant for a particle losing energy by radiation alone is relatively long and so the temperature falls more slowly. At this point our experiments usually end.

It is obvious that if we could measure the temperature and mass ablation as a function of velocity, we could compute the heat transfer coefficient. However, the measurement of mass ablation at low velocities and with small particles is very difficult. Without knowing how much energy is going into vaporization, it would be of little use to know how much goes into radiation.

On the other hand, there is a section of the particle track where we may be relatively certain that little energy is going into either vaporization or radiation. This is the time interval just after the particle has entered the gas. All the energy is being used to raise the particle temperature towards the melting point. We need only to identify the melting point at 1535°C and we may calculate directly the heat transferred to the particle.

We believe that the behavior of the charge on the particle gives an indication of when the particle turns molten.

All particles, without exception, lose some fraction of their charge shortly after entering a gas target. This applies to all the gases we have used. In general, the charge follows a curve very similar to those illustrated in Figs. 5 and 6. There seems to be a

short time when the charge loss is small and then an almost linear decrease occurs. Invariably, the loss then stops and the particle continues on with a constant charge. If the curve is followed further, the charge once again starts to decrease as illustrated in Fig. 6 and, in a time comparable to the first decrease, goes to zero.

The explanation we advance for this behavior is as follows. When the particles first enter the gas, the average electric field at the surface is 2×10^9 volts/meter. Small irregularities on the surface enhance this field at local spots. The combination of high fields and bombardment by gas atoms with an energy equivalent to a few electron volts causes the emission of ions. We do not know whether the ions emitted are iron, iron oxides, or ionized target gas. However, a combination of gas and field is necessary since there is no charge loss for a particle traveling through vacuum.

Whatever the actual mechanism of initial charge loss, the critical assumption we make is that the melting of the particle smooths out the local irregularities and lowers the field. At this point the charge emission stops. We take the knee of this curve to be the time of melting and measure it as indicated in Figs. 5 and 6. A graph of charge versus time was made for each particle analyzed and the time the particle melted was determined in this manner.

Since we are dealing with highly charged solid spheres which become molten, it is of interest to calculate the Rayleigh limit⁴ of our particles; namely, that value of the charge q on a liquid droplet of radius r at which the coulomb repulsion just balances the force due to surface tension σ , i.e., $q^2 = 64\pi^2\sigma\epsilon_0 r^3$. When the charge is below this limit, a liquid drop is stable against breakup. Figure 7, illustrating some of the data for particles in air, shows that while nearly all of our particles start with an amount of charge in excess of the Rayleigh limit they fall below the limit before they reach

the point where we assume they are molten. The crosses in Fig. 7 represent the initial particle charge and the circles represent the charge on the same particle after it has ceased losing charge.

There is still one uncertainty, and that is whether the latent heat of melting should be included. If the particle melts from the surface, uniformly inward, probably little of the latent heat should be included and only the energy necessary to raise the temperature by 1500°K would be counted. Since the heat is delivered on the front side only, perhaps an acceptable compromise would include only one-half of the latent heat of melting. The analysis of the data does not include the latent heat, but it is a simple matter to correct the results so as to take this into account.

To find λ we equate the energy necessary to raise the particle temperature by 1500°K to the energy delivered over a time τ ,

$$mC(1500) = \int_0^{\tau} \frac{\lambda}{2} \rho \pi r^2 v^3 dt . \quad (9)$$

We chose an average specific heat C of $0.165 \text{ cal/gm}^{\circ}\text{C}$ for iron over this temperature range. The particle mass m was measured as described in Section II, and the particle radius was derived from $m = (4/3)\pi r^3 \rho_{\text{Fe}}$ with the density of iron taken as 7.8 gms/cm^3 . The gas density ρ was derived from the pressure measured by a calibrated thermocouple gauge. The reciprocal velocity was plotted versus time for each particle, as illustrated in Fig. 4, and the measured curve used to determine the velocity function used in the integral. The measured heat transfer coefficients are presented in Table II, along with the initial velocities and particle radii. The heat transfer coefficient for nitrogen was calculated from those of oxygen and air, by the following equation:

$$\lambda_{\text{air}} = 0.79 \lambda_{\text{N}_2} + 0.21 \lambda_{\text{O}_2} \quad (10)$$

Since the latent heat of melting is not included, these values would represent a lower limit. Inclusion of the latent heat would mean raising all the values of λ by a factor of $(1 + L/1500C)$ where L is the latent heat of melting and C is the specific heat. If we take $L = .64$ cal/gm and $C = 0.165$ cal/gm^{°C}, this factor is 1.26. Should only one-half of the latent heat be used, then the correction factor is 1.13.

There is one other correction which should be applied to the heat transfer coefficient derived for oxygen. This would take into account the possible addition of chemical energy from the exothermic reaction of iron and oxygen. The fact that the oxygen data consistently yield coefficients greater than unity indicates something of this nature is taking place. At natural meteor velocities the relative contribution of this chemical energy will be much smaller, since the kinetic energy contribution increases as the square of the velocity.

Accounting for this energy is difficult, but, if we assume that the heat transfer coefficient for oxygen is the same as the average of argon and air, then the difference between measured and assumed values would be due to chemical reactions. With this assumption, we can calculate the average chemical energy delivered per molecule of oxygen. When this has been done we find that the average energy is 0.35 eV/molecule. Since iron-oxygen reactions have typical energies of two or three eV, this result implies that about one out of ten molecules which strike the particle reacts chemically.

At the present time we have no direct evidence to support the assumption that the particle reaches the melting point coincident with the cessation of charge loss. However, the results are consistent with this assumption and there are several points which argue in favor of this conclusion.

In the first place, the heat transfer coefficients are close enough to unity that melting cannot occur much earlier than we designate. This would require energy transfer with an efficiency greater than 100%. Melting must then occur either at the time we indicate or sometime later. If it is later, then an argument must be developed to explain the cessation of charge loss without a change of phase. Examination of the data indicates that the melting argument is consistent with the observations while other explanations are not. For example, the effect is not directly related to the electric field since the field varies by at least a factor of two between particles. It is not a function of the time spent by the particle in the gaseous environment because this varies by an order of magnitude. Charge loss does not cease at a given particle velocity. The results, however, are consistent with a temperature rise, i.e., they obey Eq. (9) reasonably well as shown in Table II.

Further support for the melting hypothesis is obtained from the results of a separate set of experiments. In these experiments, photomultiplier tubes were interspersed with the charge detectors along the gas target tube. Thus, we observed the charge loss and light emission simultaneously. The visible light emitted by the particle was observed to rise sharply to a maximum along the trajectory and then decay. The maximum occurs later than the knee on the charge curve.

In Fig. 8 we have taken one particle and plotted the measured velocity and light output versus time. By assuming a heat transfer coefficient of unity and knowing the particle mass and velocity, we may compute the temperature rise of the particle. The results of this calculation are included in Fig. 8 also. The actual temperature will rise less sharply above 2000°K than indicated because we have neglected any energy losses by radiation in the computed curve.

The calculated thermal time constant of a particle losing energy by radiation alone is much longer than the observed decrease in the light output. From this we infer that vaporization is limiting the particle temperature near the peak of the light output curve. If this is the case, the temperature must be in the neighborhood of 3000°K or higher. We may then look back along the particle trail and estimate when the temperature was 1800°K . When this is done, the results agree with our original assumption that the particle is near 1800°K when the charge loss stops.

V. SUMMARY

The drag coefficients of small spherical particles traveling through oxygen, argon and air under conditions of hypersonic free molecular flow have been measured. The results presented in Table I are consistent with a value of unity for the drag coefficient in all three gases. The measurement technique was straightforward and the deviations in the results can probably be ascribed to experimental errors on individual particles.

We have derived a value for the heat transfer coefficients in the same three gases and under the same conditions. In order to calculate these coefficients we found it necessary to make certain assumptions concerning the temperature and physical state of the particles. These assumptions are outlined in Section IV. None of these arguments is conclusive proof, but they are all consistent. We conclude, therefore, that the values of heat transfer coefficients which we have tabulated in Table II are valid lower limits for this velocity and particle regime.

Table I. Drag Coefficients

Oxygen Data ¹			Argon Data ²			Air Data ³		
v_o (km/sec)	r (microns)	Γ	v_o (km/sec)	r (microns)	Γ	v_o (km/sec)	r (microns)	Γ
5.8	0.32	1.02	6.8	0.23	0.94	6.7	0.31	1.13
5.3	0.43	1.27	5.1	0.51	0.94	6.4	0.29	1.24
5.2	0.37	1.09	4.9	0.63	0.93	5.7	0.41	1.11
4.8	0.54	1.24	4.7	0.55	0.91	5.1	0.52	1.03
4.7	0.65	1.14	4.2	0.55	0.88	4.8	0.56	1.03
4.7	0.62	1.12	4.1	0.68	0.96	4.7	0.57	0.88
4.6	0.64	1.14	3.7	0.56	0.92	4.7	0.57	1.01
4.6	0.42	0.68	3.6	0.73	0.84	4.3	0.43	1.02
4.5	0.61	1.20	3.5	0.93	1.01	4.0	0.55	1.16
4.4	0.61	0.81	3.4	0.97	1.02	4.0	0.55	1.10
4.4	0.54	0.84	3.2	1.08	1.02			
4.4	0.42	0.86	2.8	1.11	1.12			
4.4	0.59	1.06						
4.3	0.68	1.06						
3.7	0.71	0.95						
3.4	1.02	1.23						
3.1	1.06	1.20						

Mean Values with
r.m.s. deviations:

$$\Gamma_{\text{oxygen}} = 1.05 \pm 0.17 \quad \Gamma_{\text{argon}} = 0.96 \pm 0.08 \quad \Gamma_{\text{air}} = 1.07 \pm 0.09$$

1. gas pressure = 2.0 and 1.0 mm Hg
2. gas pressure = 1.3 mm Hg
3. gas pressure = 1.5 mm Hg

Table II. Heat Transfer Coefficients

Oxygen Data ¹			Argon Data ²			Air Data ³		
v_o (km/sec)	r (microns)	λ	v_o (km/sec)	r (microns)	λ	v_o (km/sec)	r (microns)	λ
4.2	0.66	1.07	5.0	0.51	0.98	6.7	0.31	0.89
4.1	0.65	1.05	4.9	0.63	0.79	6.5	0.30	0.76
4.0	0.81	1.00	4.7	0.55	0.94	6.2	0.40	0.84
3.7	0.67	1.09	4.6	0.58	0.99	6.0	0.46	0.80
3.6	0.87	1.07	4.2	0.71	0.84	5.2	0.63	0.81
3.6	0.96	1.08	4.2	0.55	0.97	4.8	0.57	0.81
3.4	1.00	0.99	4.0	0.84	0.96	4.7	0.57	0.94
3.4	0.64	1.06	3.8	0.56	0.86	4.6	0.66	0.97
3.3	0.60	1.05	3.7	0.85	0.96	4.4	0.63	0.83
3.2	0.66	1.09	3.6	0.70	0.75	4.4	0.43	0.78
						4.0	0.55	0.99
						3.9	0.71	0.88
						3.8	0.70	0.91

Mean Values with
r.m.s. deviations:

$$\lambda_{\text{oxygen}} = 1.06 \pm 0.03 \quad \lambda_{\text{argon}} = 0.90 \pm 0.08 \quad \lambda_{\text{air}} = 0.86 \pm 0.07$$

For nitrogen (obtained by combining air and oxygen data)

$$\lambda_{\text{nitrogen}} = 0.81 \pm 0.09$$

-
1. gas pressure 2.0 mm Hg
 2. gas pressure 1.3 mm Hg
 3. gas pressure 1.5 mm Hg

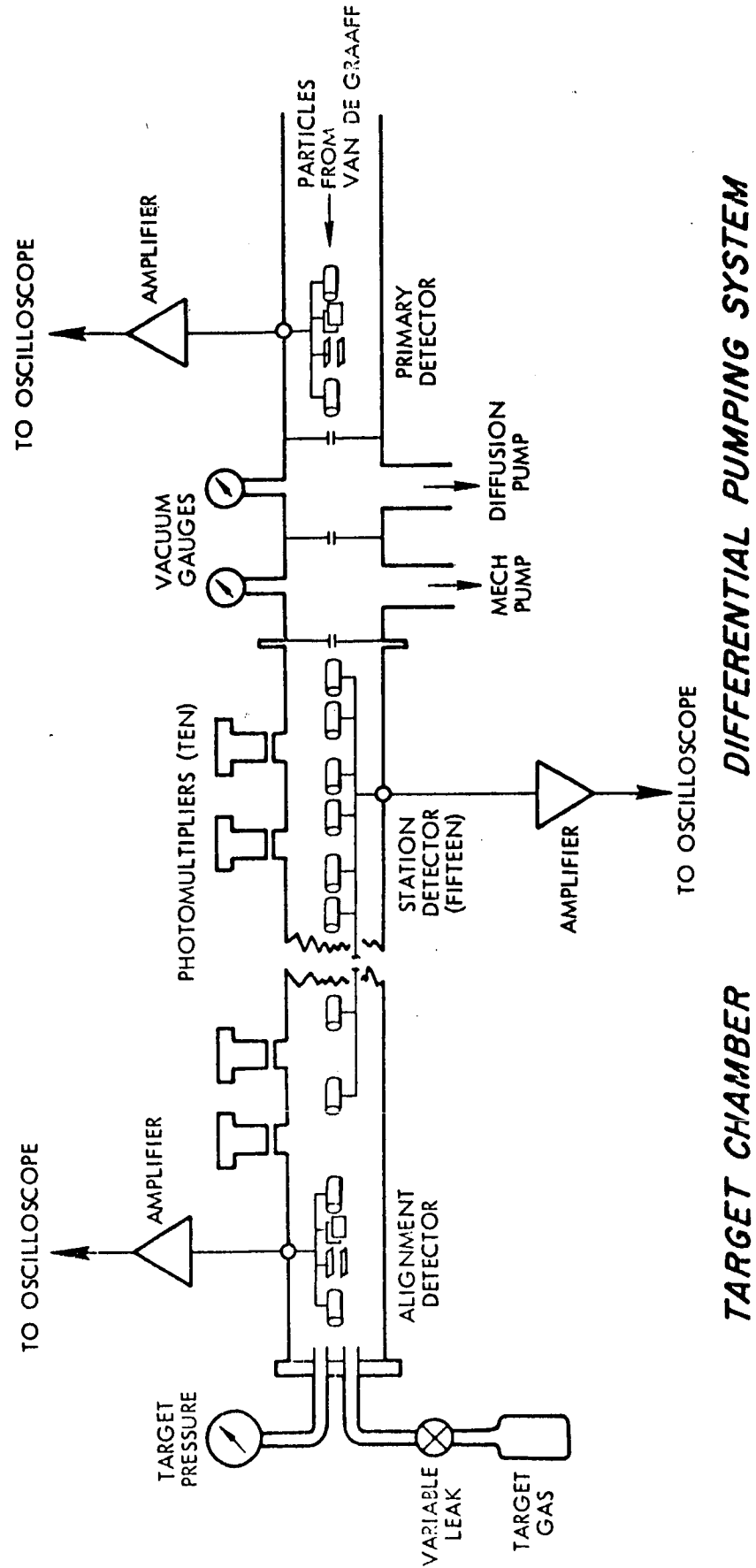


Figure 1. Schematic diagram of experiment.

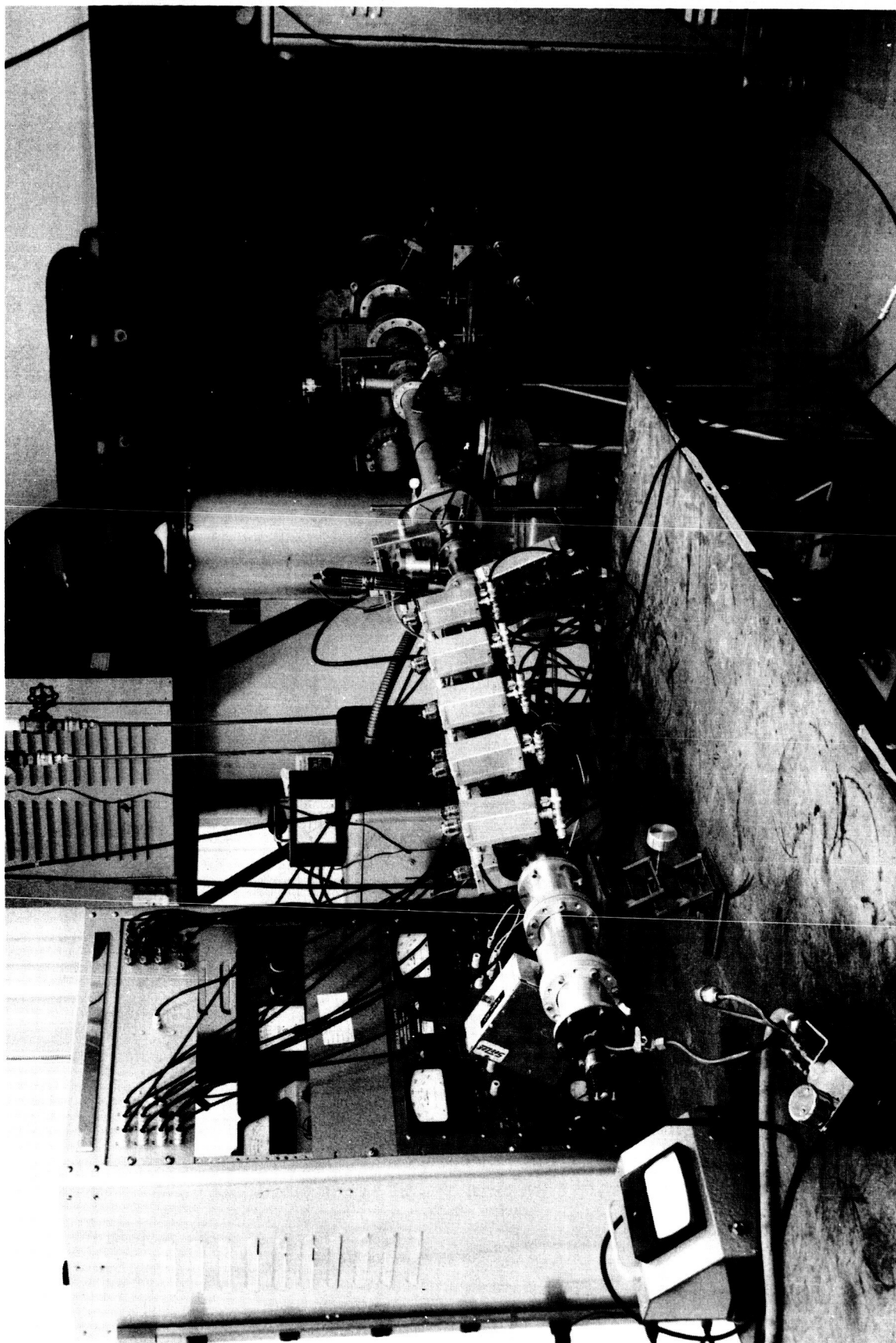


Figure 2. Photograph of experimental apparatus.

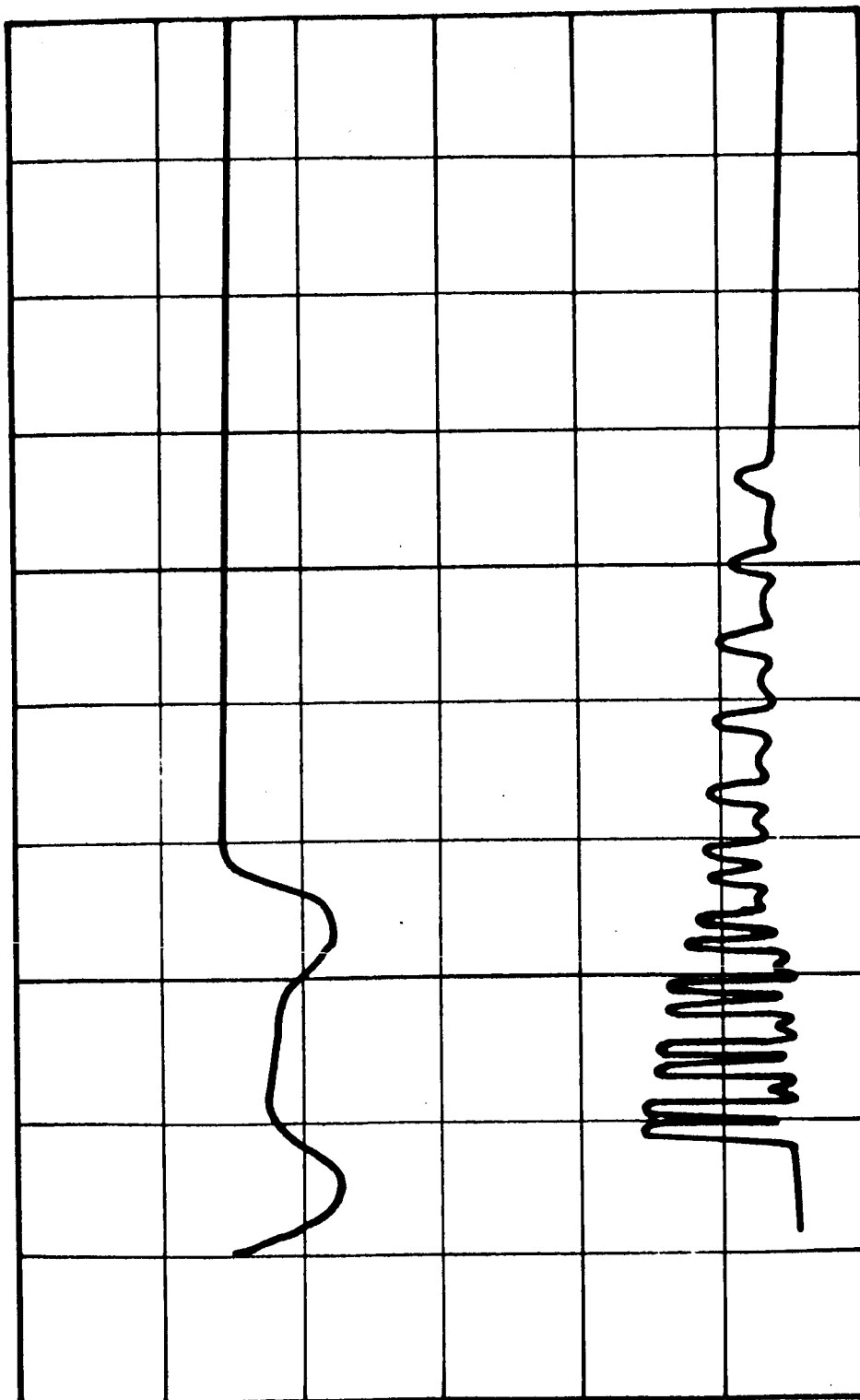


Figure 3. Typical oscilloscope trace. The upper trace shows the output of the primary detector. The vertical scale is 0.1 volts/div and the sweep speed is 5.0 μ sec/div. The lower trace shows the output of the fifteen-station detector. The vertical scale is 0.1 volts/div and the sweep speed is 50 μ sec/div.

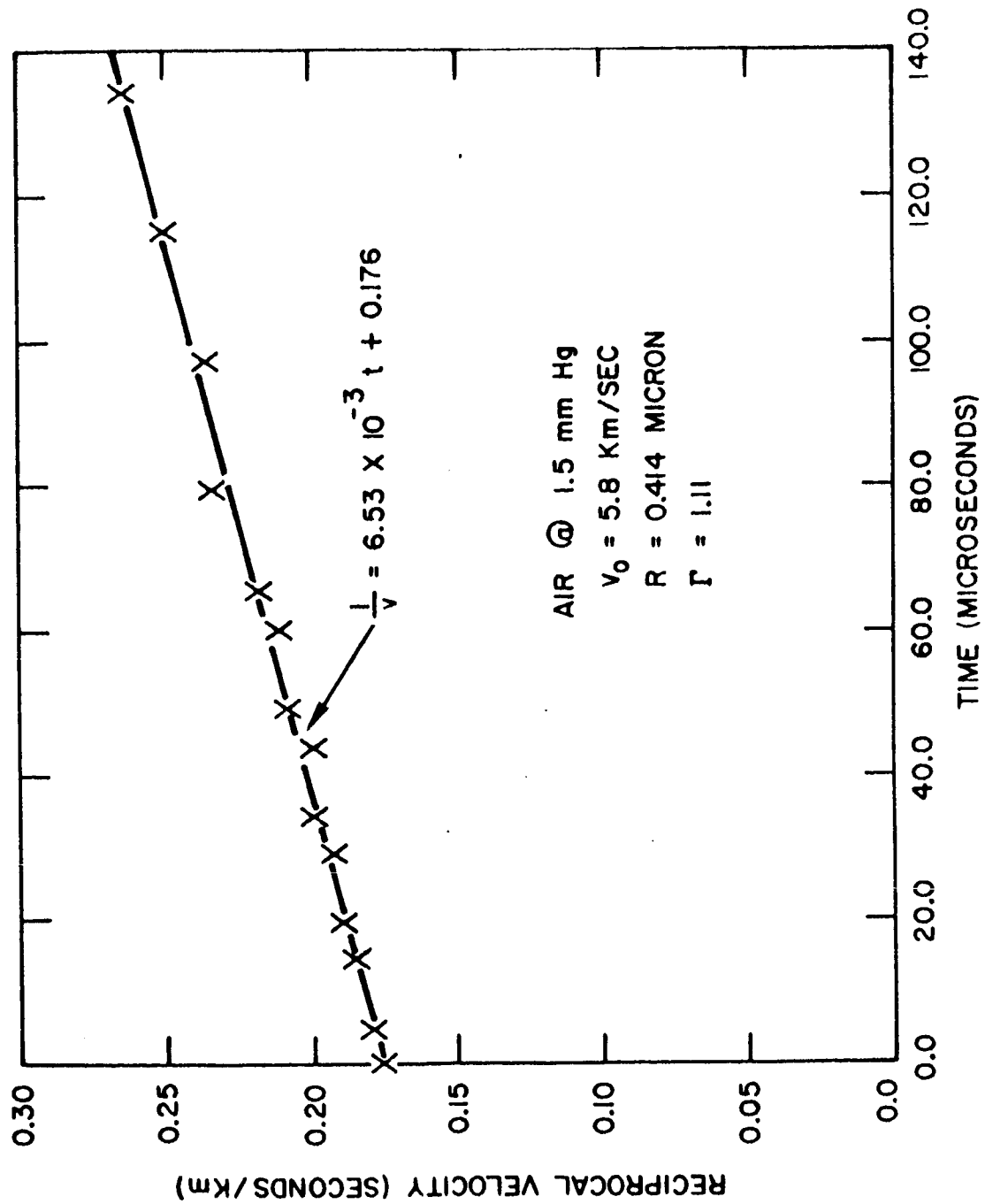


Figure 4. Least-squares fit of reciprocal velocity versus time for a typical particle.

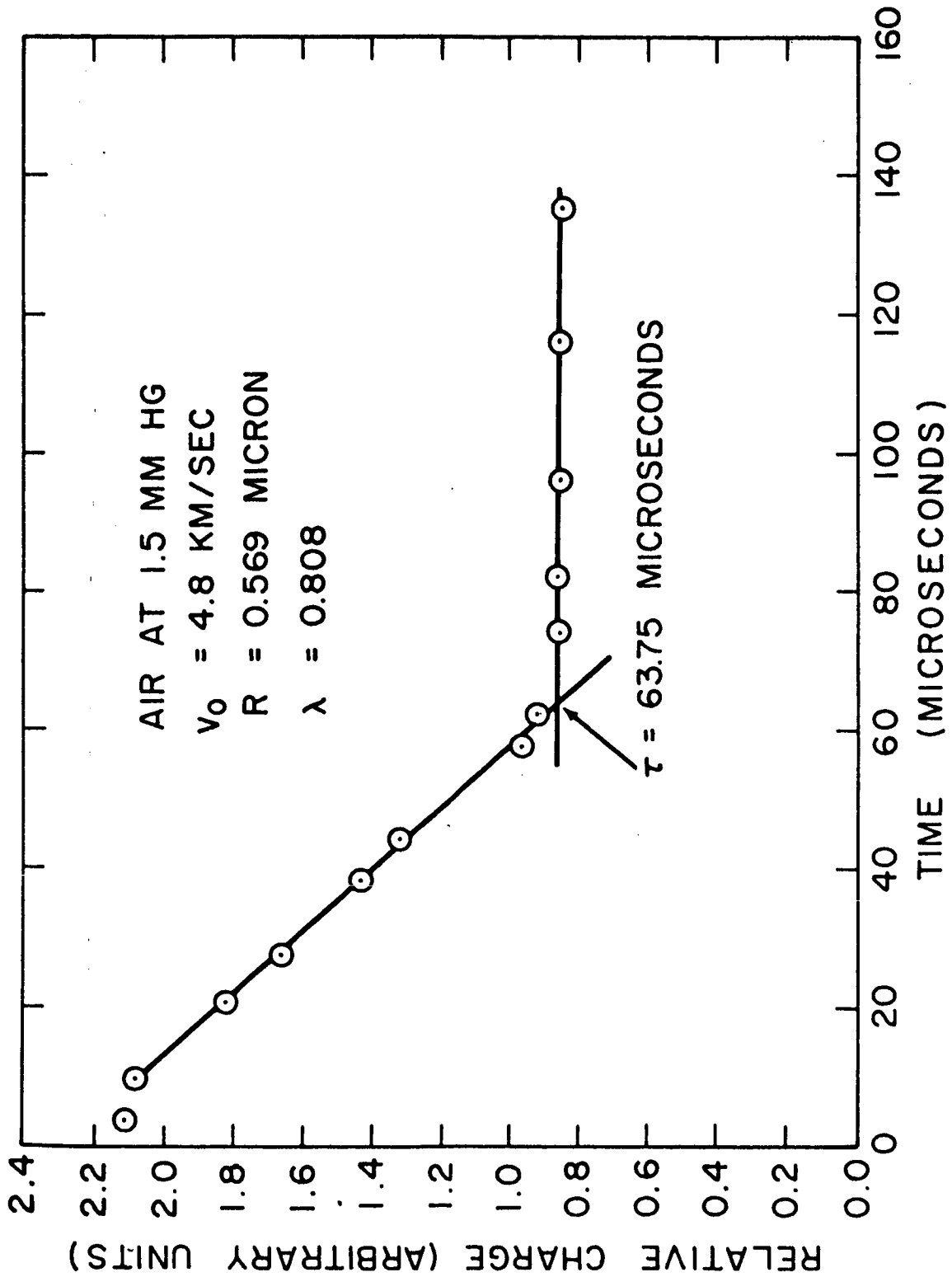


Figure 5. Graph of charge versus time for a typical particle illustrating the method used to find the time of melting.

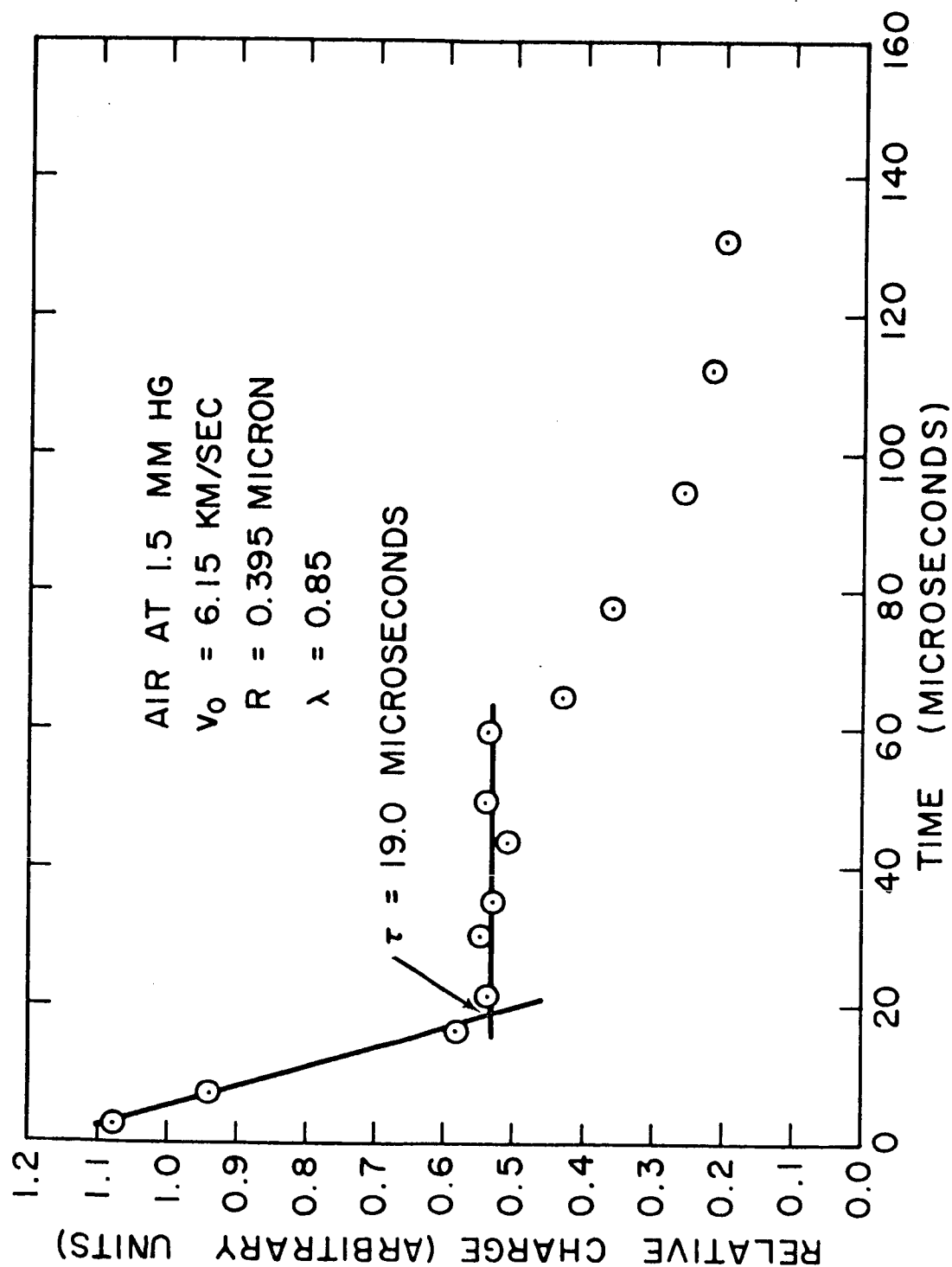


Figure 6. Graph of charge versus time for a particle which displays loss of charge during latter part of trajectory.

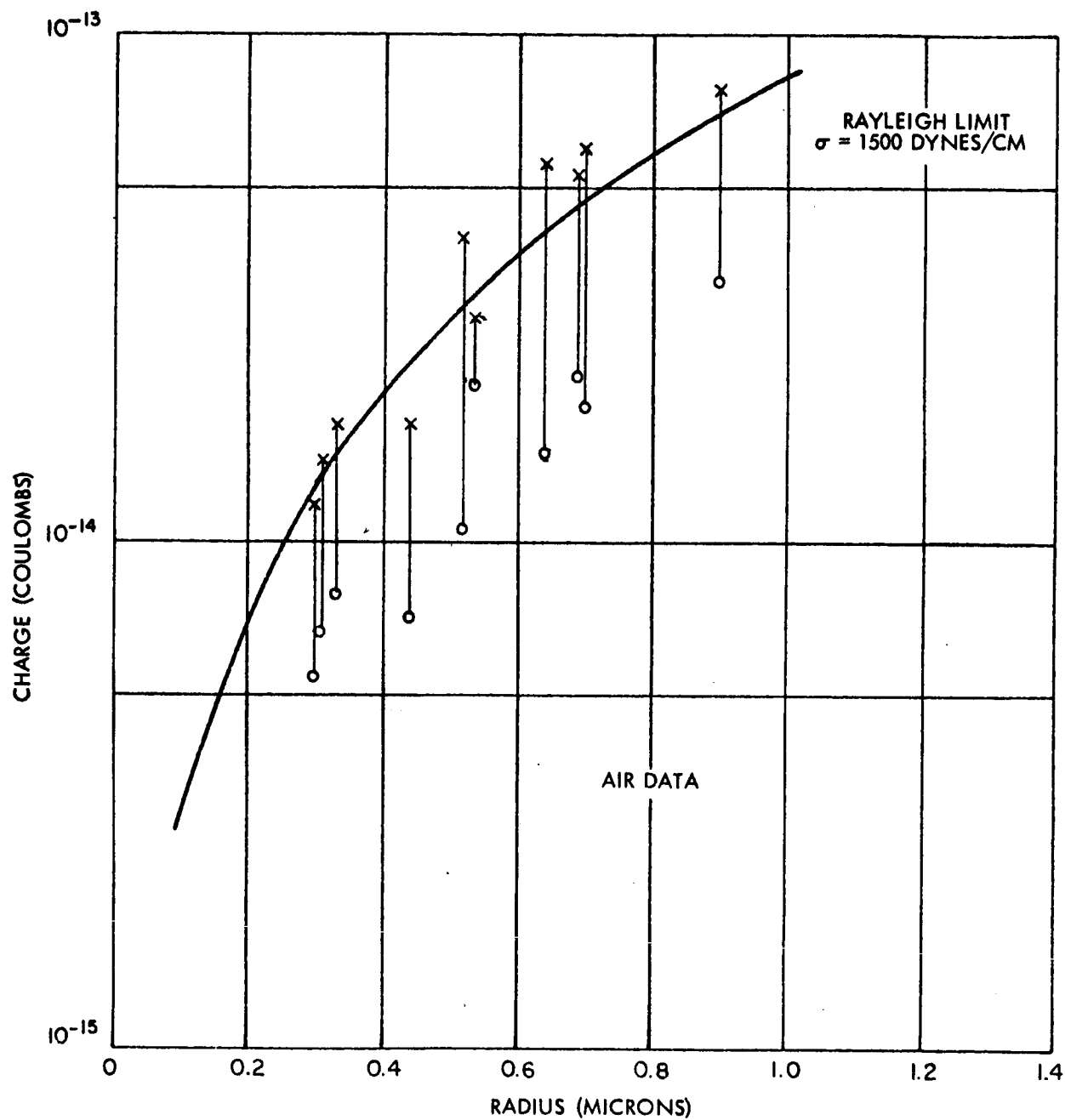


Figure 7. The solid curve is the Rayleigh limit (see text) for liquid particles with a surface tension of $\sigma = 1200$ dynes/cm. Each cross and open circle represents one experimental particle. The cross represents the initial charge and the open circle represents the charge after the particle has melted.

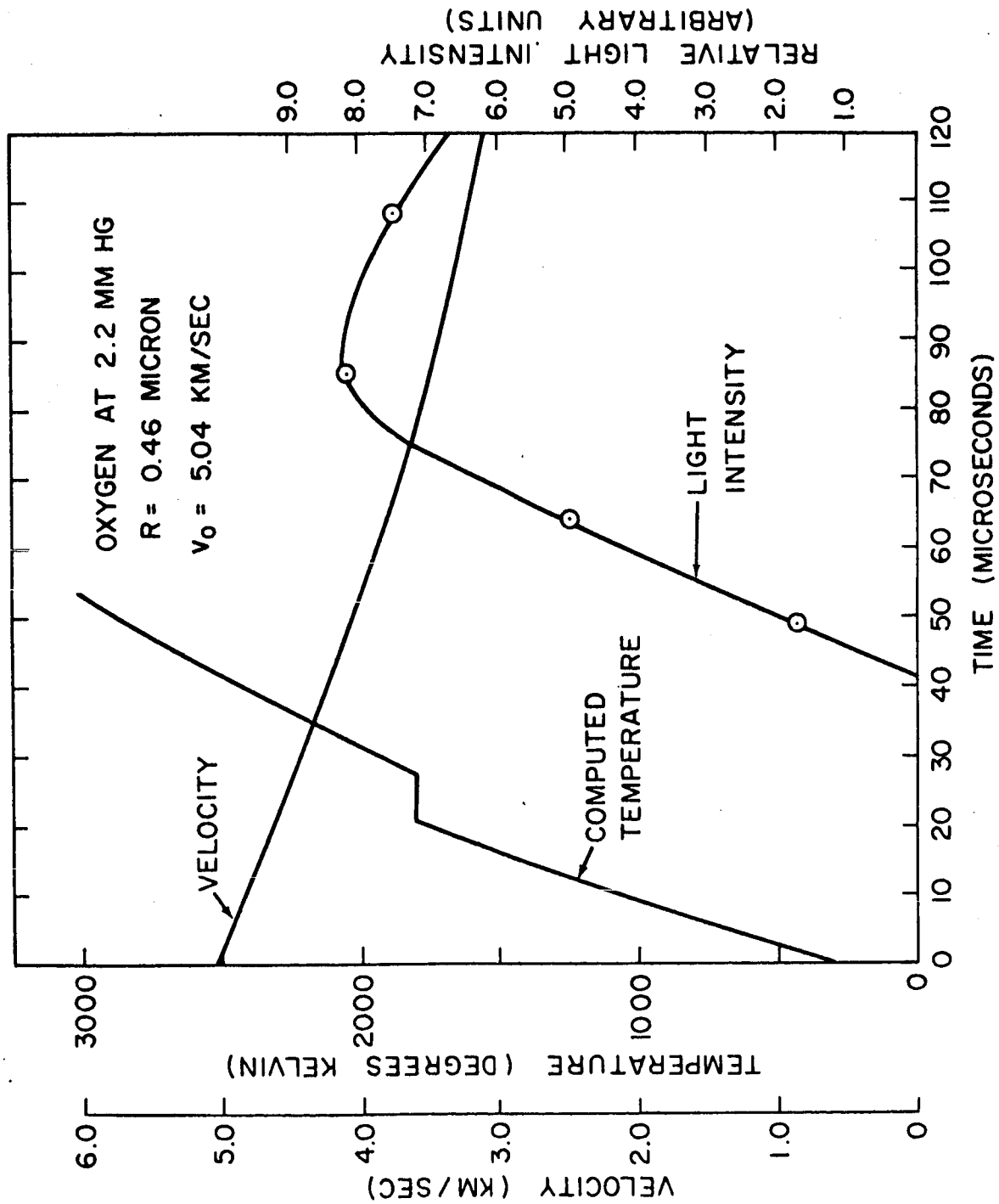



Figure 8. Graph illustrating measured velocity and measured light output for a typical particle. Included is a plot of particle temperature computed assuming a heat transfer coefficient of unity. See text for a more complete discussion.

REFERENCES

1. F. L. Whipple and G. S. Hawkins, "Meteors", Handbuch der Physik, Vol. LII, Springer-Verlag, Berlin, 1959.
 2. J. F. Friichtenicht, Rev. of Sci. Inst., Vol. 33, 209 (1962).
 3. H. Shelton, C. D. Hendricks, Jr., and R. F. Wuerker, J. Appl. Phys., Vol. 31, 1243, (1960).
 4. Lord Rayleigh, Phil. Mag. 5, 14, 184 (1882); "The Theory of Sound", (Dover Publications, Inc., New York, 1945), Vol. II, p. 372.
- 

**PENETRATION OF THIN FILMS BY HYPERVELOCITY
MICROPARTICLES**

APPENDIX N

TECHNICAL REPORT

"PENETRATION OF THIN FILMS BY HYPERVELOCITY
MICROPARTICLES"

July 1965

Prepared for

National Aeronautics and Space Administration
Washington, D. C. 20546

Contract No. NASw-936


Prepared by
J. F. Friichtenicht
Manager, Meteoritics Dept.


Approved by
D. B. Langmuir
Director

PHYSICAL ELECTRONICS LABORATORY
Physical Research Division
TRW Systems
One Space Park, Redondo Beach, California

PENETRATION OF THIN FILMS BY HYPERVELOCITY MICROPARTICLES

I. INTRODUCTION

At least one type of micrometeoroid detector operates on the basis of light transmission through holes produced in otherwise opaque films by the impact of micrometeorites. The detector flown aboard the Explorer VII satellite by LaGow and Secretan¹ was of this type. In their device, the opaque film was placed between a light source and a photomultiplier tube, which measures the quantity of light transmitted through the film. A sudden increase in phototube current signals a meteoroid impact. The magnitude of the phototube current increase is proportional to the area of the hole in the film. For maximum benefit to be derived from the measurements, it is desirable to relate the current increase to the parameters of the impacting micrometeoroid.

Films typical of those used by LaGow and Secretan were calibrated using high-speed particles from the TRW Systems electrostatic hypervelocity accelerator.² A brief experimental program in support of these measurements was conducted and the results are given below. It should be pointed out that the results are equally applicable to the general area of hypervelocity impact phenomena.

II. PROCEDURES AND RESULTS

The thin film, in the form of a strip about one inch wide by three inches long, was mounted in a test fixture attached to the end of the accelerator drift tube. The plane of the film was perpendicular to the axis of the particle beam. A detector³ for the measurement of particle charge, velocity, mass, and trajectory was positioned immediately in front of the film holder. The film could be moved manually in a direction defined by the long axis of the film, thus exposing a number of separate and distinct target areas to the beam.

As many as ten areas could be utilized before the target was removed from the vacuum chamber. The film holder was carefully indexed and the observed impact sites were correlated with the trajectory information derived from the particle detector.

The targets were 0.00025 inch thick mylar films with a thin (about 0.1 micron) layer of vapor-deposited aluminum on the impact side. The diameter of the holes produced D_H was measured with a screw micrometer eyepiece and a high power optical microscope. For these measurements, D_H is defined as the diameter of that part of the crater transparent to light. In general, this diameter is smaller than the overall diameter of the disturbed area. Carbonyl iron spheres were used for all of the shots. The particle diameter D_p was determined by the techniques described in Ref. 3.

The results are summarized in Fig. 1. The results show that the ratio of hole diameter to particle diameter increases slowly with velocity, but is relatively constant from about 5 or 6 km/sec and up. The scatter of the data points prohibits a reasonable estimate of the velocity dependence. The lack of precision arises from errors in the measurement of both of the quantities. Also, it is likely that the thickness of the film relative to the size of the particle plays an important role, but this has not been considered. It is clear, however, that the hole diameter is at most one or two times the particle diameter even at the highest impact velocities. More precise measurements are required to fully assess the situation.

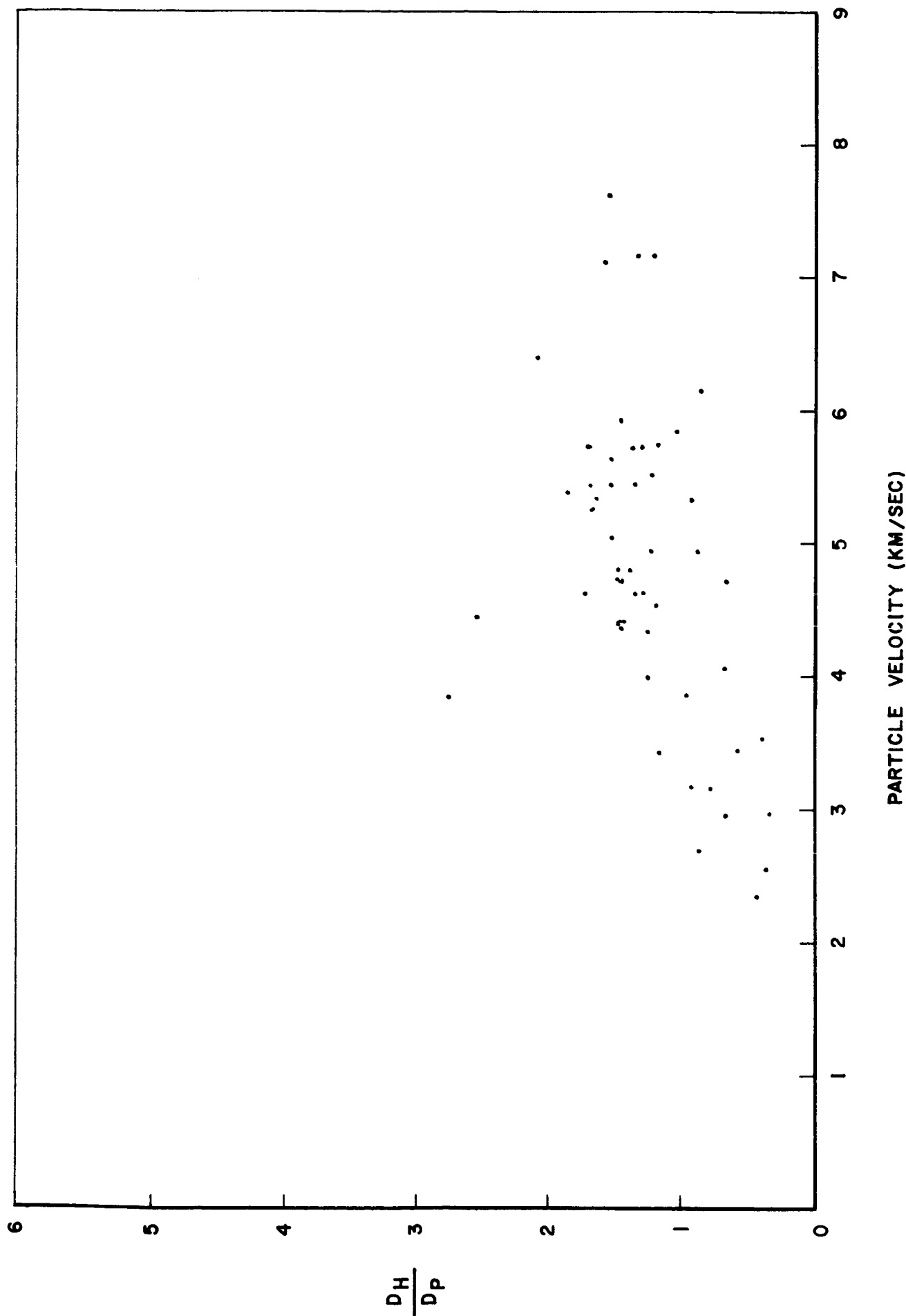


Figure 1. Relative hole diameter of holes produced in thin films by the impact of high speed particles as a function of velocity.

REFERENCES

1. H. E. LaGow and L. Secretan, "Results of Micrometeorite Penetration Experiment on the Explorer VII Satellite (1959 Iota)", NASA Technical Note D-1722, April 1963.
2. J. F. Friichtenicht, "Two-Million-Volt Electrostatic Accelerator for Hypervelocity Research", Rev. of Sci. Instr., Vol. 33, 209-212, 1962.
3. H. Shelton, C. D. Hendricks, Jr., and R. F. Wuerker, "Electrostatic Acceleration of Microparticles to Hypervelocities", J. of Appl. Phys., Vol. 31, 1243-1246, 1960.

SOLID-STATE DETECTOR

APPENDIX O

TECHNICAL REPORT

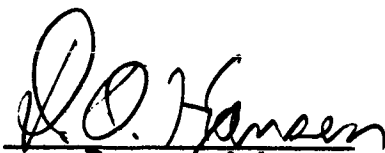
"SOLID-STATE DETECTOR"

August 1965

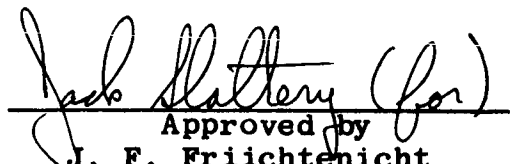
Prepared for

National Aeronautics and Space Administration
Washington, D. C. 20546

Contract No. NASw-936



Prepared by
D. O. Hansen



Approved by
J. F. Friichtenicht
Manager, Meteoritics Dept.

PHYSICAL ELECTRONICS LABORATORY
Physical Research Division

TRW Systems
One Space Park, Redondo Beach, California

SOLID-STATE DETECTOR

The TRW electrostatic microparticle accelerator is nearly an ideal facility for the development and testing of sensitive micrometeorite detectors. The results of experiments on the impact ionization effect¹ and tests of thin film capacitor penetration detectors indicate behavior similar to the properties exhibited by semiconductor particle detectors. These semiconductor detectors enjoy general use in the field of nuclear physics. The charge collection mechanisms are reasonably well understood for nuclear particles and the manufacturing processes have reached a high degree of sophistication. Furthermore, standardized instrumentation has been developed for use with the basic detector unit. For these reasons, the possibility of using a semiconductor junction detector as a micrometeorite detector were examined.

For these initial tests an n-type silicon surface barrier diode (fabricated at TRW) was used. The surface barrier detector is constructed by evaporating a thin layer of gold (100-2000 Å) onto high resistivity n-type material. A distributed p-type layer is formed by surface states at the interface between the metal and the semiconductor. A dipole layer is formed by positively-charged ionized donors in the n-type material and the p-type states. The region which is essentially stripped of conduction electrons is called a surface barrier. A depletion region is formed by the application of a reverse bias across the n-p junction, most of the extent of which is into the n-type region. The width of this depletion region is given approximately by

$$d = (\rho V)^{\frac{1}{2}}/3 \quad (1)$$

where d is the depletion width in microns, ρ is resistivity of the n-type material in ohm centimeters and V is the effective reverse bias in volts. This bias is made up of a self-bias,

which for the detector used was about 1/2 volt, plus the external applied voltage. When the semiconductor detector is used on nuclear particles, for every 3.5 ev of energy lost by the particle in the depletion region, an ion-electron pair is formed, and is then collected by the detector electrodes. It should not be expected that the mechanism of the detector for micrometeorites will be at all similar to that just described for nuclear particles because of the tremendous difference (10^6) in mass of the particles.

In the initial tests the particles from the accelerator were incident on the gold electrode (p side) of the detector which was grounded. An Ortec preamplifier and amplifier (Models 101 and 201) were used with the detector, and these were calibrated to indicate total collected charge from the detector. Bias voltage of 0, 10 and 30 volts were used, and the detector output was not found to depend on the applied bias voltage. This was consistent, since the 0.5 volt self-bias results in a depletion depth of about 40 microns, and this is greater than the expected depth of penetration of the particles. Figure 1 is a plot of signal amplitude, normalized to particle mass, as a function of velocity. The data has a slope of about 3, which is the value obtained in earlier work on impact ionization.

It was discovered that there was a significant fraction (10-20%) of the output signals from the detector which were inverted from the expected polarity. It is not understood at this time why these occurred. It was found that if the n electrode was grounded, the fraction of opposite polarity signals was decreased to about 3%. Also, the slope of the data when plotted as before, seems to be about 5, as compared with three in the other configuration.

It was felt that possibly recombination processes might have affected the observed response. To investigate this, a biased grid was placed in front of the grounded p electrode. Signals were observed at the n electrode. Biases of both polarities and various voltages were used on the grid. The conclusion reached

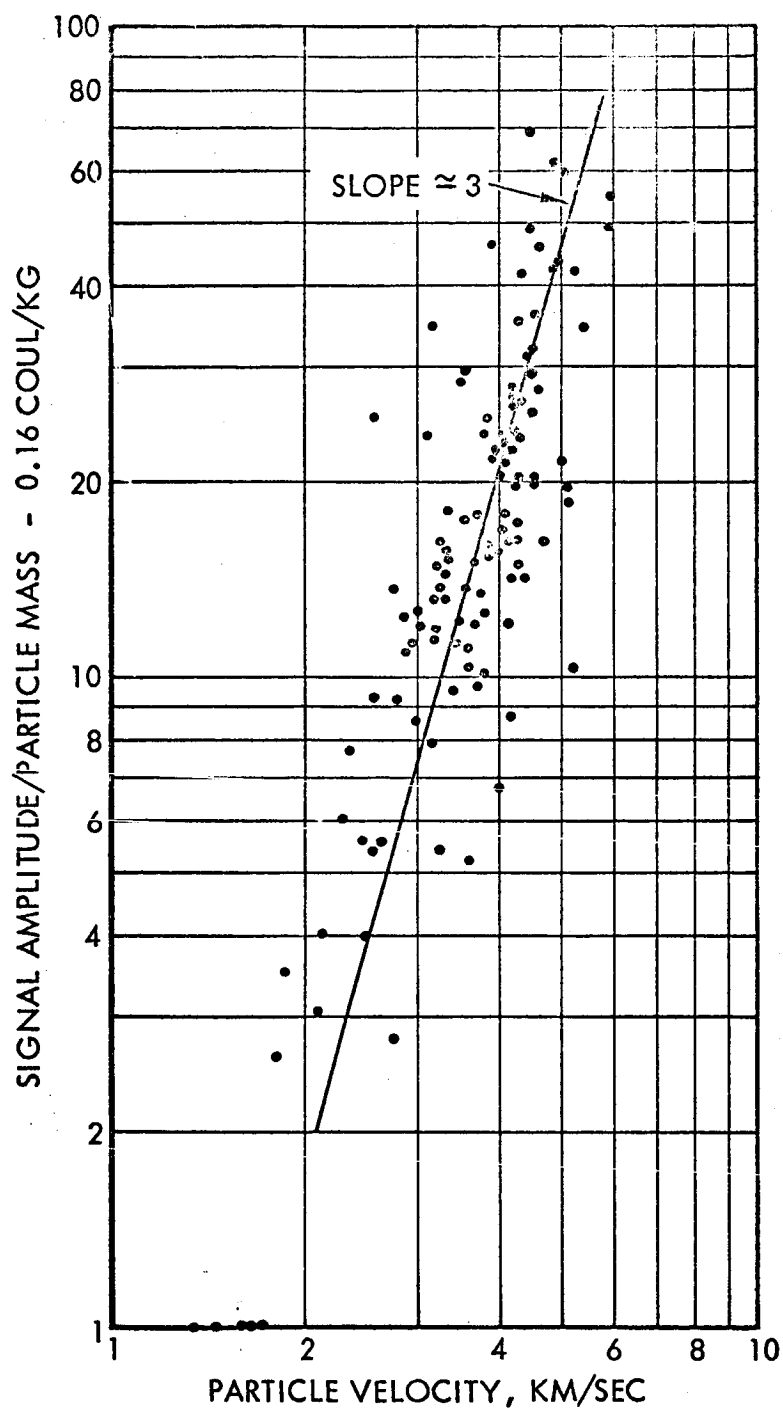


Figure 1. Signal amplitude from semiconductor meteorite detector versus incoming particle velocity.

was that a positive bias on the grid, resulting in electron extraction from the detector, reduced the number of opposite polarity signals by a significant amount.

Based on the results of this preliminary examination, and in view of the advantages that were pointed out at the beginning of this note, it is felt that these detectors certainly merit a more thorough evaluation as a possible micrometeorite detector.

REFERENCES

1. J. F. Friichtenicht and J. C. Slattery, "Ionization Associated with Hypervelocity Impact," NASA TN D-2091.

HIGH VOLTAGE BREAKDOWN INITIATED BY PARTICLE IMPACT

APPENDIX P

TECHNICAL REPORT

HIGH VOLTAGE BREAKDOWN INITIATED BY PARTICLE IMPACT

April 1965

Prepared for
National Aeronautics and Space Administration
Washington, D. C. 20546

Contract No. NASw-936

Prepared by

J. F. Frichtenicht
for J. C. Slattery

J. F. Frichtenicht
J. F. Frichtenicht

D. O. Hansen
D. O. Hansen

Approved by

D. B. Langmuir
D. B. Langmuir
Director

PHYSICAL ELECTRONICS LABORATORY
Physical Research Division
TRW Space Technology Laboratories
Thompson Ramo Wooldridge Inc
One Space Park, Redondo Beach, California

HIGH VOLTAGE BREAKDOWN INITIATED BY PARTICLE IMPACT*

J. C. Slattery, J. F. Friichtenicht and D. O. Hansen
TRW Space Technology Laboratories, Redondo Beach, California

This letter describes the techniques employed and reports results of exploratory experiments on the particle initiated high voltage breakdown hypothesis due to Cranberg¹. The assumption is made that small particles are torn from an electrode by electrical stress and are accelerated across the gap. Upon impact at the opposite electrode, gas and metal vapor are evolved from the surface, creating local conditions conducive to the initiation of a discharge between the electrodes. No attempt is made to explain the mechanism of particle formation nor to justify the existence of such particles on fundamental grounds. However, an analysis by Slivkov² applies constraints on particle size. The upper limit is established by requiring that the kinetic energy of the particle be sufficient to vaporize its own mass. The lower limit is established by requiring that the gas cloud be large enough to permit charge multiplication while simultaneously satisfying the conditions at the Paschen minimum.

Maitland³ has compiled data from a number of experimenters and finds that the results are compatible with the particle initiated breakdown concept. Rozanova⁴ has shown conclusively that particle impacts are capable of initiating discharge by placing loosely bound particles on the surface of conditioned electrodes. Application of pulsed voltages resulted in breakdown attributed to the particle impacts. Results of work in our laboratory on the effects of micrometeoroid bombardment of ion engines⁵ suggested a similar mechanism. This led to the experiments described below.

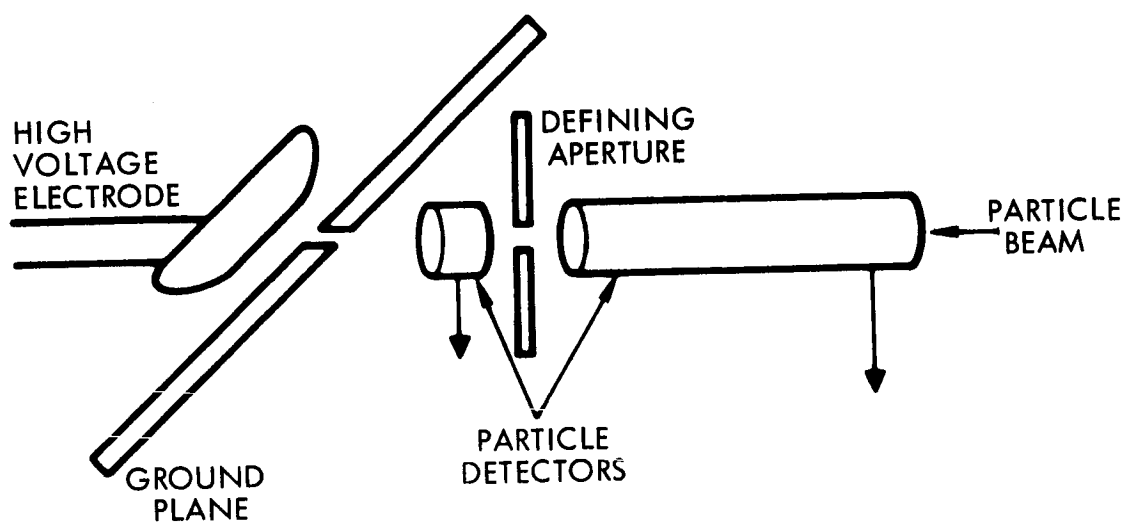
* This work supported by the NASA under Contract No. NASw-936.

In these experiments, particles of known mass and energy are injected through an aperture in one electrode of a plane parallel electrode configuration. The particle parameters are completely independent of electrode spacing and voltages and the experiments are primarily concerned with the investigation of the effects of voltages and electric fields on the developing discharge. The experiments provide no information on the mechanism of particle formation required for the Cranberg hypothesis. However, the parameters of particles required to initiate discharge can be determined and compared to what might be anticipated in an actual case.

The STL electrostatic hypervelocity accelerator⁶ was used as a source of particles. In this device, small iron particles are charged by a process described elsewhere⁷ and are injected into the accelerating field of a 2-million volt Van de Graaff generator. The particle mass and energy are determined prior to impact by techniques described in Ref. 7.

A diagram of the experimental configuration is shown in Fig. 1. Particles from the accelerator pass through a detector used for the measurement of particle mass and velocity. Most of them pass through a 0.75 mm diameter defining aperture which is aligned with a 1 mm aperture in the ground electrode. Finally, the particles impact upon the high voltage electrode. Another particle detector is interposed between the two apertures and serves to identify which of the particles passing through the main detector eventually strike the target. In practice, slight misalignment results in less than 100 per cent transmission through both apertures. For each set of conditions, the transmission was determined and the observed frequency of discharge was weighted accordingly.

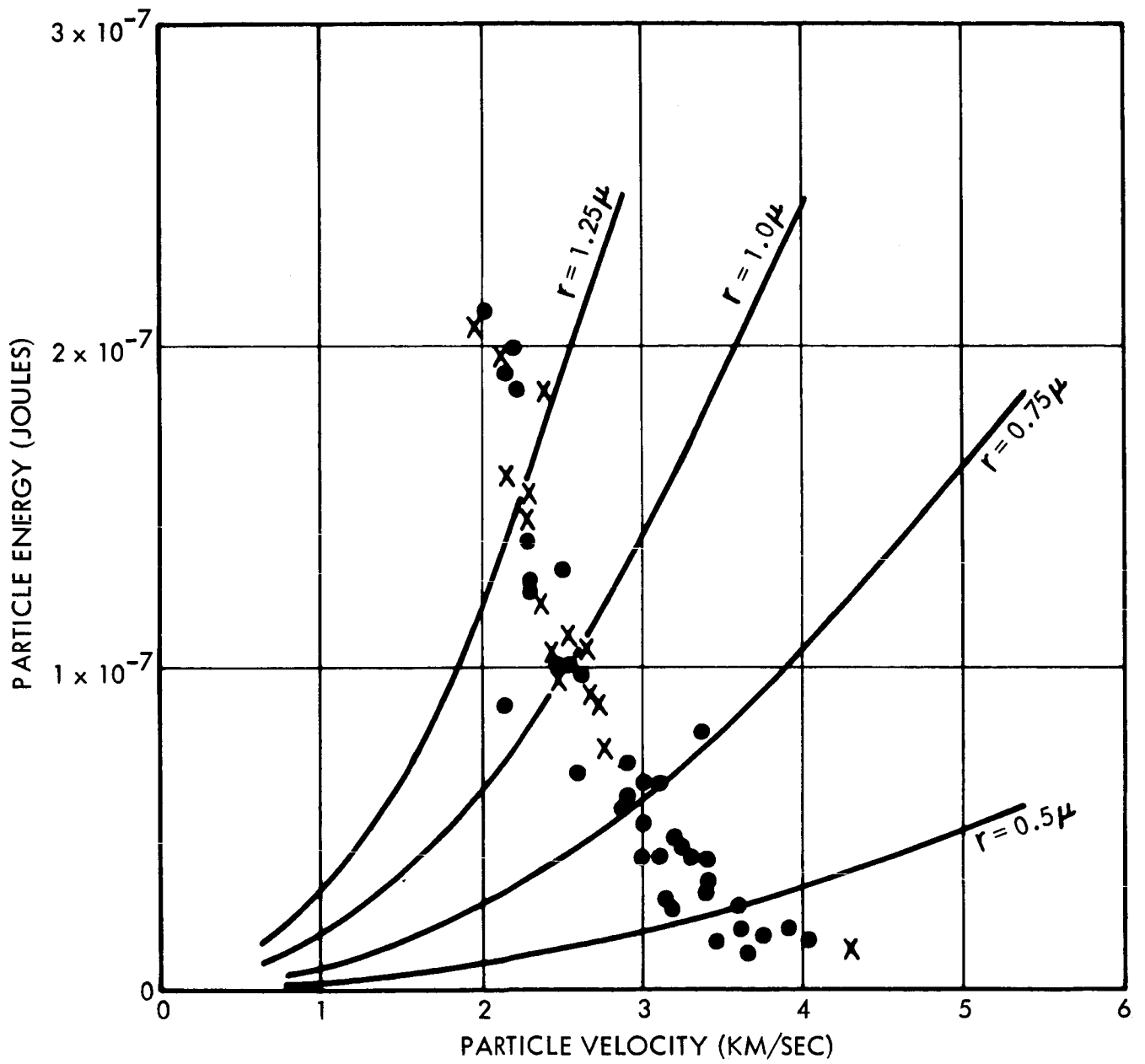
Both of the electrodes were made of polished stainless steel. The ground plane was in the form of truncated cylinder about 3.8 cm in diameter. The high voltage electrode was machined to a Rogowski⁸



surface having a flat center portion of about 1 cm diameter and an overall diameter of 2.5 cm. The gap between electrodes was adjustable over a relatively wide range as was the voltage applied to the electrode. However, no voltages exceeding positive or negative 30 kilovolts were used.

The electric field lines at the impact point are somewhat distorted by the presence of the aperture in the ground plane. To reduce this, the electrodes were inclined by 45° to the particle beam. The effects of distortion have not been evaluated completely, but it is assumed that the discharge occurs between the impact point and a smooth portion of the ground plane. Discharges were sensed by observing the voltage developed across a 0.1 ohm resistor interposed between the ground plane and true electrical ground.

Results obtained under typical conditions are shown in Fig. 2. The x's denote the parameters of particles which initiated discharge while the points represent particles that did not. For the case illustrated, a 15 kv positive voltage was applied to the electrode and the gap was 0.5 mm. The probability of discharge is evidently much greater for particles with energies and radii in excess of about 0.8×10^{-7} joules and 0.9 microns, respectively. The relatively sharp threshold between discharge and no discharge is exhibited for all voltages and fields used. This defines a lower limit in particle energy (or size) below which discharge is not initiated. No upper limits were observed. Thus Slivkov's prediction of particle size limits is only partially verified by these experiments. However, the requirement imposed by Slivkov that the particle possesses enough kinetic energy to vaporize its own mass is an oversimplification of the case. Partial vaporization of a large particle would release more gas than complete vaporization of a small one. The fraction of particle material vaporized is a strong function of velocity, but Slivkov does not consider this aspect. A revision of Slivkov's criteria to include



velocity effects may be in order.

The thresholds in particle energy and size required to initiate breakdown shift with voltage and electric field. Smaller, less energetic particles are capable of initiating discharges for higher voltages and fields. Insufficient data are available to define the voltage and field dependence but it appears that the electric field is a more critical factor. This again is in general agreement with Slivkov. He implies that charge multiplication with the expanding gas cloud is dependent upon the potential difference across the cloud. For a cloud with dimensions smaller than the gap spacing, the total voltage across the cloud is determined by the voltage gradient.

The parameters of particles charged and accelerated under conditions suggested by Cranberg and Slivkov can be computed and compared to the parameters of particles used here. Assuming spherical iron particles, a charging mechanism similar to that described in Ref. 7, and conditions identical to those used in obtaining the results given in Fig. 2, a 30 micron radius particle would be required to attain the threshold energy shown in Fig. 2. This is obviously too large to be compatible with the Cranberg-Slivkov formulation. However, the particle impact hypothesis is not directly applicable at the voltages and fields used here. It is interesting to note that the estimate in particle size is compatible with the experimental observations of Rozanova.

A definite dependence on the polarity of the applied voltage was observed. Significantly less energetic particles are required to initiate discharge when the particle impacts on the cathode. For example, virtually all of the particles shown in Fig. 2 would have initiated discharge if the polarity had been reversed.

In summary, the experiments described above provide quantitative information on the particle initiated voltage breakdown hypothesis. The existence of a low energy limit for particles capable of initiating discharge has been verified and measured.

A definite polarity dependence was noted and the effects of applied voltage and electric field were observed qualitatively. Although the validity of the Cranberg hypothesis cannot be verified directly by these experiments, extension of the measurements to higher voltages and fields would enable one to define the parameters of particles required to initiate breakdown under conditions where the particle impact hypothesis is presumed to be valid. Evaluation of particle formation mechanisms in light of these results could be instrumental in testing the validity of the Cranberg breakdown hypothesis.

REFERENCES

1. L. Cranberg, J. Appl. Phys., 23, 518 (1952).
2. I. N. Slivkov, Soviet Phys., Tech. Phys. 2, 1928 (1957).
3. A Maitland, J. Appl. Phys., 32, 2399 (1961).
4. N. B. Rozanova, Izv. AN SSSR, Ser. Fiz., Trans. Bulletin 26, 1462 (1962).
5. J. C. Slattery, Final Report, NASA Contract No. NAS3-3569, NASA CR-54057, June, 1964.
6. J. F. Friichtenicht, Rev. of Sci. Instr. 33, 209 (1962).
7. H. Shelton, C. D. Hendricks, Jr., and R. F. Wuerker, J. Appl. Phys., 31, 1243 (1960).
8. J. D. Cobine , "Gaseous Conductors", McGraw-Hill, p. 177, (1941).